Wind Energy extraction using flutter mechanism of rigid sections

by

Sidharthan Kasi Murugan

A thesis submitted to the graduate faculty

in partial fulfillment of the requirements for the degree of

MASTER OF SCIENCE

Major: Aerospace Engineering

Program of Study Committee:
Partha P. Sarkar, Major Professor
Vinay Dayal
Thomas Ward

The student author, whose presentation of the scholarship herein was approved by the program of study committee, is solely responsible for the content of this thesis. The Graduate College will ensure this thesis is globally accessible and will not permit alterations after a degree is conferred.

Iowa State University

Ames, Iowa

2022

DEDICATION

I would like to dedicate this thesis to my family. My adoring parents, Murugan and Rajalakshmi, my sister Bavani, deserve special gratitude for their unconditional love, support and encouragement throughout my life which helped me to be the person I am today. I am always grateful for the all the sacrifices they have done for my success.

TABLE OF CONTENTS

Page

LIST OF FIGURES

Page

LIST OF TABLES

Page

ACKNOWLEDGMENTS

I would like to thank my committee chair, Dr. Partha P. Sarkar, and my committee members, Dr. Vinay Dayal and Dr. Thomas Ward for their guidance and support throughout the course of this research.

In addition, I would also like to thank my friends, colleagues, the department faculty and staff for making my time at Iowa State University a wonderful experience. I also want to offer my gratitude and appreciation to Mr. Andrew Jordan and Mr. Neil Osborn for their help in my experiments, without them this thesis would not have been possible.

ABSTRACT

Fluid-structure interaction (FSI) is routinely used for resolving design related vibration issues of flexible structures, for example, long-span bridges, tall buildings, airplanes (wings or tails), wind turbine and helicopter blades. In the past few years, numerous studies have used FSI as a tool to study fluid-based energy harvesting from solar, wind, and ocean. Due to high capital investment and maintenance cost, the conventional land-based wind turbines are not suitable for small-scale wind energy harvesting at low wind speeds, and due to acoustic and aesthetic issues these turbines cannot be deployed in proximity of city centers or on building roof tops or backyards, where energy is in high demand. Therefore, an alternate mechanism that exploits the various aeroelastic phenomena including vortex-induced vibration, buffeting, galloping, flutter, etc., to cause large-amplitude response in specific structural shapes has been explored by some for tapping the renewable wind energy source in the low-wind speed regime. This study explores the feasibility of a flutter-driven or flutter-induced vibration (FIV) wind energy harvester that uses rigid-body motions of section models to harvest wind energy at low wind speeds. Section models are rigid-models with 1-3 degree-of-freedom (DOF) that faithfully represent the geometry of the cross-section of a structure over a finite length, with end plates to simulate a 2D-flow. The objective of this study was to explore the parameters that will influence the performance of the FIV wind energy harvester which is assessed by the low magnitude of flutter speed and large magnitude of vibration amplitude at or near flutter.

There are various cross-sections of section models that are prone to vibration at a given wind speed along a particular DOF. Rectangular sections of aspect ratio (AR) less than 2 usually have low flutter speeds in the vertical DOF and ‘H’-shaped sections, used in old long-span bridges like Tacoma Narrows, have low flutter speeds in the torsional DOF. A hybrid section

model formed by combining these two sections is therefore expected to be more sensitive to a coupled vertical-torsional flutter at low wind speeds. Such hybrid cross-sections are ideal for a 2-DOF (vertical and torsional) FIV wind energy harvester. Wind tunnel experiments were performed with geometrically scaled models to determine the flutter speed and average wind energy capture for various section models in 1-DOF and 2-DOF motions. For a comparative study, rectangular section models (AR=1.5 and AR=1) in 1-DOF (vertical or torsional) and 2-DOF (vertical and torsional), and H-shaped section models in torsional DOF were tested. The best rectangular section in the vertical DOF and best H-shaped section in the torsional DOF with respect to low flutter speed and high vertical or torsional amplitudes of vibration are combined to form a hybrid section and tested in 2-DOF (vertical and torsional) and compared with the best rectangular section and best H-shaped section for flutter speed and average wind energy available at flutter. In order to amplify the performance of the devised FIV wind energy harvester, a parametric study of the flutter mechanism is conducted in terms of mass ratio, frequency ratio (2-DOF), location of the pivot point and choice of DOF(s) to use. This study also developed a method to extract the rational function coefficients, used in time-domain flutter analysis numerically, from flutter derivatives of the specific sections used here that will enable a parametric study of the FIV wind energy harvester in the future to optimize its design and wind energy performance of its scaled-up versions for commercial usage. An estimate of the maximum power that can be captured using a linear generator from a scaled-up version of a FIV wind energy harvester that uses a rectangular section of AR=1.5 (0.60 m width x 0.40 m depth and 26.7 kg mass) suspended inside a duct in vertical DOF was made as 100 watts at 2.5 m/s (with a 8:1 inlet area contraction), which is promising.

CHAPTER 1. INTRODUCTION

1.1 Objective

The overall objective of this study is to explore a flutter-driven wind energy harvester that will extract wind energy at low wind speeds through rigid-body motions. This study will explore the effects of the parameters of the wind energy harvester such as cross-sectional shape, mass, frequency, degrees of freedom (vertical, torsional or vertical-torsional), location of pivot point in torsion and the non-dimensional scaling parameters (Amplitude ratio, Scruton number, Reynolds number, Reduced velocity, mass ratio, frequency ratio, etc.) on the performance of wind energy capturing.

1.2 Background and Motivation

In the past few years, there has been various studies on extracting electrical power from the available energy resources such as solar, thermal, wind, ocean, hydropower, biofuels, out of which wind is a bountiful source of clean energy. Wind is abundant in nature; it is available everywhere on earth and in some places with considerable wind energy density (potential wind energy per unit area). Wind energy is not uniformly distributed, but mainly found in the higher layers of the troposphere. The data provided by the NOAA/ESRL Physical Science Division (CO, USA) states that the most favorable altitude in terms of wind power is at approximately 10,000 m (32,800 ft), where average wind speeds can exceed 45 m/s, but it is quite difficult to tap. With much reduced average wind speed near the ground, wind energy density decreases drastically compared to this favorable altitude as it is proportional to the cube power of the average wind speed. At 80 m above the ground, which represents the hub height of the latest generation of wind turbines, the global average wind speed is estimated to be 4.6 m/s, which is barely enough for economical wind power generation. At 10 m above the ground the global

average wind speed is even lower, estimated to be 3.3 m/s. The global average wind power density at an elevation of 10 m from the ground is estimated to be 22 W/m^2 and at 80 m above the ground, it is 58 W/m^2. The traditional wind energy harvesters or wind turbines adopt rotation of turbine blades in wind as a mechanism to generate power. The scale of these wind turbines is quite large, and their energy conversion efficiency drops as the size of the harvester decreases which is due to high drag ratio and electromagnetic interference. Therefore, the high cost and complexity of a conventional wind turbine designs restrict wind energy harvesting at small scale ($\leq$ 10 m rotor diameter), lower elevations ($\leq$ 10 m) and low wind speeds ($\leq$ 10 m/s). Another issue of a land wind turbine is that power transmission from the wind farms, where multiple wind turbines are located, to large population centers over long distances is costly and less efficient because of loss of power due to transmission. Wind turbines cannot be deployed close to population centers and within urban centers because of acoustic issues. Thus, an alternate method of capturing wind energy that addresses these issues needs to be explored.

When a flexible structure is subjected to an airflow, it vibrates due to the fluid-structure interaction. These structural vibrations can be potentially converted into electrical energy. Wind resource as widespread kinetic energy has been widely exploited in the past decades. In the past few years, fluid-structure interactions have been studied not only for design issues related to failure, but also for energy harvesting purposes, exploiting the aeroelastic instabilities (e.g.: flutter, galloping, vortex-induced vibrations, buffeting). Energy harvesting deals with the energy conversion from external driving sources like solar power, thermal energy, vibrational energy, etc. The basic concept of energy harvesting is to obtain electrical energy by energy conversion from wasted heat, vibration, potential energy, mechanical deformation, etc. The converted energy derived from these ambient sources is either directly consumed or stored in a

rechargeable battery for future use. Theses energy harvesting mechanism are a great resource for the Aerospace industry because, every year enormous amount of money is lost in terms of maintenance cost, fuel consumption, emissions from different systems, etc. These energy harvesters can convert mechanical vibrations, acoustic waves and dissipated heat into electrical energy and the potential for energy saving is enormous. There are various mechanisms for extracting energy from the mechanical vibrations, such as electromagnetic (Arnold [1]), electrostatic (Mitcheson et al. [2]) and piezoelectric (Abdelkefi et al. [3]). A flutter-induced vibration (FIV) energy harvester is one such micro-environmental device that can be used to scavenge the available wind energy due to the mechanical vibration induced by the flow. Flutter is a typical aeroelastic instability phenomenon where divergent and large-amplitude vibrations occur beyond a critical wind speed or flutter speed. Thus, flutter phenomenon has a wide wind speed range above the flutter speed, where larger-amplitude response, proportional to the wind speed, is sustained which is beneficial for wind energy harvesting. It is important to note that FIV wind energy harvesters can be designed to adapt to low flutter speed, fluctuating wind speed and changing wind direction. Thus, the flutter phenomenon is more beneficial than other flow-induced vibrations such as vortex-induced vibration (VIV) for wind energy harvesting. It is known that there are specific cross-sectional shapes that are prone to vibration at a given wind speed and a specific wind angle of attack (angle between major axis of the cross-section and wind direction). Wind energy harvesting, using vibration of a flat plate with porous screens to induce aeroelastic instability, has been proposed [4]. A comprehensive research review of this work may be found in Young et al. [5]. Caracoglia [6] investigated a torsional-flutter-based apparatus using an airfoil section for extracting wind energy, where the location of the pivot point on flutter speed was studied. Cao and Sarkar [7] performed vertical-torsional experiments

using section models of certain cross-sectional shapes and figured out that the bluff cross-sections have a lower flutter speed compared to the streamlined cross-sections in both DOFs (vertical and torsional). Matsumoto [8] extracted flutter derivatives of bluff (rectangular shapes) cross-sections of low aspect ratios (= width/depth or B/D ratios) out of which the section with an aspect ratio of 1 was found to have the lowest flutter speed in the vertical DOF. Hou and Sarkar [9] extracted the flutter derivatives for the bluff sections with aspect ratios of 1.5 and 0.67 and found that the flutter speed is lower for the B/D=1.5 case. From the extracted flutter derivatives of a structure that are functions to model aeroelastic or motion-induced loads for flutter analysis, one can determine the reduced velocity at which the structure will start to flutter in a particular vibration mode (vertical, torsional, lateral, and combination thereof). Thus, rectangular sections of low aspect ratios (< 2) have usually low flutter speed in the vertical DOF than the torsional DOF. Further, it was known that historic long span bridge sections that are 'H' shaped have low flutter speed in the torsional DOF, for example, Tacoma Narrows Bridge (1940). Scanlan and Tomko [10] extracted the flutter derivatives of various bridge cross-sections using wind tunnel experiments out of which the 'H' shaped sections were found to have the lowest flutter speed in the torsional DOF. Thus, if these two types of sections (rectangular and H) are combined to form one rigid section then the system would be vulnerable to coupled vertical-torsional flutter at low wind speeds because rectangular section is prone to flutter in the vertical DOF and the 'H' section in the torsional DOF. A parametric study of the flutter mechanism of a single-DOF and two-DOF system with flutter-prone sections at low wind speeds needs to be conducted to study the flutter mechanism with respect to the frequency ratio, mass ratio and the offset distance (between center of mass and center of stiffness) to achieve a better understanding of the design criteria for a FIV wind energy harvester to optimize its performance.

The accuracy of any experimental test result can be always validated using the corresponding numerical simulations. Numerical simulations using the equations of motion will facilitate parametric study of a dynamic system such as the FIV wind energy harvester. Traditional analysis for calculating response of a slender structure or long span bridge section that is subjected to aerodynamic loads in time domain employs rational function coefficients. The aerodynamic behavior (displacement, velocity and acceleration) of any structure at flutter speed or below it can be numerically predicted in time domain with the help of rational function coefficients, both in smooth-wind and turbulent-wind case. Cao and Sarkar [7] and Sauder and Sarkar [11] developed and validated algorithms for direct extraction of rational functions from section model tests using a forced vibration technique. These algorithms require time histories of aeroelastic loads (forces and moments) acting on the model and the displacements of the model during its vibration as inputs. Since measurement of aeroelastic loads can be challenging and cumbersome for certain cross-sections, an algorithm to extract the rational function coefficients directly from the flutter derivatives that are widely available in the literature and easier to extract for any cross section without using the aeroelastic loads will be very useful.

1.3 Current Work

The main objective of this study is to explore the feasibility of a FIV wind energy harvester that will be able to scavenge the available wind energy at low wind speeds using flutter mechanism. Rectangular sections (with aspect ratio less than 2) have low flutter speed in the vertical DOF and H-shaped sections have a low flutter speed in the torsional DOF. Thus, rectangular sections with aspect ratio of 1.5 and 1, and H-shaped sections are selected for this study. Before beginning the wind tunnel experiments, the displacements of each cross-section during 1-DOF and 2-DOF (vertical, torsional and vertical-torsional) flutter was numerically

predicted using rational function coefficients in time domain. Wind tunnel experiments using geometrically scaled models were performed to determine which rectangular section is prone to flutter at a lower wind speed and will produce higher magnitude of vibration in the vertical DOF, and which H-shaped section will flutter at a lower wind speed with higher magnitude of vibration in the torsional direction. Finally, a hybrid section is made, in which one half of the best rectangular section is combined with one half of the best H-shaped section, because it was anticipated that a rigid body section formed by combining these two sections is prone to coupled vertical-torsional flutter at low wind speeds. From the wind tunnel test results, one can determine which cross-section or combination of cross-sections will have the best amplitude of flutter in a particular mode of vibration (vertical, torsional and vertical-torsional), which is vital for wind energy extraction. A parametric study is conducted with respect to the frequency ratio, mass ratio and the offset distance (between centers of mass and stiffness) to achieve a better understanding of the design criteria for a FIV wind energy harvester.

Also, a new algorithm is proposed and investigated for direct extraction of rational function coefficients from the flutter derivatives data. This formulation does not need time histories of displacement and aeroelastic loads to extract the rational functions. Therefore, this formulation is only applicable to those cross-sections of structures that already have the flutter derivatives extracted. It is certainly advantageous for those cross-sectional shape where it is difficult to measure the aeroelastic loads. The rational function coefficients for the proposed sections of the FIV wind energy harvester were extracted that will enable to conduct a parametric study of the FIV wind energy harvester in the future to optimize its design, its wind energy prediction and performance of its scaled-up versions for commercial usage.

1.4 Organization of this study

This thesis presents a small-scale wind energy harvesting system using a rigid section model, that explores the use of a single cross-sectional shape or a hybrid section by combining two different cross-sections together in 1-DOF (vertical or torsional) or 2-DOF (vertical-torsional). It also includes a new formulation for direct extraction of rational function coefficients from the flutter derivatives data of the used cross-sectional shapes which will enable to evaluate the performance of the wind energy harvester using these cross-sections or other cross-sections in the future. A parametric study is also presented to enhance the performance and better designing of the FIV wind energy harvester. Chapter 2 gives an overview of the relevant aeroelasticity phenomena including the flutter phenomenon. It also includes the methods adopted for estimation of power generated from the recorded acceleration time history. A detailed discussion on direct rational function extraction from the flutter derivative data is provided. Chapter 3 discusses the wind tunnel setup, description of the dynamic suspension system used for model tests, design and assembly of selective section models, data acquisition and experimental procedure. Chapter 4 starts with estimation of critical flutter speed in vertical DOF, torsional DOF and vertical-torsional DOF. The effects of frequency ratio, mass ratio and model offset distance on the critical flutter speed for each section model were studied and discussed. The effect of Scruton number on the amplitude of vibration of a section is also discussed. A comparison of performance on the basis of power generation is presented between the rectangular sections, H-shaped sections and the hybrid section. Chapter 5 gives the summary of all the results and the enhancements made to the small-scale wind energy harvester for optimum power generation. It also mentions further recommendations and future research that can be performed with this energy harvesting system.

CHAPTER 2. BACKGROUND

2.1 Aeroelasticity and Flutter Phenomenon

Aeroelasticity involves the study of interaction of the aerodynamic forces with the structural motions. It is the study of the coupling between aerodynamic, inertial and elastic forces experienced by an elastic body when exposed to a fluid flow. Aeroelasticity has become an integral part of engineering design applications due to variety of reasons in pursuit of making lighter and longer-spanned structures such as airplanes and other aerospace vehicles, long-span bridges, tall buildings, and wind turbine blades that are few examples in aerospace, civil and mechanical engineering. Although historically, research on aeroelasticity has focused on these structural applications to ensure their safety, more recently it has focused on wind energy harvesting from flow-induced vibrations. Flow induced vibrations are very common physical phenomena because these are caused by the aerodynamic instability or vortex shedding when the fluid passes around a slender structure. Although they can cause some structural damage, it also has a great potential for harvesting wind energy from the vibrating structure. The flow induced vibrations can be divided into four categories: vortex induced vibrations (VIV), buffeting, galloping and flutter [12].

Vortex induced vibration (VIV) is closely related to bluff bodies and the flow velocity. When a fluid flows around a bluff body, vortices are shed alternately from either side of the bluff body and normal to the flow direction in its wake. The vortex that is shed from the bluff body generates negative pressure field or suction that alternates between the two sides of the bluff body because of the alternating vortices. These are referred as von-Kármán vortices that are shed periodically over a wide range of Reynolds number (Re) varying between 300 and 3×10^5. Due to this phenomenon, the bluff body is subjected to alternating aerodynamic forces resulting in its

oscillation transverse to the flow direction with a finite amplitude if it is flexible. When the vortex shedding frequency (i.e. frequency of the vortex shedding on one side of the bluff body) becomes equal to the natural frequency of the bluff body along its transverse degree of freedom, resonance occurs, and the bluff body undergoes large amplitude sinusoidal motion at a constant amplitude. This large-amplitude motion continues to occur over a range of fluid velocity during which the vortex-shedding frequency and natural frequency of the body remain equal is known as “lock-in” phenomenon. The velocity of the fluid flow upstream of the bluff body at which VIV at “lock-in” occurs can be determined from a non-dimensional number known as the Strouhal number ($St=f_sD/U$) of the bluff body which relates the vortex shedding frequency (f_s) to the free stream velocity (U) of the fluid and a characteristic dimension of the bluff body (D). Although the forced excitation in VIV from the vortices is at a single frequency, there is a significant amount of motion-induced (or aeroelastic) damping loads that are generated which eventually determines the amplitude of vibration. Vortex induced vibration is a major safety concern for slender structures such as long-span bridges, tall buildings, luminaries, stay-cables in cable-stayed bridges and power-line cables as it can cause undesirable vibrations. However, many have proposed to tap VIV for wind-energy harvesting.

Buffeting is a phenomenon of random excitation of structures caused by the effects of natural turbulence in the upstream flow or wakes from other bluff bodies or wind gusts. The mechanism of buffeting in structures is unlike that of VIV, where the magnitude of the fluid force is independent of the structural motions, and the frequencies of excitation are usually wide-band as influenced by the natural turbulence of the flow and the flow-structure interaction but similar to VIV the structural vibration due to buffeting is also affected by the natural frequency and mechanical damping of the structure. The mathematical formulation to represent buffeting

excitation and estimate its effects has been developed based on random vibration theory. Since buffeting does not generate large-amplitude motions generally, past research on wind energy capture from buffeting has been relatively limited.

Galloping is a typical phenomenon of self-excited vibrations in structures caused by the aerodynamic instability. It occurs in structures with special cross-sectional shapes, for example, rectangular, ‘D’ sections or ice-coated power-line cables. It is usually characterized by low frequency and high amplitude oscillations in the transverse direction to the flow. It is related to the velocity of the incoming flow and the orientation of the structure with respect to the fluid flow and is considered as a non-linear aerodynamic phenomenon.

Flutter is a typical aeroelastic instability phenomenon like “buckling” in structures which occurs in flexible structures or their components. It is self-excited oscillations that produce diverging response beyond a critical speed of the upstream flow. In a linear structural system, at flutter the structure undergoes simple harmonic motion, with zero or negative net damping, resulting in large-amplitude oscillation that eventually results in structural failure. When a structure is subjected to wind, there are mean and fluctuating aerodynamic loads induced on the structure due to buffeting which initiates motions in the structure. As the structure oscillates, its orientation with respect to the airflow changes, resulting in modified aerodynamic loads on the structure that change with its orientation that could cause the structure to vibrate more. This fluid-structure interaction that is primarily motion-dependent produces large-amplitude response once the wind speed reaches a critical value known as flutter speed. This phenomenon, in which a flexible structure loses its ability to resist the aerodynamic loads due to loss of its mechanical damping or stiffness is known as flutter. Flutter can be divided into two types, “damping-driven” flutter that occurs in a single-mode of vibration because of negation of mechanical damping, and

"stiffness-driven" flutter, also known as classical flutter, that requires two or more modes of vibration to participate and results in a loss of stiffness in the structure. Damping-driven flutter generally occurs in structures with bluff-sectional shapes at relatively low-wind speeds, whereas stiffness-driven flutter occurs in structures with streamlined sectional shapes such as an airfoil and usually occurs at relatively high wind speeds.

Flutter is characterized by a cut-in speed for large-amplitude structural oscillations, that continue over a wide range of wind speeds beyond the cut-in speed, which is beneficial for wind energy harvesting compared to the other forced vibration phenomenon such as VIV which occurs over a limited range of wind speeds. The flutter boundary is very sensitive to Frequency ratio, Mass ratio and offset distance. Frequency ratio can be defined as the ratio of the vertical frequency of the suspension system to the torsional frequency of the suspension system (σ).

$$\sigma = \frac{f_h}{f_\alpha}$$

It is known that the flutter speed increases with increasing frequency ratio. There are certain frequency ratios at which the flutter speed becomes very small depending on the values of other parameters.

Mass ratio (μ) is defined as,

$$\mu = \frac{m}{\pi \rho B^2}$$

where m is the mass per unit length of the section model, ρ is the density of air, and B is the width of the section model. Considering the air density to be constant, as we increase the mass, the mass ratio (μ) increases, and as the mass ratio (μ) increases the flutter speed also increases.

Bisplinghoff, Ashley and Haffman (1955) classify the effects of chordwise offsets (distance of mass center from the mid-chord, e, and distance of elastic center from the mid-chord, a, both located behind the mid-chord) in terms of small and large Frequency ratio (σ). When σ is small they noted that generally flutter can happen only when the center of mass is behind the quarter-chord ($e > -1/2$, $a=0$). When σ is large they note that flutter can happen when the elastic axis is in front of quarter-chord ($a < -1/2$, $e=0$). Flutter does not appear to occur for any given σ when the mass center, elastic center and aerodynamic center all coincide ($e = a = -1/2$). These conclusions are based on a simplified model of the wing.

2.2 Past Work

Various structural cross-sections have been experimentally studied for wind energy harvesting by flow induced vibrations. Antonino [13] studied vortex induced vibrations of a B/D=4:1 rectangular cylinder. Gang Hu [14] investigated the efficiency of circular cylinder-based wind energy harvester with different rod-shaped attachments. Zhang [15] investigated wind energy harvesting by flow induced torsional vibration on a T-shaped cantilever beam. Wang [16] studied energy harvesting based on galloping of isosceles triangle section bluff bodies. Shan [17] presented a curved panel energy harvester for aeroelastic vibration. Wan Sun [18] experimented nested bluff body structure, two bluff bodies in tandem, for a vibro-wind galloping energy harvester. Jiantao Zhang [19] studied stepped beam structure for wind energy harvesting by galloping vibrations. L.B. Zhang [20] experimented ‘Y’ shaped bluff body structure for galloping-based electromagnetic energy harvester.

Numerical simulations would be beneficial to predict the aerodynamic loads and structural response in a fluid-structure interaction problem such as the one considered in this research for wind energy harvesting. Once validated by comparing with experimental data,

numerical simulations would help in a parametric study of a FIV wind energy harvester, optimize its design and predict its performance. Time-domain analysis using Rational function coefficients have been used to numerically predict the self-excited aerodynamic behavior of a structure and flutter speed. A previously developed algorithm (Cao and Sarkar [21]) for extracting rational function coefficients from a forced vibration technique uses the phase difference between simultaneously obtained displacement and aeroelastic load time histories. Even a slight error in the phase difference obtained from the experiments would contribute to significant error in the obtained rational function coefficients and flutter derivatives. Therefore, Chowdhury and Sarkar [22] presented a free vibration technique while Cao and Sarkar [7] presented a forced vibration technique that do not use this phase difference to extract the rational functions coefficients for a two degree of freedom dynamic system. These techniques were developed to extract the rational functions directly from the experimental data obtained from section model tests as opposed to using the flutter derivatives. These algorithms are more efficient than the alternate method of using flutter derivatives over a range of wind speeds as it requires data obtained at only two to three wind speeds to solve for the full set of rational function coefficients. However, these algorithms require time histories of aeroelastic loads on the section model along with those of the displacements of the model while it vibrates in free or forced vibration. Therefore, surface pressures on the section model need to be measured on the surface of the section model. Since measurement of aeroelastic loads can be challenging and cumbersome for certain cross-sections, an algorithm to extract the rational function coefficients directly from the flutter derivatives that are widely available in the literature and easier to extract for any cross section without using the aeroelastic loads will be very useful. There are two methods that can be followed for the same. In the first method, the time histories of the

displacements and aeroelastic loads associated with a particular cross-sectional shape of a structure can be numerically simulated using the flutter derivatives and then the rational function coefficients can be extracted using these time histories with the help of algorithms mentioned earlier. Alternately, the relationship between the flutter derivatives and the rational function coefficients can be used to develop an analytical technique to extract these coefficients from the flutter derivatives. This latter method was used here in this study to extract the rational function coefficients of the sections considered here. This formulation is presented below.

2.3 Equations of Motion

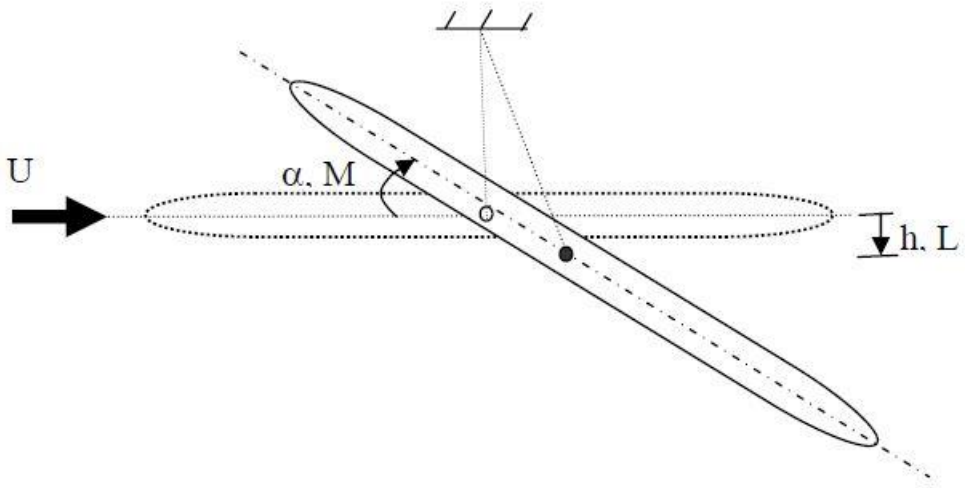

Figure 2.1 Illustration of Degrees of Freedom used for Wind Tunnel Tests

The self-excited (motion-induced) aerodynamic loads (lift L_{se} and moment M_{se}) per unit length for a two-DOF (vertical-torsional) dynamic system or section model (Figure 2.1) of a structural section in frequency domain are given by,

$$L_{se} = \frac{1}{2}\rho U^2 B\left[KH_1^*\left(\frac{\dot{h}}{U}\right) + KH_2^* B\left(\frac{\dot{\alpha}}{U}\right) + K^2 H_3^* \alpha + K^2 H_4^*\left(\frac{h}{B}\right)\right] \quad (2.1)$$

$$M_{se} = \frac{1}{2}\rho U^2 B^2\left[KA_1^*\left(\frac{\dot{h}}{U}\right) + KA_2^* B\left(\frac{\dot{\alpha}}{U}\right) + K^2 A_3^* \alpha + K^2 A_4^*\left(\frac{h}{B}\right)\right] \quad (2.2)$$

where, h and α are displacements, $\dot{h}$ and $\dot{\alpha}$ are velocities, of the dynamic system (Figure 2.1), $H_i^*$and A_i^*, i=1-8 are known as flutter derivatives which are functions of reduced frequency, $K = \frac{\omega B}{U}$, ρ is air density, ω is circular frequency, B is a characteristic length (model width), and U is mean wind speed upstream of the model.

The equations of motion for a 2-DOF (vertical and torsional) including self-excited loads can be written as,

$$m\,\ddot{h} + C_{hh}^{eff}\,\dot{h} - C_{h\alpha}^{eff}\,\dot{\alpha} + K_{hh}^{eff}\,h + K_{h\alpha}^{eff}\,\alpha = 0 \tag{2.3}$$

$$I\,\ddot{\alpha} + C_{\alpha\alpha}^{eff}\,\dot{\alpha} - C_{\alpha h}^{eff}\,\dot{h} + K_{\alpha\alpha}^{eff}\,\alpha + K_{\alpha h}^{eff}\,h = 0 \tag{2.4}$$

and these equations in matrix form,

$$\begin{bmatrix} m & 0 \\ 0 & I \end{bmatrix} \begin{bmatrix} \ddot{h} \\ \ddot{\alpha} \end{bmatrix} + \begin{bmatrix} C_{hh}^{eff} & C_{h\alpha}^{eff} \\ C_{\alpha h}^{eff} & C_{\alpha\alpha}^{eff} \end{bmatrix} \begin{bmatrix} \dot{h} \\ \dot{\alpha} \end{bmatrix} + \begin{bmatrix} K_{hh}^{eff} & K_{h\alpha}^{eff} \\ K_{\alpha h}^{eff} & K_{\alpha\alpha}^{eff} \end{bmatrix} \begin{bmatrix} h \\ \alpha \end{bmatrix} = \begin{bmatrix} 0 \\ 0 \end{bmatrix} \tag{2.5}$$

In the two degree of freedom model illustrated in Figure (2.1) and described by equation (2.5), m and I are defined as mass per unit length of the section model and moment of inertia per unit length of the section model, respectively, $\underline{K}^{eff}$ is effective stiffness matrix of the section model that includes the mechanical stiffness in terms of natural frequencies ω_h and ω_α in the vertical-DOF and torsional-DOF, and the aeroelastic stiffness in terms of the flutter derivatives $H_i^*$and A_i^*, i=3-4, $\underline{C}^{eff}$ is effective damping matrix of the section model that includes the mechanical damping in terms of critical damping ratios, ξ_h and ξ_α, in the vertical and torsional DOF, respectively, and the aeroelastic damping in terms of the flutter derivatives $H_i^*$and A_i^*, i=1-2. Equation (2.5) can be re-written as,

$$\underline{\ddot{q}} + \underline{C}^{eff}\,\underline{\dot{q}} + \underline{K}^{eff}\,\underline{q} = 0, \tag{2.6}$$

where, $\underline{\ddot{q}} = \begin{bmatrix} \ddot{h} \\ \ddot{\alpha} \end{bmatrix}$, $\underline{\dot{q}} = \begin{bmatrix} \dot{h} \\ \dot{\alpha} \end{bmatrix}$, $\underline{q} = \begin{bmatrix} h \\ \alpha \end{bmatrix}$

The aeroelastically modified equations of motions for 2-DOF in equation (2.6) can be represented as the state-space model in 2n-space,

$$\dot{\underline{X}} = \underline{A}\,\underline{X}, \text{ where } \underline{X} = \begin{bmatrix} \underline{q} \\ \dot{\underline{q}} \end{bmatrix}, \dot{\underline{X}} = \begin{bmatrix} \dot{\underline{q}} \\ \ddot{\underline{q}} \end{bmatrix}, \underline{A} = \begin{bmatrix} \underline{0} & \underline{I} \\ \underline{K}^{eff} & \underline{C}^{eff} \end{bmatrix} \tag{2.7}$$

where $\underline{K}^{eff}$ and $\underline{C}^{eff}$ are the effective stiffness and damping matrices of the order $n \times n$ including the aeroelastic terms as mentioned earlier.

$$\underline{K}^{eff} = \begin{bmatrix} K_{hh}^{eff} & K_{h\alpha}^{eff} \\ K_{\alpha h}^{eff} & K_{\alpha\alpha}^{eff} \end{bmatrix}, \underline{C}^{eff} = \begin{bmatrix} C_{hh}^{eff} & C_{h\alpha}^{eff} \\ C_{\alpha h}^{eff} & C_{\alpha\alpha}^{eff} \end{bmatrix}$$

The $\underline{A}$ matrix is a $2n \times 2n$ square matrix, where n is the number of degrees of freedoms and $\underline{I}$ is the identity matrix of the order $n \times n$ and $\underline{0}$ is a $n \times n$ null matrix. $\underline{A}$ matrix can be determined if the acceleration, velocity and displacement data are known for n degrees of freedom for at least $2n$ different instances of time. The $\underline{A}$ matrix determined from the zero-wind case will yield the mechanical stiffness and mechanical damping matrices for the suspension system and the section model. From the $\underline{A}$ matrix for non-zero wind cases the effective stiffness and damping matrices can be obtained from which the flutter derivatives at a particular normalized wind speed can be obtained. System identification methods such as ILS-method and modified ILS method, that were developed earlier by Sarkar and co-workers to accurately identify the $\underline{A}$ matrix from experimental data (displacement or acceleration), can be used.

2.4 Extraction of Rational Function Coefficients from Flutter Derivatives.

In this study, a formulation to extract the Rational function coefficients directly from the flutter derivative data is presented for a 2-DOF (vertical and torsional) system. Flutter derivatives $\underline{H_1^*}$, $\underline{H_2^*}$, $\underline{H_3^*}$, $\underline{H_4^*}$, $\underline{A_1^*}$, $\underline{A_2^*}$, $\underline{A_3^*}$ and $\underline{A_4^*}$ are the associated eight flutter derivatives of a coupled vertical-torsional motion of a dynamic system of a cross-sectional shape immersed in airflow

that describe the self-excited or aeroelastic loads (lift and moment) acting on it as formulated in equation (2.1). The vertical direct flutter derivative $\underline{H_1^*}$ is associated with the vertical velocity and influences vertical damping. The vertical direct flutter derivative $\underline{H_4^*}$ is associated with the vertical displacement and influences vertical stiffness. The torsional direct flutter derivative $\underline{A_2^*}$ is associated with the torsional velocity and influences torsional damping. The torsional direct flutter derivative $\underline{A_3^*}$ is associated with the torsional displacement and influences torsional stiffness.

Using one lag term for a two-DOF system, Chowdhury and Sarkar [21] derived the Rational function coefficient matrix $\underline{Q}$ of the order 2 × 2.

$$\underline{Q} = \begin{bmatrix} (\underline{A_0})_{11} + (\underline{A_1})_{11}\, p + \frac{(\underline{F})_{11} p}{p+\lambda} & (\underline{A_0})_{12} + (\underline{A_1})_{12}\, p + \frac{(\underline{F})_{12} p}{p+\lambda} \\ (\underline{A_0})_{21} + (\underline{A_1})_{21}\, p + \frac{(\underline{F})_{21} p}{p+\lambda} & (\underline{A_0})_{22} + (\underline{A_1})_{22}\, p + \frac{(\underline{F})_{22} p}{p+\lambda} \end{bmatrix} \tag{2.8}$$

where $\underline{Q}$ is the Rational function matrix consisting of four Rational functions coefficients. $\underline{A_0}$, $\underline{A_1}$, $\underline{F}$ and λ are the Rational function coefficients. $\underline{A_0}$ is the stiffness matrix, $\underline{A_1}$ is the damping matrix and $\underline{F}$ is the lag matrix, all of order 2 × 2, λ is the lag coefficient and p is the non-dimensional Laplace domain variable ($p = iK$).

$$\underline{Q_{11}} = (\underline{A_0})_{11} + (\underline{A_1})_{11}\, p + \frac{(\underline{F})_{11} p}{p+\lambda} \tag{2.9}$$

Substituting $p = iK$ in equation (2.9),

$$\underline{Q_{11}} = (\underline{A_0})_{11} + (\underline{A_1})_{11}\, iK + \frac{(\underline{F})_{11}\, iK}{iK+\lambda}$$

$$\underline{Q_{11}} = (\underline{A_0})_{11} + (\underline{A_1})_{11}\, iK + \frac{(\underline{F})_{11}\, iK\, (\lambda_L - iK)}{(\lambda_L + iK)(\lambda_L - iK)}$$

Grouping the real terms together and imaginary terms together,

$$\underline{Q_{11}} = \left[\, (\underline{A_0})_{11} + \frac{K^2 (\underline{F})_{11}}{(\lambda_L{}^2 + K^2)}\right] + i\left[\, K(\underline{A_1})_{11} + \frac{K\, \lambda_L\, (\underline{F})_{11}}{(\lambda_L{}^2 + K^2)}\,\right] \tag{2.10}$$

$$\text{Real}\ (\underline{Q_{11}}) = (\underline{A_0})_{11} + \frac{K^2(\underline{F})_{11}}{(\lambda_L{}^2+K^2)} \tag{2.11}$$

$$\text{Imag}\ (\underline{Q_{11}}) = K\ [(\underline{A_1})_{11} + \frac{\lambda_L\ (\underline{F})_{11}}{(\lambda_L{}^2+K^2)}\ ] \tag{2.12}$$

$$\underline{H_1^*} = \frac{\text{Imag}\ (\underline{Q_{11}})}{K^2} \tag{2.13}$$

$$\underline{H_4^*} = \frac{\text{Real}\ (\underline{Q_{11}})}{K^2} \tag{2.14}$$

where $\underline{H_1^*}$ and $\underline{H_4^*}$ are the flutter derivatives related to the Rational function coefficients,

$$\underline{H_1^*} = [\ \frac{(\underline{A_1})_{11}}{K} + \frac{\lambda_L\ (\underline{F})_{11}}{K\ (\lambda_L{}^2+K^2)}\ ]$$

$$\underline{H_1^*} = \frac{C_1}{K} + \frac{1}{K}\ [\ \frac{C_2C_3}{C_3^2+K^2}\ ] \tag{2.15}$$

where $C_1 = (\underline{A_1})_{11}$; $C_2 = (\underline{F})_{11}$; $C_3 = \lambda_L$.

$$\underline{H_4^*} = [\ \frac{(\underline{A_0})_{11}}{K^2} + \frac{(\underline{F})_{11}}{(\lambda_L{}^2+K^2)}\ ]$$

$$\underline{H_4^*} = \frac{C_4}{K^2} + \frac{C_2}{C_3^2+K^2} \tag{2.16}$$

where $C_4 = (\underline{A_0})_{11}$.

Multiplying equation (2.15) with K gives,

$$K\ \underline{H_1^*} = C_1 + \frac{C_2C_3}{C_3^2+K^2} \tag{2.17}$$

Multiplying equation (2.16) with C_3 gives,

$$C_3\ \underline{H_4^*} = \frac{C_3C_4}{K^2} + \frac{C_2C_3}{C_3^2+K^2} \tag{2.18}$$

Subtracting (2.18) from (2.17) gives,

$$K\ \underline{H_1^*}\ -\ C_3\ \underline{H_4^*} = C_1\ -\ \frac{C_3C_4}{K^2}$$

$$K\ \underline{H_1^*} = C_3\ \underline{H_4^*} + C_1\ -\ \frac{C_3C_4}{K^2}$$

$$Y\ (K_i) = \begin{bmatrix} 1 & \underline{H_4^*}\ (K_i) & \frac{-1}{K_i^2} \end{bmatrix} \begin{bmatrix} C_1 \\ C_3 \\ C_3 C_4 \end{bmatrix}$$

$$\begin{bmatrix} Y(K_1) \\ Y(K_2) \\ . \\ . \\ Y(K_n) \end{bmatrix} = \begin{bmatrix} 1 & \underline{H_4^*}\ (K_1) & \frac{-1}{K_1^2} \\ 1 & \underline{H_4^*}\ (K_2) & \frac{-1}{K_2^2} \\ . & . & . \\ . & . & . \\ 1 & \underline{H_4^*}\ (K_n) & \frac{-1}{K_n^2} \end{bmatrix} \begin{bmatrix} C_1 \\ C_3 \\ C_3 C_4 \end{bmatrix} \tag{2.19}$$

$$Y = \varphi\ X \tag{2.20}$$

Multiplying both sides of the equation (2.18) with φ^{T} gives,

$$\varphi^{\mathrm{T}}\ Y = \varphi^{\mathrm{T}}\ \varphi\ X$$

$$X = (\varphi^{\mathrm{T}}\ \varphi)^{-1}\ \varphi^{\mathrm{T}}\ Y \tag{2.21}$$

where, $X = \begin{bmatrix} C_1 \\ C_3 \\ C_3 C_4 \end{bmatrix}$, $Y = \begin{bmatrix} Y(K_1) \\ Y(K_2) \\ . \\ . \\ Y(K_n) \end{bmatrix} = \begin{bmatrix} K(1)\underline{H_1^*} \\ K(2)\underline{H_1^*} \\ . \\ . \\ K(\mathrm{n})\underline{H_1^*} \end{bmatrix}$, $\varphi = \begin{bmatrix} 1 & \underline{H_4^*}\ (K_1) & \frac{-1}{K_1^2} \\ 1 & \underline{H_4^*}\ (K_2) & \frac{-1}{K_2^2} \\ . & . & . \\ . & . & . \\ 1 & \underline{H_4^*}\ (K_n) & \frac{-1}{K_n^2} \end{bmatrix}$

X contains the rational function coefficients C_1, C_3 and C_4.

Also, from equation (2.17),

$$K\ \underline{H_1^*} = C_1 + \frac{C_2 C_3}{C_3^2 + K^2}$$

$$K\ \underline{H_1^*}\ - C_1 = \frac{C_2 C_3}{C_3^2 + K^2}$$

$$\begin{bmatrix} Z(K_1) \\ Z(K_2) \\ . \\ . \\ Z(K_n) \end{bmatrix} = \begin{bmatrix} \frac{C_3}{C_3^2 + K_1^2} \\ \frac{C_3}{C_3^2 + K_2^2} \\ . \\ . \\ \frac{C_3}{C_3^2 + K_n^2} \end{bmatrix} C_2 \tag{2.22}$$

$$Z = \theta\ C_2 \tag{2.23}$$

Multiplying both sides of the equation (2.23) with θ^T gives,

$\theta^T Z = \theta^T \theta\, C_2$

$C_2 = (\theta^T \theta)^{-1}\, \theta^T Z$ (2.24)

where, $\theta = \begin{bmatrix} \frac{C_3}{C_3^2+K_1^2} \\ \frac{C_3}{C_3^2+K_2^2} \\ . \\ . \\ \frac{C_3}{C_3^2+K_n^2} \end{bmatrix}$, $Z = \begin{bmatrix} Z(K_1) \\ Z(K_2) \\ . \\ . \\ Z(K_n) \end{bmatrix} = \begin{bmatrix} \mathrm{K}(1)\underline{H_1^*} - C_1 \\ \mathrm{K}(2)\underline{H_1^*} - C_1 \\ . \\ . \\ \mathrm{K}(\mathrm{n})\underline{H_1^*} - C_1 \end{bmatrix} = \begin{bmatrix} Y(K_1) - C_1 \\ Y(K_2) - C_1 \\ . \\ . \\ Y(K_n) - C_1 \end{bmatrix}$

Thus, using n values of $\underline{H_1^*}$, $\underline{H_4^*}$ and K, one can obtain C_1, C_2, C_3 and C_4, and hence the Rational function coefficients $(\underline{A_0})_{11}$, $(\underline{A_1})_{11}$, $(\underline{F})_{11}$ and λ_L. K is the non-dimensional reduced frequency, $K = \omega\, \mathrm{B}/\, \mathrm{U}$; ω is the angular frequency of oscillation and U is the test section mean wind velocity. Similarly, by solving $\underline{Q_{12}}$ {refer equation (2.8)} using $\underline{H_2^*}$, $\underline{H_3^*}$ and K, we can obtain$(\underline{A_0})_{12}$, $(\underline{A_1})_{12}$, $(\underline{F})_{12}$ and λ_L, by solving $\underline{Q_{21}}$ using $\underline{A_1^*}$, $\underline{A_4^*}$ and K, we can obtain$(\underline{A_0})_{21}$, $(\underline{A_1})_{21}$, $(\underline{F})_{21}$ and λ_M, and by solving $\underline{Q_{22}}$ using $\underline{A_2^*}$, $\underline{A_3^*}$ and K, we can obtain$(\underline{A_0})_{22}$, $(\underline{A_1})_{22}$, $(\underline{F})_{22}$ and λ_M. While solving these equations one gets two values of λ_L and λ_M, so the average of the two values are used to determine these parameters. Once the Rational function coefficients are derived from the set of flutter derivatives of a particular cross-section these can be used to predict the self-excited aerodynamic loads (lift, $L_{se}(\mathrm{t})$ and moment, $M_{se}(\mathrm{t})$) on this section and calculate its response using the following equations (Cao and Sarkar [7]).

$L_{se}(\mathrm{t}) = \frac{1}{2}\rho\, U^2\, B\, [\, ((\underline{A_0})_{11} + (\underline{F})_{11})\, \frac{h}{B} + (\underline{A_1})_{11}\, \frac{\dot{h}}{U} - (\underline{F})_{11}\, \frac{\lambda_L U}{B^2} \int_0^t e^{-\frac{U}{B}\lambda_L (t-\tau)}\, h(\tau)\, d\tau + ((\underline{A_0})_{12} + (\underline{F})_{12})\alpha + (\underline{A_1})_{12}\, \frac{B}{U}\dot{\alpha} - (\underline{F})_{12}\, \frac{\lambda_L U}{B} \int_0^t e^{-\frac{U}{B}\lambda_L (t-\tau)\alpha(\tau) d\tau}\,]$ (2.25)

$M_{se}(\mathrm{t}) = \frac{1}{2}\rho\, U^2 B^2 [\, ((\underline{A_0})_{21} + (\underline{F})_{21}\,)\,\frac{h}{B} + (\underline{A_1})_{21}\,\frac{\dot{h}}{U} - (\underline{F})_{21}\,\frac{\lambda_M U}{B^2}\int_0^t e^{-\frac{U}{B}\lambda_M (t-\tau)}\, h(\tau)\, d\tau + ((\underline{A_0})_{22} +$

$(\underline{F})_{22}\,)\alpha + (\underline{A_1})_{22}\,\frac{B}{U}\dot{\alpha} - (\underline{F})_{22}\,\frac{\lambda_M U}{B}\int_0^t e^{-\frac{U}{B}\lambda_M (t-\tau)}\alpha(\tau) d\tau]$ (2.26)

where τ is a dummy time variable that appears inside the integration.

The equations governing the motion of a statically and aerodynamically coupled section model about its center of mass are given by,

$\mathrm{M}\,[\ddot{h} + 2\xi_h\omega_h\,\dot{h} + \omega_h^2\, h + \omega_h^2\, r\,\alpha] = \mathrm{L_{ae}} + \mathrm{L_b}$ (2.27)

$\mathrm{I}\,[\ddot{\alpha} + 2\xi_h\omega_h\,\dot{\alpha} + \overline{\omega_h^2}\; h + \overline{\omega_\alpha^2}\,\alpha] = \mathrm{M_{ae}} + \mathrm{M_b}$ (2.28)

where M and I are mass and moment of inertia per unit length of the section model, r is the offset distance (distance between the elastic center and mass center).

$\overline{\omega_h^2} = \frac{M\omega_h^2\, r}{I}$, $\overline{\omega_\alpha^2} = [\frac{M}{I}\left(\frac{\omega_h^2}{\omega_\alpha^2}\right) r^2 + 1]$

Substituting the expressions for the self-excited lift ($\mathrm{L_{ae}}$) and aeroelastic moment ($\mathrm{M_{ae}}$) in terms of the Rational function coefficients, and assuming zero buffeting loads ($\mathrm{L_b}$, $\mathrm{M_b}$) in equations (2.27) and (2.28) for flutter analysis, the following equations can be written,

$\underline{\mathrm{I}}\,\underline{\ddot{q}} + \underline{C_m}\,\underline{\dot{q}} + \underline{K_m}\,\underline{q} = \underline{C_{ae}}\,\underline{\dot{q}} + \underline{K_{ae}}\,\underline{q} + \underline{F_{ae}}(\mathrm{t})$ (2.29)

$\underline{\mathrm{I}}\,\underline{\ddot{q}} + \underline{C_T}\,\underline{\dot{q}} + \underline{K_T}\,\underline{q} = \underline{F_{ae}}(\mathrm{t})$ (2.30)

$\underline{C_T} = \underline{C_m} - \underline{C_{ae}}$

$\underline{K_T} = \underline{K_m} - \underline{K_{ae}}$

$\underline{C_T}$ and $\underline{K_T}$ are effective stiffness and effective damping matrices of the order 2 × 2. In terms of the Rational function coefficients, the components of $\underline{C_T}$ and $\underline{K_T}$ can be written as,

$\underline{C_m} = \begin{bmatrix} 2\xi_h\omega_h & 0 \\ 0 & 2\xi_\alpha\omega_\alpha \end{bmatrix}$, $\underline{C_{ae}} = \frac{1}{2}\rho U^2 B \begin{bmatrix} \frac{(\underline{A_1})_{11}}{M} & \frac{(\underline{A_1})_{12}\, B}{M} \\ \frac{(\underline{A_1})_{21}}{I} & \frac{(\underline{A_1})_{22}\, B}{I} \end{bmatrix}$

$$\underline{K_m} = \begin{bmatrix} \frac{\omega_h^2}{\omega_h^2} & \frac{\omega_h^2\, r}{\omega_\alpha^2} \end{bmatrix}, \underline{K_{ae}} = = \frac{1}{2}\rho U^2 B \begin{bmatrix} \frac{(\underline{A_0})_{22}+(\underline{F})_{22}}{M} & \frac{(\underline{A_0})_{22}+(\underline{F})_{22}}{M} \\ \frac{(\underline{A_0})_{22}+(\underline{F})_{22}}{I} & \frac{(\underline{A_0})_{22}+(\underline{F})_{22}}{I} \end{bmatrix}$$

$$\underline{F_{ae}(t)} = -\frac{1}{2}\rho U^2 B \begin{bmatrix} (\underline{F})_{11}\, \frac{\lambda_L U}{MB^2} \int_0^t e^{-\frac{U}{B}\lambda_L (t-\tau)}\, h(\tau)\, d\tau + (\underline{F})_{12}\, \frac{\lambda_L U}{MB} \int_0^t e^{-\frac{U}{B}\lambda_L (t-\tau)} \alpha(\tau) d\tau \\ (\underline{F})_{21}\, \frac{\lambda_M U}{IB^2} \int_0^t e^{-\frac{U}{B}\lambda_M (t-\tau)}\, h(\tau)\, d\tau + (\underline{F})_{22}\, \frac{\lambda_M U}{I} \int_0^t e^{-\frac{U}{B}\lambda_M (t-\tau)} \alpha(\tau) d\tau \end{bmatrix}$$

The aeroelastically modified equations of motion (equation 2.30) can be written in state-space form as,

$$\dot{\underline{X}} = \underline{A}\,\underline{X} + \underline{F(t)} \tag{2.31}$$

where $\underline{F(t)} = \begin{bmatrix} \underline{0} \\ \underline{F_{ae}(t)} \end{bmatrix}$

where $\underline{0}$ is the null matrix of the order *2 × 1*.

Thus, using equations (2.25 and 2.26), the self-excited aerodynamic loads (Lift and Moment) in terms of extracted rational function coefficients and in equation (2.31) the response (displacement, velocity and acceleration) of any structure at wind speed below or equal to flutter speed can be numerically predicted in time domain.

2.5 Determination of Power Generation

In this study, the section model that is subjected to the airflow vibrates due to the fluid-structure interaction. Any vibrating object possesses Kinetic energy due to its motion. It is equal to the amount of work or potential energy needed to accelerate a given body of a given mass from rest to its stated velocity along a straight line.

$$\text{Kinetic Energy} = \frac{1}{2}\,\mathrm{M}v^2, \tag{2.32}$$

where M is the total mass of the section model and v is the time varying velocity of the vibrating section model in the vertical DOF.

A similar expression for the Kinetic energy can be written for torsional oscillation,

Kinetic Energy (KE) = $\frac{1}{2} I_T \dot{\alpha}^2$, (2.33)

where I_T is the total mass moment of inertia of the section model and $\dot{\alpha}$ is the time varying velocity of the vibrating section model in the torsional DOF.

Considering a cosine wave form for the vertical and torsional displacements of the section model with zero net damping which occurs at flutter, the vertical and torsional displacements can be defined as,

$h(t) = h_0 \cos(\omega_F t)$ (2.34)

$\alpha(t) = \alpha_0 \cos(\omega_F t)$ (2.35)

h_0 and α_0 is the steady-state amplitudes of the vertical and torsional displacement which can be determined from the wind tunnel experiments or numerical simulations. The first derivatives of the vertical and torsional displacements *h* and α gives the vertical and torsional velocities.

$\dot{h}(t) = -\omega_h h_0 \sin(\omega_F t)$ (2.36)

$\dot{\alpha}(t) = -\omega_\alpha \alpha_0 \sin(\omega_F t)$ (2.37)

$\dot{h}$ and $\dot{\alpha}$ are the corresponding velocities in the vertical and torsional DOF.

Average Kinetic Energy over one cycle of oscillation in the vertical DOF is given by,

$KE_{vertical} = \frac{1}{T} \int_0^T \frac{1}{2} M \dot{h}^2 \, dt$ (2.38)

The average power P_{avg} over one cycle of oscillation in the vertical DOF is given by,

$P_{avg} = \frac{1}{T^2} \int_0^T \frac{1}{2} M \dot{h}^2 \, dt$ (2.39)

$P_{avg} = \frac{M \omega_F^2 h_0^2}{2 T^2} \int_0^T sin^2(\omega_F t) \, dt$

$\int_0^T sin^2(\omega_F t) \, dt = \frac{T}{2}$

$$P_{avg} = \frac{M\,\omega_F{}^2\ h_0{}^2}{4\,T} \tag{2.40}$$

where T is the time period which is given by $T = \frac{2\,\pi}{w_F}$, ω_F is the effective frequency of oscillation at flutter.

$$P_{avg} = \frac{M\,\omega_h{}^3\ h_0{}^2}{8\,\pi} \tag{2.41}$$

The average power expression in equation (2.41) can be written in terms of non-dimensional parameters that are important for fluid-structure interaction problems, Scruton number (Sc), Reynolds number (Re), Reduced Velocity (RV), mass ratio (μ),

$$P_{avg} = \pi\ (\frac{h_0}{B})^2\ (Sc)(Re^2)\left(\frac{1}{RV^2}\right)\left(\frac{1}{\mu}\right)(\ \frac{M\,f_h\,\upsilon^2}{\xi_m\ B^2}) \tag{2.42}$$

$$Sc = \frac{M\,\xi_m}{L\,\rho\,B^2} \tag{2.43}$$

$$RV\ = \frac{U}{f_h\,B} \tag{2.44}$$

$$Re = \frac{U\,B}{\upsilon} \tag{2.45}$$

$$\mu = \frac{M}{\pi\,\rho\,B^2 L} \tag{2.46}$$

$$\upsilon = \frac{\mu}{\rho} \tag{2.47}$$

where Sc is the Scruton number, Re is the Reynolds number, RV is the Reduced Velocity, μ is the mass ratio, B is the width of the section model, L is the length of the section model, M is the inertial mass of the system, f_h is the vertical frequency in Hz, ξ_m is the mechanical damping ratio at zero wind speed, υ is the kinematic coefficient of viscosity, μ_s is static coefficient of viscosity, ρ is air density, and U is the mean wind speed. From equation (2.41), as the frequency of oscillation increases P_{avg} will increase, but the flutter speed will increase for a given critical

reduced velocity. From equation (2.42), it is known that as the Scruton number increases P_{avg} will increase, but then as the Scruton number increases the amplitude of vibration decreases proportionally, so the power generation might decrease. Thus, these parameters are all inter-related and need to be determined carefully for ideal power generation.

Similarly, the average power over one cycle of oscillation in the torsional DOF is given by,

$$P_{avg} = \frac{I_T\ \omega_F{}^3\ \ \alpha_0{}^2}{8\ \pi} \tag{2.48}$$

Thus, the average power generated when the model is vibrating in a coupled vertical-torsional motion at flutter with modal amplitudes of vertical and torsional vibrations h_0 and α_0, where the net damping is zero and the vertical and torsional frequencies are equal to the flutter frequency (ω_F), is given by,

$$P_{avg} = \frac{M\ \omega_F{}^3\ \ h_0{}^2}{8\ \pi} + \frac{I_T\ \omega_F{}^3\ \ \alpha_0{}^2}{8\ \pi} \tag{2.49}$$

$$P_{avg} = \frac{\omega_F{}^3}{8\ \pi}\left(\ M\ h_0{}^2 + I_T\ \ \alpha_0{}^2\right) \tag{2.50}$$

Writing equation of motion for the vertical DOF,

$$M\left[\ddot{y} + 2\xi_m\omega_m\dot{y} + \omega_m^2\ y\right] = F_a \tag{2.51}$$

where F_a is the self-excited force without the aerodynamic stiffness for simplification.

$$M\left[\ddot{y} + 2\xi_m\omega_m\dot{y} + \omega_m^2\ y\right] = \frac{1}{2}\rho U^2 B\mathrm{L}\ K H_1^*\frac{\dot{y}}{U} \tag{2.52}$$

Equating the $\dot{y}$ terms,

$C_m = 2M\ \xi_m\omega_m$ is the mechanical damping in the system

$C_a = -\frac{1}{2}\rho U^2 B\mathrm{L}\ K\frac{H_1^*}{U}$ aero-elastic damping in the system

Substituting $K = \omega_m B/\ U;$

$C_a = -\frac{1}{2}\rho B^2 L\omega_m H_1^*$, is the aeroelastic damping. (2.53)

$\xi_a = \frac{C_a}{2M\omega_m} = -\frac{\rho B^2 L H_1^*}{4M}$ is the aeroelastic damping ratio. (2.54)

$C_m = C_{mech} + C_M$ is the total mechanical damping from springs (C_{mech}) and a linear generator (C_M)

$\xi_m = \frac{C_{mech}}{2M\omega_m} + \frac{C_M}{2M\omega_m} = \xi_{mech} + \xi_M$, is the total mechanical damping ratio

$\xi_T = \xi_{mech} + \xi_M + \xi_a$, where ξ_T is the total damping of the system.

At flutter the total damping in the system is zero. When $\xi_T < 0$, the system exhibits a diverging motion.

The damping force F_M in a linear-actuator type generator will be due to electromagnetic force that can be written as,

$F_M = C_M\dot{y} = N\, I_C\, L_C\, B_M$ (2.55)

where B_M is the magnetic strength, L_C is the length of one coil, N is the number of coils, and I_C is the current in each coil.

$C_M\dot{y} = N\frac{|E|}{R_C} L_C B_M$, where $|E|$ is the electromotive force or voltage generated and R_C is the resistance in each coil.

$C_M\dot{y} = N\frac{d\phi_B/dt}{R_C} L_C B_M = N\frac{B_M L_C v}{R_C} L_C B_M$ (2.56)

where $I_C = \frac{B_M L_C v}{R_C}$, ϕ_B is magnetic flux and $v = \dot{y}$.

$C_M = \frac{N\,(B_M L_C)^2}{R_C}$ and $\xi_M = \frac{N\,(B_M L_C)^2}{2M\omega_m R_C}$ (2.57)

Average power in the generator is given by,

$P_{avg} = \frac{1}{T}\int_0^T I_C^2\, R_C\, dt\, N = \frac{1}{T}\left(\frac{B_M L_C}{R_C}\right)^2 R_C N \int_0^T v^2 dt$ (2.58)

Now, $\int_0^T v^2 \mathrm{dt} = A^2\omega_m^2 \frac{T}{2}$, where A is the amplitude of the simple-harmonic oscillation

$P_{avg} = \frac{1}{T}\left(\frac{B_M L_C}{R_C}\right)^2 R_C \mathrm{N}\, A^2\omega_m^2 \frac{T}{2} = \frac{\mathrm{N}\,(B_M L_C)^2}{R_C}\frac{A^2\omega_m^2}{2}$

$P_{avg} = \frac{\mathrm{N}\,(B_M L_C)^2}{R_C}\frac{A^2\omega_m^2}{2} = 2M\omega_m\xi_m \frac{A^2\omega_m^2}{2}$, using equation (2.57)

$$P_{avg} = M\xi_M A^2\omega_m^3 \tag{2.59}$$

$$P_{avg} = M\xi_M\left(\frac{A}{B}\right)^2\omega_m^3 B^2 \tag{2.60}$$

Equation (2.60) estimates the average power that can be captured from the vibrating section model in a single DOF using a linear generator.

Now, it is known that ξ_T is zero at flutter.

$\xi_T = \xi_{mech} + \xi_M + \xi_a = 0$

$\xi_M = -\xi_{mech} - \xi_a$

$$\xi_M = \frac{\rho B^2 L H_1^*}{4M} - \xi_{mech} + \frac{\rho B^2 L H_1^*}{4M} \tag{2.61}$$

$\frac{M\xi_M}{\rho B^2 L} = \frac{H_1^*}{4} - \frac{M\xi_{mech}}{\rho B^2 L} + \frac{H_1^*}{4}$

$$\frac{4M\xi_M}{\rho B^2} = H_1^* - 4S_C \tag{2.62}$$

Equation 2.62 gives the maximum damping ratio of the linear actuator that can be sustained in the system at flutter, where S_C is the Scruton number and H_1^* is the flutter derivative value at flutter speed.

CHAPTER 3. EXPERIMENTAL SET-UP

3.1 Wind Tunnel Test Set-up

This chapter describes the wind tunnel tests including the design and fabrication of the section models and the test setup of the suspension system that was used to test the characteristic vibration response of these models in a range of wind speeds. All the experiments were performed in the Aerodynamic and Atmospheric Boundary Layer (AABL) Wind and Gust tunnel located in the Wind Simulation and Testing Laboratory (WiST Lab) that is located in the Department of Aerospace Engineering at Iowa State University (ISU). This wind tunnel consists of two test sections, one is the aerodynamic test section, whose width and height are 2.44 m (8.0 ft) and 1.83 m (6.0 ft), respectively, and the maximum wind speed capacity is 53 m/s (173.9 ft/s). Another section is the ABL test section, whose width and height are 2.44 m (8.0 ft) and 2.21 m (7.25 ft), respectively, and the maximum wind speed capacity is 40 m/s (131 ft/s). The wind tunnel tests were carried out in the aerodynamic test section where the upstream flow was smooth and uniform across the test section. Figure (3.1) shows the interior of the test section with a section model of a rectangular section (B/D = 1) model suspended by a set of springs. To determine the mechanical frequency and damping of the suspended system consisting of the model and the springs, the model is deflected manually by introducing a small initial displacement along a particular degree of freedom (DOF) and released. For example, to estimate the vertical frequency and damping, the model is displaced evenly by a small amplitude in the vertical DOF. Similarly, to estimate the torsional frequency and damping, the model is displaced evenly by a small amplitude in the torsional DOF. From the recorded time history of the model in free vibration, the mechanical frequency and damping of the system is estimated for each section model tests along each DOF (vertical or torsional).

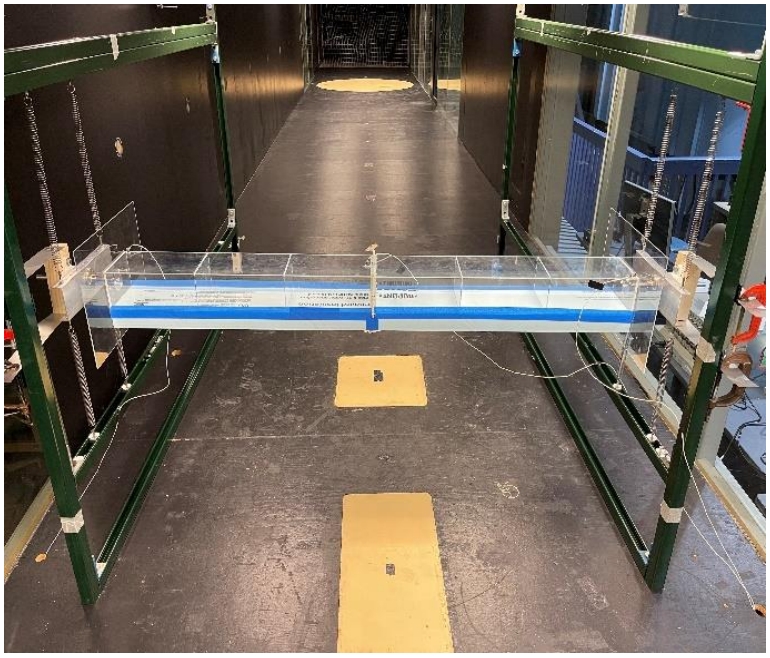

Figure 3.1 Test section interior with suspended section model

After suspending the model in the test section of the wind tunnel, the data acquisition equipment and power supply cords were connected. Initial fine-tuning of the model-spring system are important to ensure correct operation of the suspension system.

3.2 Suspension System

The basic design of the suspension system was inspired by Sarkar et al. [23]. The suspension system comprises of the following components as described below,

i. A ‘C’ or channel section: Two C sections, one at each end of the model, were used to connect the springs and the model. Holes were drilled on the top and bottom of the C section to connect the vertical springs. There are a total of ten holes drilled at an interval of 1 inch, so that the horizontal distance between the vertical springs connected to the top and bottom of the C section can be varied to change the torsional stiffness of the system

while keeping the vertical stiffness constant, and thereby change the frequency ratio (ratio of vertical to torsional frequency). Since this study involves determining the effect of frequency ratio on critical flutter speed, the distance between the springs need to be adjusted to achieve different frequency ratios. Two wooden blocks with rectangular cross section were designed, each with a ball bearing at its center, to connect the section model to the C section. The wooden blocks and ball bearings with plastic housing were used to keep the mass of the suspension system low. The ball bearing, housed inside the wooden block, on either side of the suspension system supported the section model horizontally while allowing it to vibrate smoothly in torsional DOF. The section model was built by joining two smaller models of equal length (referred here as half-model). An aluminum rod of length and diameter 0.75 m and 0.0127 m, respectively, was used to support the half-model in the suspension system assembly and to enhance the rigidity of the model. Rigidity is an important factor in dynamic testing because if the section model flexes while it is subjected to aeroelastic induced motion, then the dynamic response characteristics would change drastically. The aluminum rod goes through the center of each half-model and a larger end plate on one end of the model. The larger end plates were fixed to the aluminum rod with a locknut while being flushed to the model on its inside. One end of the rod goes through a hole at the center of the horizontally spanning C section on either side of the section model and were connected to the ball bearing inside the wooden bock which is located outside the horizontally spanning C section. Two leaf springs were attached to the wooden block, one on top and one to the bottom of the wooden block using screws and washers at one end while the other ends of the leaf springs were attached to the steel frame using ‘C’ clamps. The two pairs of leaf springs

restrained the two wooden blocks and hence the section model from moving in the lateral or along-wind direction while allowing vertical motion of the model and the ball bearing within the wooden block allowed torsional motion of the model. One smaller end plate was fixed to the other end of the half-model. Two such half-models, each 0.75 m long, were connected by overlapping the smaller end plates and connecting them to form one section model. Figure (3.2) shows the section model suspended in the suspension system.

ii. The suspension system has eight springs in total. Each side of the suspension system has four springs, two springs are attached to the upper surface of the 'C' section and two springs are attached to the lower surface of the 'C' section. The other end of the springs is connected to the steel frame that supports the entire assembly of the suspension system. The spring stiffness (K) of each spring was estimated (as K = 1 lb. / inch) before selecting them as per the required stiffness and desired frequencies of the system. To estimate the accurate value of the mechanical frequency and damping of the system, the section model must oscillate evenly at both ends. If the model is not displaced evenly across its length, then the model does not oscillate accurately along the intended DOF. Therefore, it was ensured that the springs were aligned vertically without any tilt to achieve even vertical displacements. Similarly, the aluminum rods should be aligned properly through the ball bearing at either end of the model for the model to vibrate smoothly without any hindrance in the torsional DOF.

Figure 3.2 Suspension System used for the section model tests

3.3 Selective Cross-Sections for Model Study

The design, fabrication and geometric scaling of the models are significant in wind tunnel testing. Since this study focuses on the amount of energy that can be harvested from the vibrating model, mass and material of the models played key roles in the wind tunnel test results. To get significant amplitude of displacements it was critical to make the section models as light as possible. The scope of the current research was to develop a simple system that can harvest wind energy by means of flow induced vibrations and to validate the method of rational function extraction (as described in Chapter 2) from flutter derivatives that does not require the measurement of aeroelastic loads. Therefore, we needed only the displacement time histories to estimate the amount of power generation while pressure taps to measure surface pressures were not required.

The objective of this study was to build a system that could flutter at lower wind speed with high amplitude response in vertical or torsional or in a coupled vertical-torsional mode with a potential to generate maximum wind energy. Thus, it involved optimization by combining two sectional shapes into one, each having low-speed flutter characteristic in a single-DOF, to flutter in two degrees of freedom at even a lower wind speed than the individual sectional shape. Selective bluff sections are known to exhibit damping-driven flutter in a single-DOF. For example, it is known that rectangular sections of certain aspect ratios (width/depth) exhibit low wind speed flutter in the vertical DOF whereas 'H' shaped sections exhibit a low wind speed flutter in the torsional DOF. Therefore, in this study, five section models were selected for the experiments which include, (a) Rectangular section with B/D ratio of 1.5, (b) Rectangular section with B/D ratio of 1, (c) 'H' shaped sections (two configurations), and (d) 'π' shaped section. As stated earlier, mass or weight of the model is an important parameter in dynamic testing. The stiffness of the springs combined with the inertial mass of the oscillating system determines the natural frequency of the system. The two rectangular sections used had almost the same weight while the two 'H' shaped sections and 'π' shaped section had the same weight. The stiffness of the spring for all the tests remained the same. Thus, the frequency of the system changed between the rectangular and H/π shaped section models, which was determined from the free-vibration tests at zero wind speed performed in the wind tunnel. As mentioned earlier, the experiments involved only acquisition of the displacement time histories and no surface pressure measurements, making the design and fabrication of the section models to be simple because pressure taps (tiny holes) were not needed to be drilled on the surface of the model to attach the pressure tubes. In the experimental methods developed in the past [7], to extract rational

functions, the aeroelastic load (lift, moment and drag) time histories were required which required pre-drilled holes on the surface of the models for measurement of pressures.

The rectangular section with a width-to-depth ratio (B/D) of 1.5:1 used here is shown in Figure 3.3 (a). It is hollow and made out of plexiglass. A hollow model will have less mass than the solid model and plexiglass is used for the same purpose. Each of the four sides of the rectangular section is attached to the others using acrylic glue. Flat thin plates made of acrylic are used as spacers inside the hollow rectangular section to enhance the rigidity of the model. The prime objective of this study was to find the best possible combination of sections that will start to flutter at the lowest wind speed. Thus, all the models were constructed similarly, so that it is easier to mix and match two different sections to form one configuration of the section model. Thus, one configuration of rectangular sections with B/D=1.5, was made up of two identical units of rectangular section, whose length, chord length (B) and thickness or depth (D) are 0.75 m, 0.15 m, 0.10 m, respectively. These two identical rectangular sections were combined along the length of the model. The two identical sections were connected together with a smaller end plate at the center whose width, height and thickness are 0.17 m, 0.12 m, 0.003175 m, respectively. The outer ends of the two sections were connected to a larger end plate whose width, height and thickness are 0.45 m, 0.30 m, 0.003175 m, respectively, to allow 2D flow over the model and provide structural rigidity. All end plates were made out of plexiglass to reduce the overall mass of the section model. An aluminum rod goes through the center of each section of the model and the larger end plate. The larger end plate was connected to the aluminum rod at one end of the two sections of the model by a locknut. Set screws were used to prevent the rod from slipping out of the locknut. The entire section model (two half-model sections) was

attached to the suspension system as one unit. The total length, chord length and thickness of the bluff section model (B/D =1.5) are 1.5 m, 0.15 m, 0.10 m, respectively.

The rectangular section (Figure. 3.3 (b)) with a width-to-depth ratio (B/D) of 1:1 was made using the same identical rectangular half-model sections whose length, chord length and thickness are 0.75 m, 0.15 m, 0.10 m. The rectangular sections with B/D = 1.5 were converted to rectangular sections with B/D = 1 by increasing the dimension of its depth. To accomplish this, a rectangular piece of foam whose length, chord length and thickness are 0.75 m, 0.15 m, 0.05 m, respectively, was attached to the bottom of each half-model section to achieve the width-to-depth ratio (B/D) of 1:1. The total length, chord length and thickness of the rectangular section (B/D = 1) are 1.5 m, 0.15 m, 0.15 m, respectively.

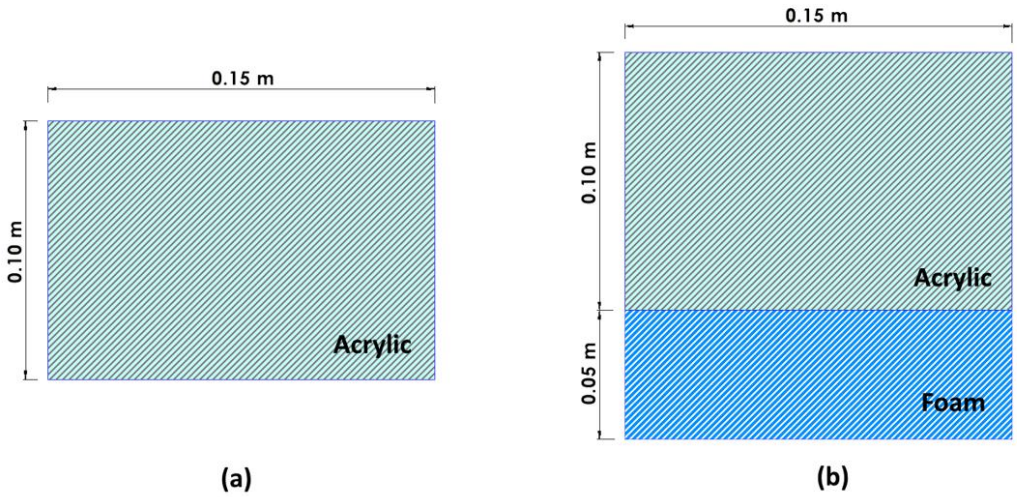

Figure 3.3 Rectangular section models, (a) B/D = 1.5, (b) B/D = 1

The ‘H’ section (Figure 3.4) consists of a horizontal plate which forms the flange of the ‘H’ section and two identical vertical plates which forms the web of the ‘H’ section. The

horizontal plate is a rectangular hollow section (half-model) and is made out of plexiglass whose length, chord length and thickness are 0.75 m, 0.15 m, 0.02m, respectively. The vertical plate was made out of plexiglass whose length, height, thickness is 0.75 m, 0.075m, 0.003175 m, respectively. Threaded holes were drilled along the centerline of the horizontal plate (0.02 m side) along its length so that the vertical plates can be connected on both the sides with screws. Similar to the rectangular section, the 'H' section is also made up of two identical half-model sections (made of identical horizontal and vertical plates) which could be combined along the length of the model with a smaller end plate at the center whose width, height and thickness are 0.17 m, 0.12 m, 0.003175 m, respectively, and a larger end plate at both ends of the section model whose width, height and thickness are 0.45 m, 0.30 m, 0.003175 m, respectively. The total length, chord length and thickness of the rectangular horizontal plates are about 1.5 m, 0.15 m, 0.02 m and the vertical plates are 1.5 m, 0.075 m, 0.003175 m, respectively.

There are three different configurations of the 'H' section as shown in the Figure (6). These different configurations are achieved by moving the location of the vertical plates with respect to the horizontal plate along the height. The vertical plates have a series of holes along its length drilled at different heights so that for each configuration the horizontal plate is connected to the corresponding series of holes on the vertical plates. The first 'H' section Figure 3.4 (a) is symmetric about the horizontal axis and is like a standard long-span bridge section. For the second 'H' section as shown in Figure 3.4 (b) the horizontal plate is moved up by 12.5 mm. For the third 'H' section as shown in Figure 3.4 (c) the horizontal plate is moved up further by 7.5 mm and the section resembles the symbol 'π', and hence will be referred here as a π section. The intention was to determine whether this geometrical change in the 'H' shape that includes the 'π' shape by moving the horizontal plate up will have an effect on the flutter speed and

amplitude in the torsional DOF. A hybrid section model, as shown in Figure 3.10, was made by combining two half-models of different sectional shapes, rectangular and H-shaped, to tap the vibration potential of each section in two different DOFs.

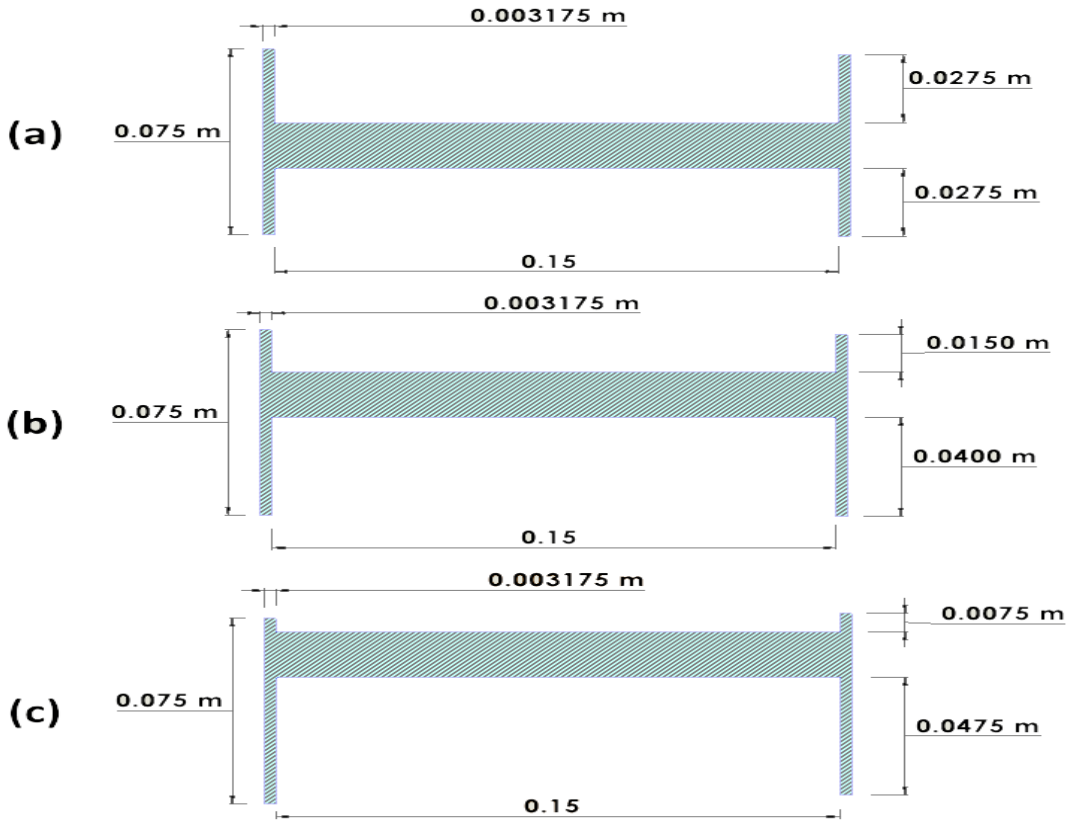

Figure 3.4 H-shape section models

In designing an experimental model, it is important to create CAD models of the proposed section geometries before fabrication. CAD models give the exact representation of how the final model will look like. Also, it is easier to make any changes to the model in CAD modeling, because once the model is built major modifications cannot be done. Thus, fabrication of the models was done once the CAD models were finalized.

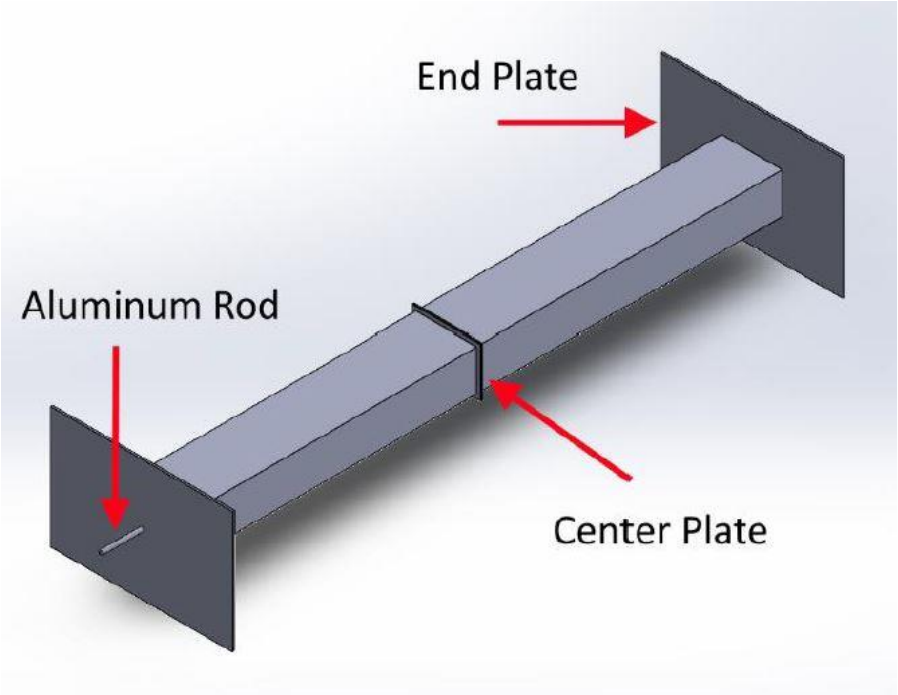

Figure 3.5 CAD drawing of Rectangular section (B/D = 1.5) assembly

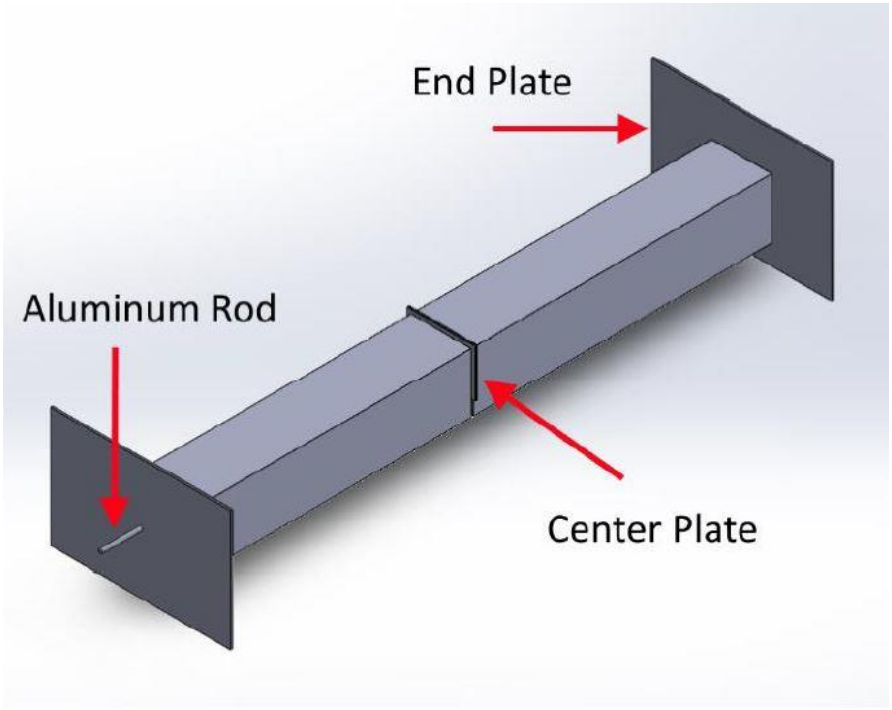

Figure 3.6 CAD drawing of Rectangular section (B/D = 1) assembly

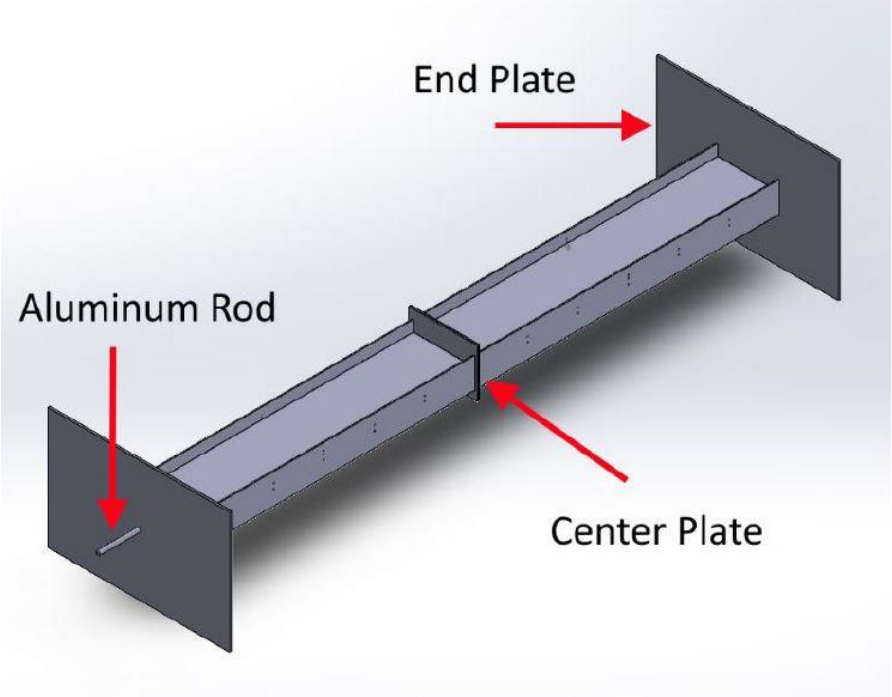

Figure 3.7 CAD drawing of ‘H’ section (Configuration 1) assembly

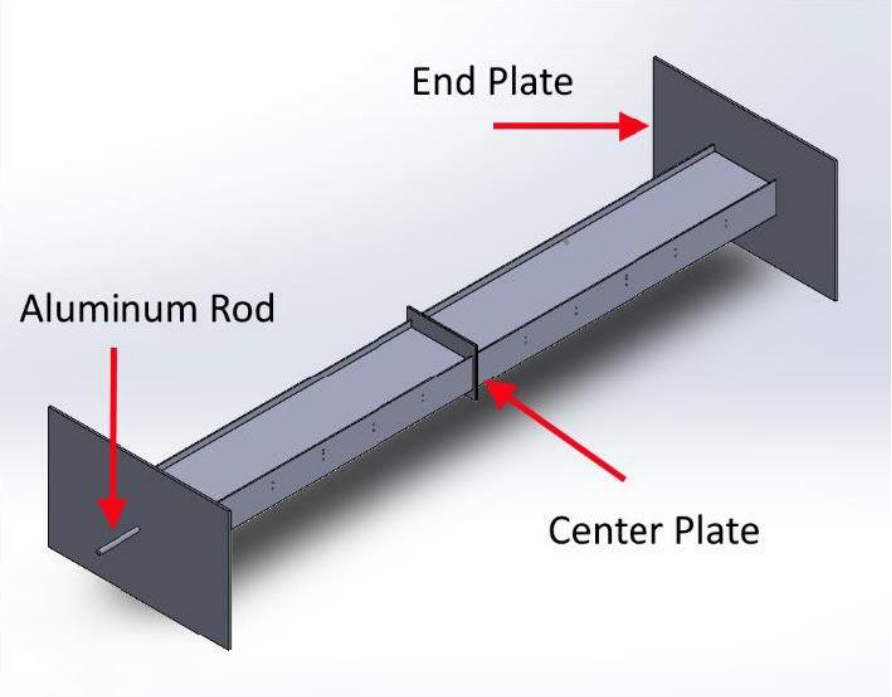

Figure 3.8 CAD drawing of ‘H’ section (Configuration 2) assembly

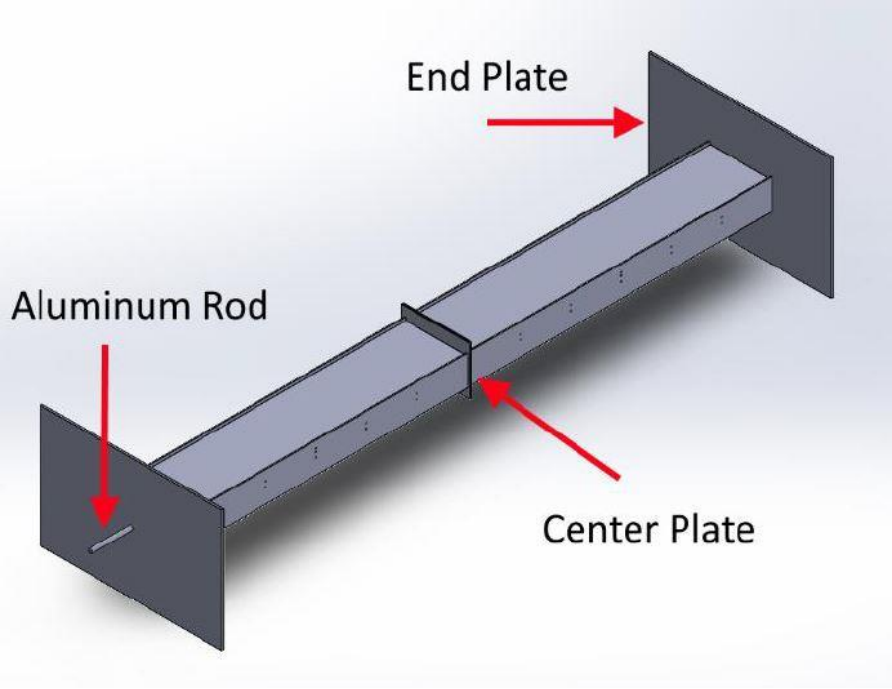

Figure 3.9 CAD drawing of 'π' section assembly

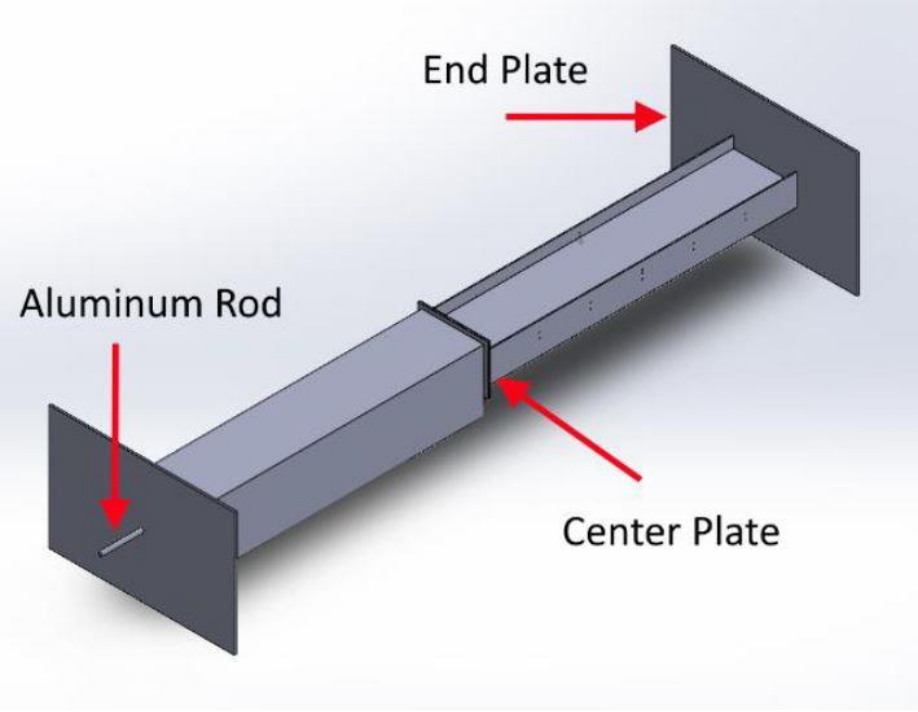

Figure 3.10 CAD drawing of Hybrid section (Rectangular and 'H' sections) assembly

3.4 Data Acquisition and Analysis

The displacement time histories were needed to assess the amplitude of vibration and to determine the power generated from the vibration of the section model. Accelerometers were used to record the acceleration time histories. From the recorded acceleration time histories, displacement time histories were calculated by integration. Three PCB Piezoelectronics accelerometers (352C65) were used to record the vertical and torsional accelerations. These accelerometers weigh 2.0 grams each and has a frequency range of 0.5 to 10,000 Hz. The sampling rate used for the acceleration measurement was 100 Hz. The total sampling time was set as 10 seconds (25 cycles or more) for all the tests. LabVIEW (National Instrument) was used for acceleration data acquisition. The accelerometers were glued on the top or bottom surface of the model using a heat gun (Figure 3.11). One accelerometer was fixed along its centerline, one at the windward edge and one at the leeward edge of the model. The distance between the accelerometer connected at the windward edge and the centerline is 0.0743 m and the distance between the accelerometer connected at the leeward edge and the centerline is 0.0737 m.

Experiments were carried out by increasing the mass and mass moment of inertia for all the section models, to understand the effect of mass ratio on flutter speed and Scruton number on the amplitude of vibration. To increase the mass, additional weights (0.25 Kg, 0.5 Kg and 1 Kg) were placed on the top surface of the model along the centerline of the model. The weights were taped along the surface of the model, so that it does not slip while the model is vibrating. To increase the mass moment of inertia, equal weights were placed on the top surface of the model one on the windward edge and other on the leeward edge. The distance between the weight on the windward edge and the centerline is equal to the distance between the weight in the leeward edge and the centerline. The distance between the two weights was measured to be 8 cm.

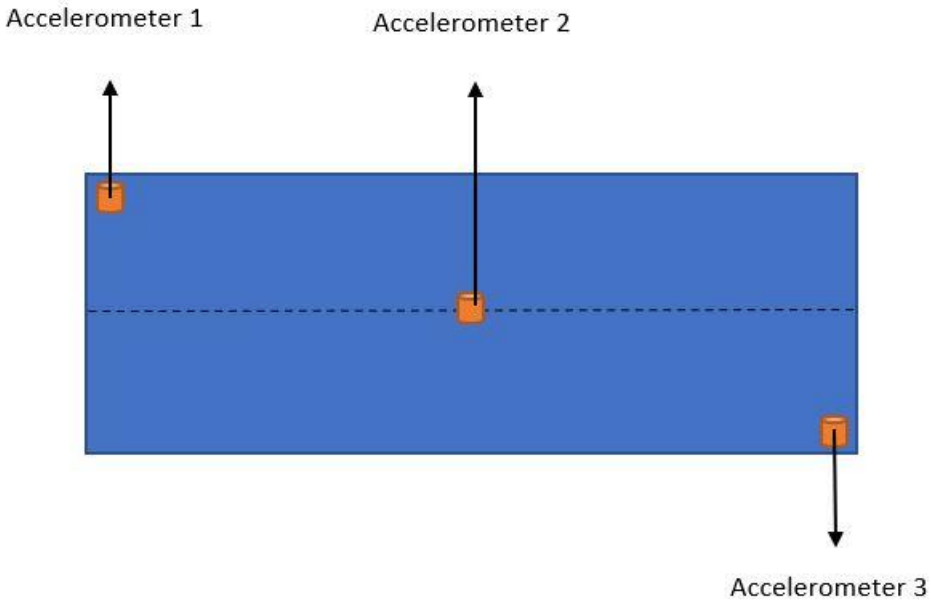

Figure 3.11 Accelerometer positions shown on the section model (top view)

The accelerometers that were attached to the model measures the acceleration of the model as it vibrates in the form of voltage. Each accelerometer has a unique calibration factor to convert the measured voltages into acceleration. The calibration factor for accelerometer 1 is 10.38 mV/m/s^2, accelerometer 2 is 10.56 mV/m/s^2 and accelerometer 3 is 10.58 mV/m/s^2. The accelerations were divided by the square of the cyclic natural frequency (ω) along a particular DOF to get the displacements of the vibrating model along that DOF. The distance between accelerometer 1 and the model mid-plane is 7.37 cm. The distance between accelerometer 3 and the model mid-plane is 7.43 cm. For calculating the vertical displacement, the average of all the three accelerometer values was used. The torsional displacement was calculated using the average torsional accelerations by using the two linear accelerations recorded by accelerometers 1 and 3. The acceleration from accelerometer 1 was divided by the distance between the mid-plane and accelerometer 1 (7.37 cm) to get the torsional acceleration of the model. The

acceleration from accelerometer 3 was divided by the distance between the mid-plane and accelerometer 3 (7.43 cm) to get the torsional acceleration of the model. These two torsional accelerations were averaged and then divided by the square of the torsional frequency to get the torsional displacement.

3.5 Methodology

Experiments were carried out by increasing the mass and mass moment of inertia for all the section models, to understand the effects of mass ratio on flutter speed and Scruton number on the amplitude of response. To increase the mass, additional weights (0.25 Kg, 0.5 Kg and 1 Kg) were placed on the top surface of the model along the centerline of the model. The weights were taped along the surface of the model, so that it does not slip while the model vibrates. To increase the mass moment of inertia, equal weights were placed on the top surface of the model symmetrically about the model's centerline, one on the windward edge and other on the leeward edge. The distance between the weights was measured to be 8 cm. The inertial mass of the section model is determined by increasing the mass of the model by adding additional weights (Δm) and recording the corresponding vertical frequency (ω_h). The additional weights (Δm) are plotted along the x-axis and the corresponding value of ($1/\omega_h^2$) are plotted along the y-axis. The slope of this curve gives $1/K_h$ and the y-intercept gives M/K_h, where K_h is the vertical stiffness of the section model and M is the inertial mass of the section model. The moment of inertia of the section model is determined by increasing the moment of inertia of the model by adding additional weights (Δm) at offset distances from the model centerline and recording the corresponding torsional frequency (ω_α). The incremental moment of inertia (ΔI) is plotted along the x-axis and the corresponding value of ($1/\omega_\alpha^2$) are plotted along the y-axis. The slope of this curve gives $1/K_\alpha$ and the y-intercept gives I_T/K_α, where K_α is the torsional stiffness of the section

model and I_T is the inertial mass of the section model. To estimate the vertical damping, the model was released from an initial displacement in the vertical DOF, and its free vibration was recorded. Similarly, to estimate the torsional damping, the model was released from an initial displacement in the torsional DOF, and its free vibration was recorded. From the recorded time history of the model in free vibration, the mechanical frequency and damping of the system is estimated for each section model tests along each DOF (vertical or torsional). A Pitot tube was kept downstream of the model along the centerline of the wind tunnel and was used to measure the mean wind velocity (U) of the flow. It gives the value of change in dynamic pressure (ΔP) which is calculated by subtracting the ambient pressure or static pressure (P_S) from the total pressure (P_T). Bernoulli's equation states that,

$$\Delta P = P_T - P_S = \frac{1}{2} \rho U^2 \tag{3.1}$$

$$U = \sqrt{\frac{(2\ \Delta P)}{\rho}} \tag{3.2}$$

The mechanical frequency is the number of cycles or vibrations the model undergoes over a period of time. From the acceleration time history, frequency can be determined by estimating the number of cycles over a period of time or time difference between the zero crossings. The damping ratio (ξ) can be written as,

$$\xi = \frac{1}{2\pi n} \ln \left(\frac{X_1}{X_n}\right) \tag{3.3}$$

where n is the number of cycles, X_1 is the amplitude of the first cycle of oscillation and X_n is the amplitude of the n^{th} cycle of oscillation. To estimate the flutter speed, acceleration time histories of the vibrating model were recorded once for four different wind speeds. The model parameters for all the cross-sections for different DOF tests are tabulated below.

Table 3.1 Model parameters for Vertical-DOF tests

Section Model	Vertical Frequency f_h (Hz)	Vertical Stiffness K_h (N/m)	Vertical Damping (ξ_h)	Mass M (Kg)
Rectangular (B/D=1.5)	2.5	1250	0.0012	5
Rectangular (B/D=1)	2.5	1250	0.0014	5

Table 3.2 Model parameters for Torsional-DOF tests

Section Model	Torsional Frequency f_α (Hz)	Torsional Stiffness K_α (Nm/rad)	Torsional Damping (ξ_α)	Moment of Inertia I_T (Kg m^2)
Rectangular (B/D=1.5)	5.1	24.51	0.0034	0.022
Rectangular (B/D=1)	4.9	37.04	0.0036	0.037
H (Configuration 1)	5	45.25	0.0042	0.045
H (Configuration 1)	4.7	37.45	0.0050	0.037
π	4.9	42.55	0.0055	0.043

Table 3.3 Model parameters for Vertical-Torsional DOF tests

Section Model	Vertical Frequency f_h (Hz)	Torsional Frequency f_α (Hz)	Vertical Stiffness K_h (N/m)	Torsional Stiffness K_α (Nm/rad)	Vertical Damping (ξ_h)	Torsional Damping (ξ_α)	Mass M (Kg)	Moment of Inertia I_T (Kg m^2)
Rectangular (B/D=1.5)	2.5	5.1	1250	24.51	0.0012	0.0034	5	0.022
Rectangular (B/D=1)	2.5	4.9	1250	37.04	0.0014	0.0036	5	0.037
Hybrid	2.5	4.8	1250	39.84	0.0019	0.0037	5	0.040

CHAPTER 4. RESULTS AND DISCUSSION

As stated earlier, the prime objective of this study is to device a flutter-driven wind energy harvester that can be used to extract wind energy at reasonably low wind speeds through rigid-body motions. This study explored the amount of wind energy that can be extracted using the FIV (flutter-induced vibration) wind energy harvester, and the system parameters that improves its performance by appropriate selection of these parameters, which include cross-sectional shape, degrees of freedom, frequency ratio, mass ratio and the offset distance between the mass center and stiffness center. This chapter presents the experimental and numerical results of this study and discusses their implications.

To understand the effect of frequency ratio (ratio of vertical to torsional frequency) on flutter speed and amplitude of vibrations, experiments were performed with different frequency ratios by changing the torsional frequency of the system while keeping the vertical frequency as constant. This is done by changing the distance between the springs of the suspension system on either side of the model. To understand the effects of mass ratio on flutter speed and amplitude of vibration, experiments were performed by adding additional weights to the system, thereby, increasing the mass of the section model. To study the effects of offset distance of the pivot point from the mass center on flutter speed and amplitude of vibration, the torsional axis of the section model was moved forward or backward in the along-wind direction, thereby creating a small offset, which is discussed in Section 4.3. Once we know the effects of frequency ratio, mass ratio and offset distance on the flutter speed, we can adjust the system parameters accordingly to enhance the performance of the FIV wind energy harvester. This chapter also gives a comparison of amplitudes of vertical and torsional displacements between the rectangular sections of B/D=1.5 and B/D=1, comparison of amplitudes of torsional displacement between the ‘H’

sections including the 'π' section and comparison of amplitudes of vertical and torsional displacements between the Hybrid section and the best performing rectangular section and 'H' section.

4.1 Estimating Flutter Speed

As the wind energy harvester continuously absorbs energy from the flow, the amplitude of vibration of the section model system will increase continuously and diverge at and beyond a critical wind speed, known as "flutter speed", as a result of loss of system damping in a 1-DOF system when the magnitude of negative aerodynamic damping becomes greater than that of the mechanical damping and as a result of loss of system stiffness in a coupled 2-DOF system. At wind speeds less than or equal to flutter speed, the system remains stable, and the linear equation(s) of motion is applicable. As the wind speed increases and approaches the flutter speed, the amplitude of vibration also increases, and eventually the system develops a constant amplitude motion at the flutter speed. Beyond the flutter speed the system becomes unstable, the linear equations are not valid anymore and the system is observed to exhibit a limit-cycle type motion of vibration with higher amplitude than that at flutter speed. Thus, the flutter speed is the boundary of the wind speed that differentiates a stable and an unstable system. Thus, it is important to identify the flutter speed of the FIV wind energy harvester which should be as low as possible for targeting maximum wind capture.

Flutter derivatives (defined in Chapter 2) can be used to predict the flutter speed of a section. The direct flutter derivative $\underline{H_1^*}$ is associated with the vertical velocity in the vertical degree of freedom (DOF) for a vertical-torsional or vertical-only system. In the reduced velocity vs $\underline{H_1^*}$ plot, the point at which the $\underline{H_1^*}$ changes its sign, from negative to positive, indicates a regime approaching onset of flutter for that section in the single-DOF (vertical) system. The

direct flutter derivative $\underline{A_2^*}$ is associated with the torsional velocity in the torsional DOF for a vertical-torsional or torsional-system. Similarly, in the reduced velocity vs $\underline{A_2^*}$ plot, the point at which the $\underline{A_2^*}$ changes its sign, from negative to positive, indicates a regime approaching onset of flutter for that section in the single-DOF (torsional) system.

For each test, acceleration of the vibrating model was recorded for multiple wind speeds. The measured accelerations were converted to displacements as mentioned in Chapter 2. Reduced velocity is the non-dimensional form of wind speed. It is given by,

Reduced velocity of vertical DOF = $\frac{U f_h}{B}$

Reduced velocity of torsional DOF = $\frac{U f_\alpha}{B}$

where, U is the mean wind speed, f_h the vertical frequency of vibration, f_α is the torsional frequency of vibration and B is the width of the section model. The vertical displacement is also converted into a non-dimensional form by dividing it with the width of the section model (B).

Figures 4.1, 4.2 and 4.3 shows the acceleration time history of the rectangular section (B/D=1.5) at various wind speeds 2.89 m/s, 4.1 m/s and 4.57 m/s. At low wind speeds, the model exhibits diverging motion with varying amplitude. At higher wind speeds 4.08 m/s and 4.57 m/s, the model exhibits almost constant amplitude motion.

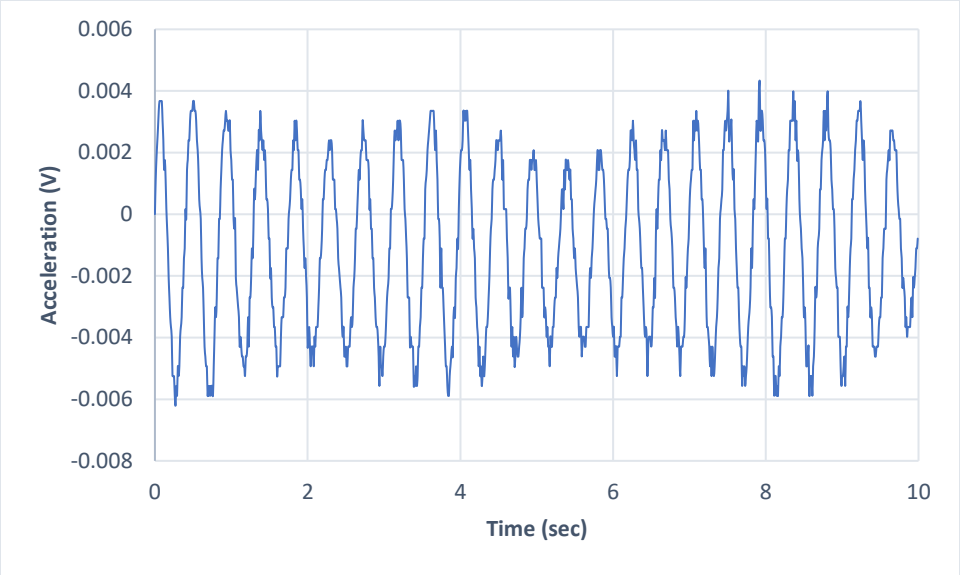

Figure 4.1 Acceleration Time History of Rectangular Section (B/D=1.5) at 2.89 m/s

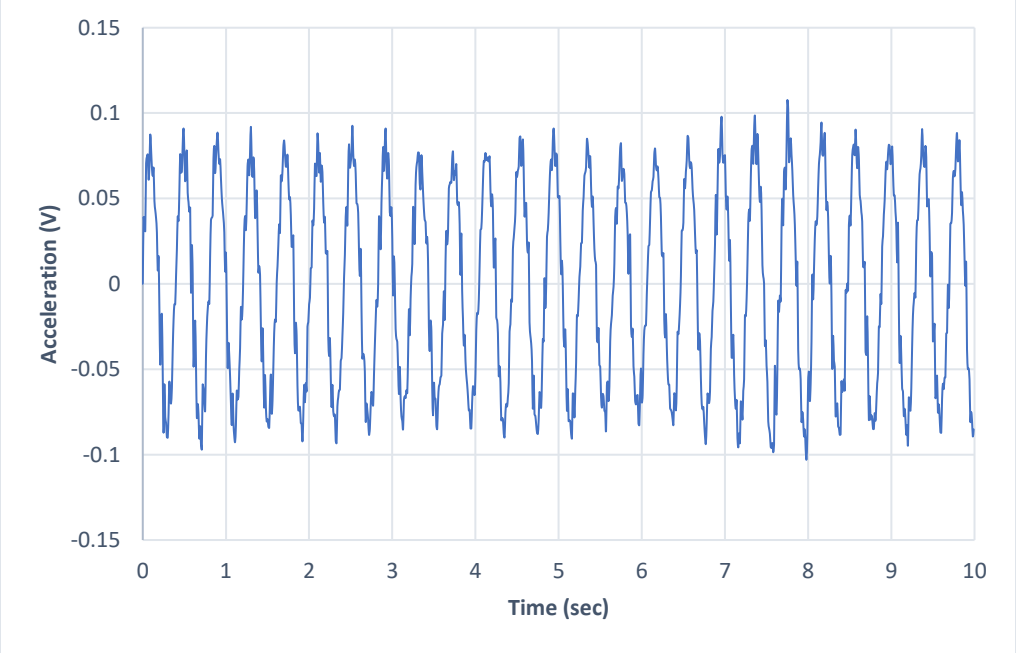

Figure 4.2 Acceleration Time History of Rectangular Section (B/D=1.5) at 4.1 m/s

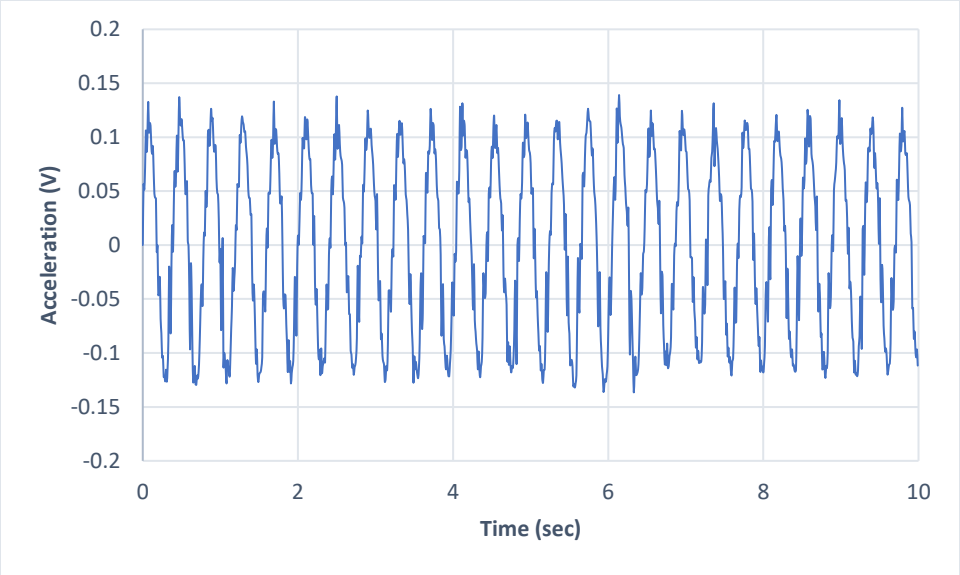

Figure 4.3 Acceleration Time History of Rectangular Section (B/D=1.5) at 4.57 m/s

The RMS (root mean square) of the vertical displacement in non-dimensional form in vertical-DOF only tests is plotted against the reduced velocity in the vertical DOF to find the flutter speed of the system vibrating in the vertical DOF. An exponential curve is fitted through the data set. The reduced velocity where the RMS vertical displacement reaches a large value asymptotically as determined by the exponentially fitted curve determines the flutter speed in the vertical DOF. However, for practical purpose, the reduced velocity at which the normalized vertical RMS amplitude reaches 0.5 is considered here as the flutter speed in the vertical DOF as beyond this point the system enters the unstable region.

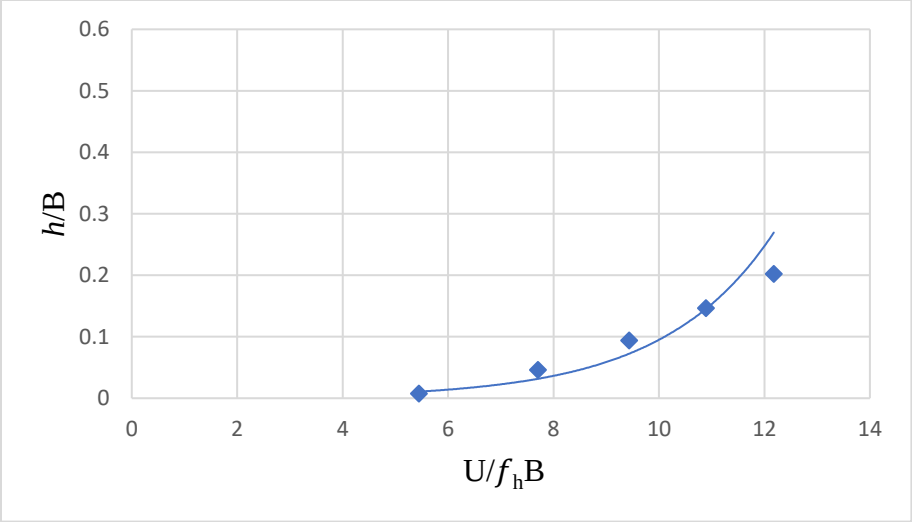

Figure 4.4 Normalized Vertical RMS amplitude versus reduced velocity for the Rectangular section, Vertical-DOF (B/D=1.5)

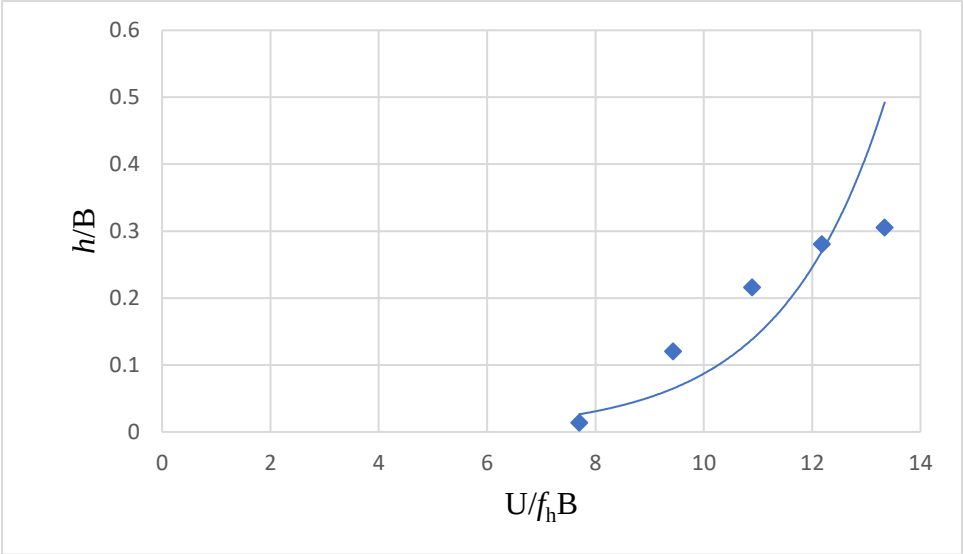

Figure 4.5 Normalized Vertical RMS amplitude versus reduced velocity for the Rectangular section, Vertical-DOF (B/D=1)

Similarly, the RMS of the torsional displacement in torsional-DOF only tests (with vertical DOF restrained) is converted into units of degrees and plotted against the reduced velocity. An exponential curve is fitted through the data set. The reduced velocity where the

RMS torsional displacement reaches a large value asymptotically as determined by the exponentially fitted curve determines the flutter speed in the torsional DOF. However, for practical purpose, the reduced velocity at which the torsional RMS amplitude reaches 5 degrees is considered here as the flutter speed in the torsional DOF as beyond this point the system enters the unstable region.

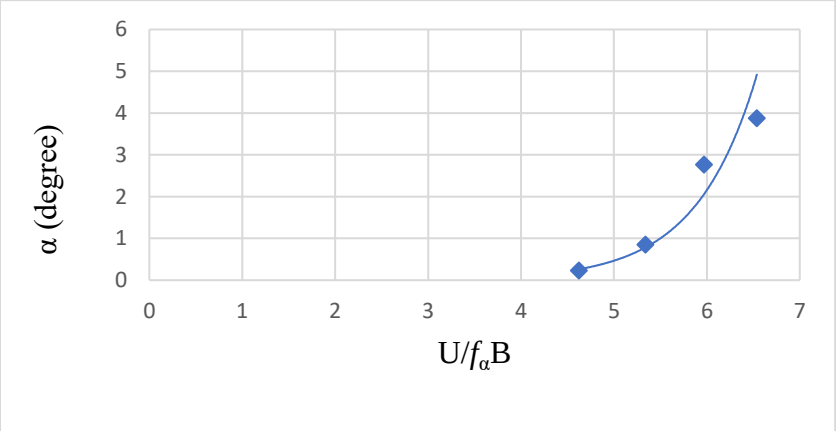

Figure 4.6 Torsional RMS amplitude vs reduced velocity for Rectangular section (B/D=1.5)

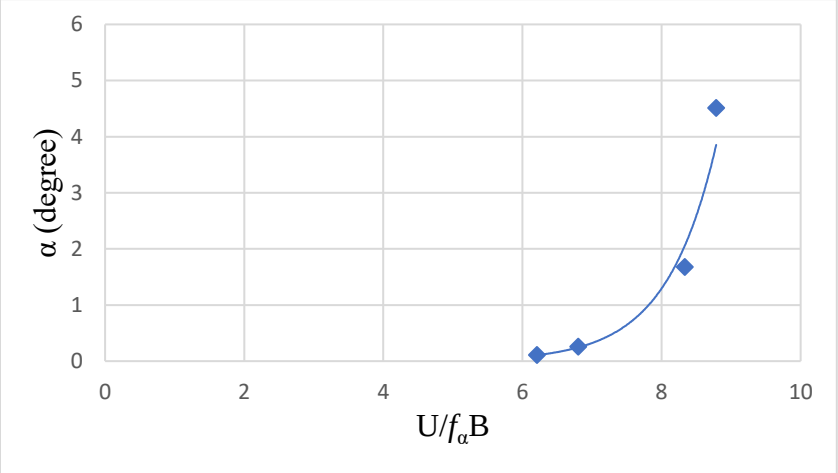

Figure 4.7 Torsional RMS amplitude vs reduced velocity for Rectangular section (B/D=1)

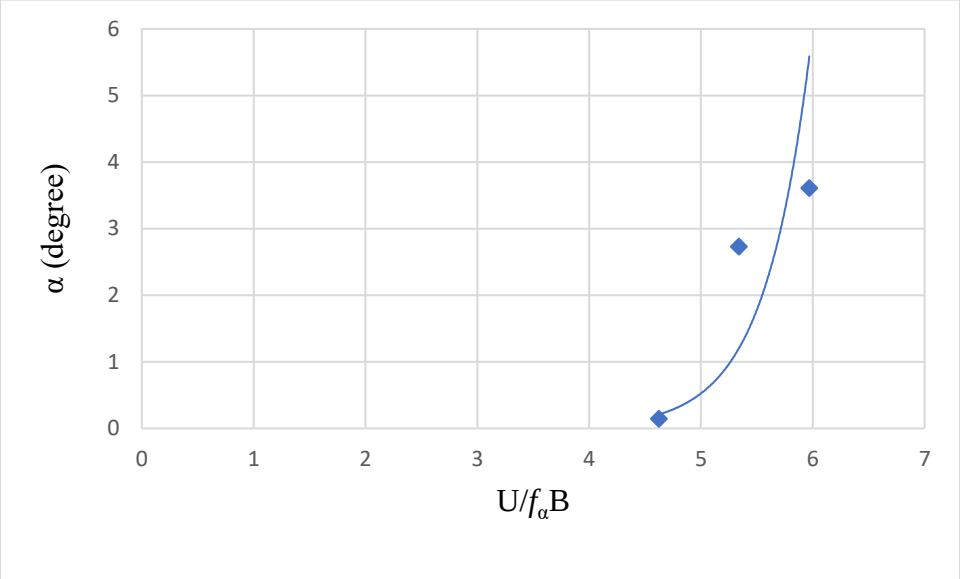

Figure 4.8 Torsional RMS amplitude vs reduced velocity for ‘H’ section (Configuration 1)

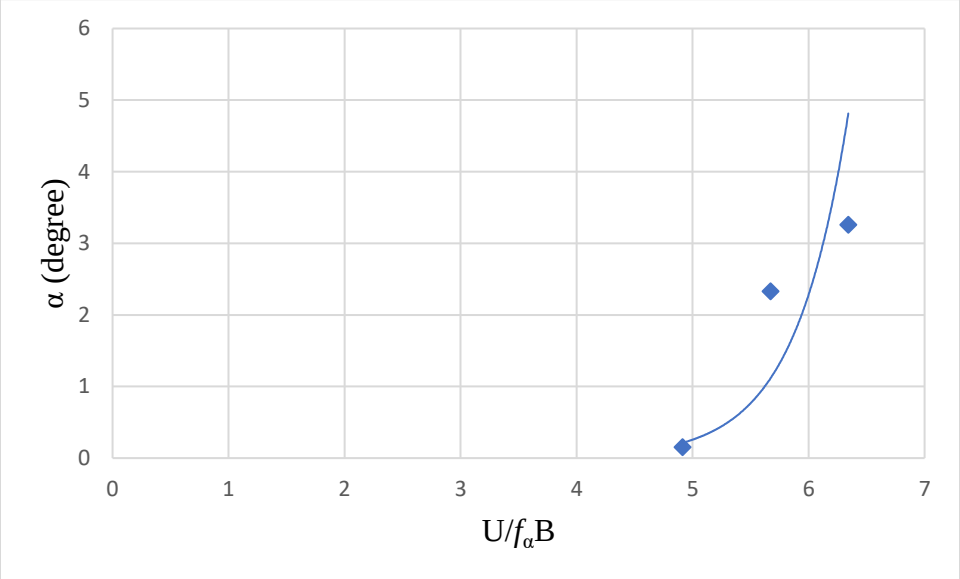

Figure 4.9 Torsional RMS amplitude vs reduced velocity for ‘H’ section (Configuration 2)

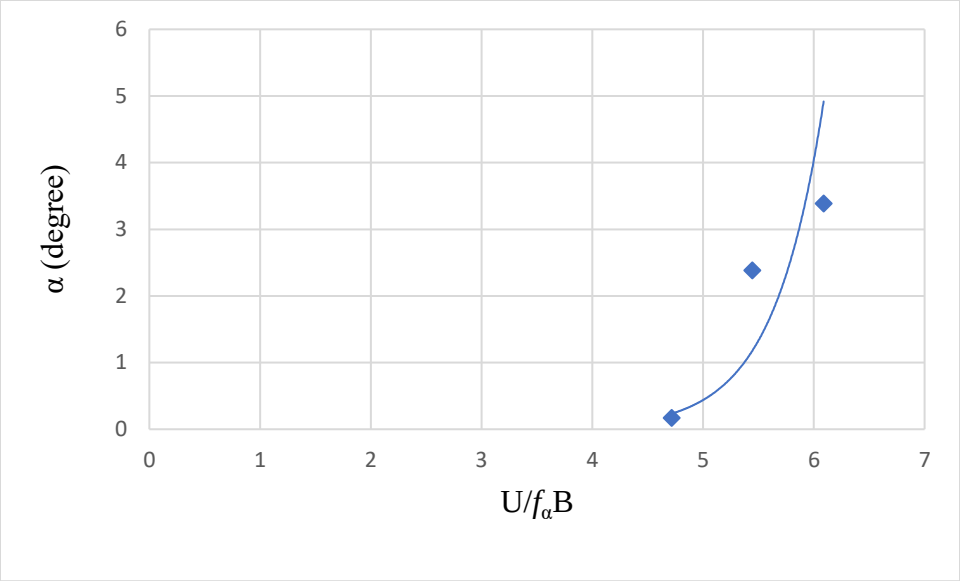

Figure 4.10 Torsional RMS amplitude vs reduced velocity for 'π' section

For the vertical-torsional DOF tests, the structure vibrates in a coupled mode at a given wind speed, where the first mode at a slightly modified frequency associated with the vertical DOF at zero wind speed, and the second mode at a slightly modified frequency associated with the torsional DOF at zero wind speed, contribute to the dynamic motion. As the wind speed increases the two frequencies become closer to each other and at flutter boundary both the frequencies will be almost equal to f_F (or Flutter Frequency) and the corresponding speed is determined to be the flutter speed in the vertical-torsional DOF. In the vertical-torsional experiments performed in this study using rectangular sections and hybrid section, the vertical amplitude of vibration dominates the torsional amplitude of vibration in a coupled vertical-torsional motion. A Fast Fourier Transform (FFT) was conducted to convert the time domain acceleration signal into frequency domain signal to understand this phenomenon. Figure 4.11 and 4.12 shows the frequency domain plot converted from the time history of the acceleration signal at wind speeds of 5 m/s and 5.4 m/s that are below the flutter speed for the rectangular section

(B/D=1.5, vertical-torsional DOF). As the wind speed increases from 5 m/s to 5.4 m/s, the amplitude of the vertical frequency increases from 38 V to 40 V but the amplitude of the torsional frequency slightly reduces or remains the same around 10 V. As the wind speed increases and approaches the flutter speed, the amplitude of the vertical frequency increases further, but the amplitude of torsional frequency decreases or remains the same, therefore, the ratio of amplitude of vertical to torsional frequency is much higher. Thus, at flutter boundary it is expected that the torsional frequency will have much lower amplitude which implies that the participation of the torsional mode at flutter will be very low or almost negligible leading to a predominantly vertical flutter mode. Thus, for practical purposes, to predict the flutter speed in the vertical-torsional DOF, the normalized vertical RMS amplitude is plotted against the reduced velocity and the point where the normalized vertical RMS amplitude reaches 0.5 is assumed to be the flutter speed in the vertical-torsional DOF like the vertical-DOF only case.

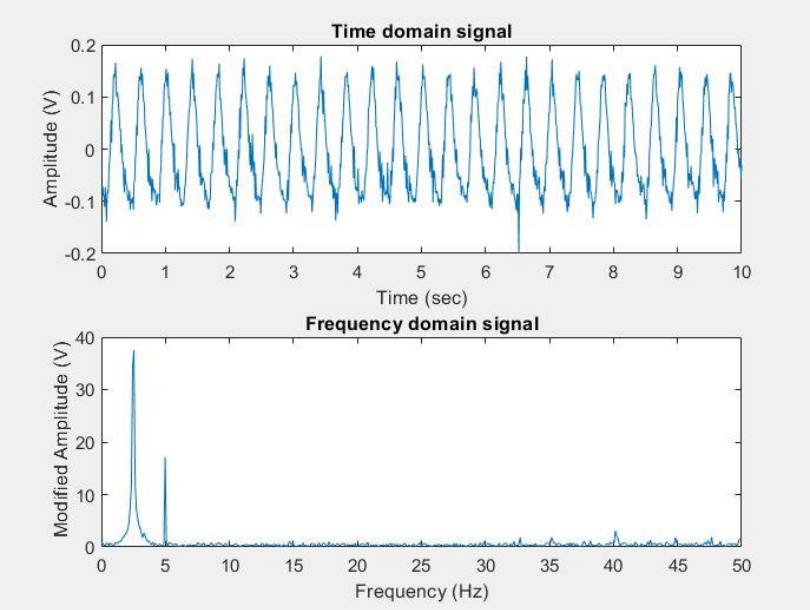

Figure 4.11 FFT of recorded acceleration time history at 5 m/s

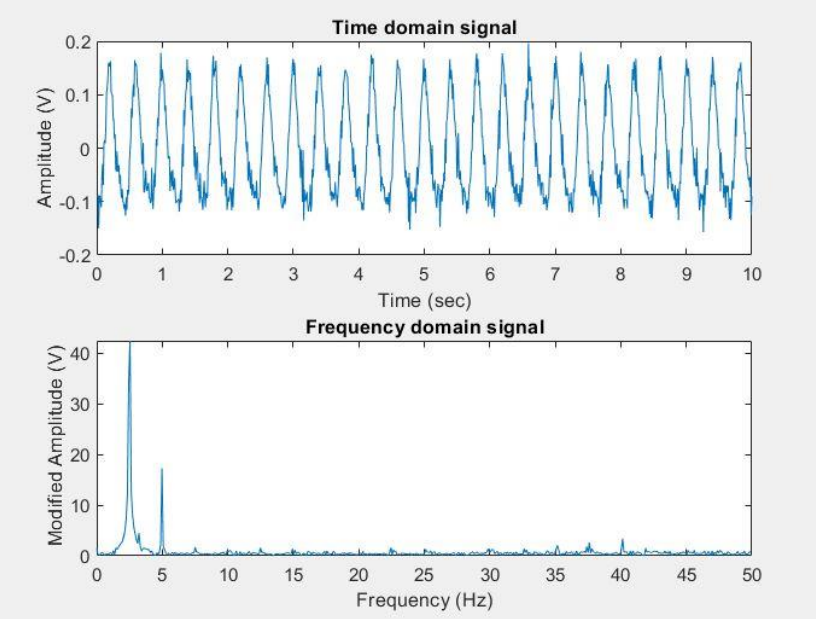

Figure 4.12 FFT of recorded acceleration time history at 5.4 m/s

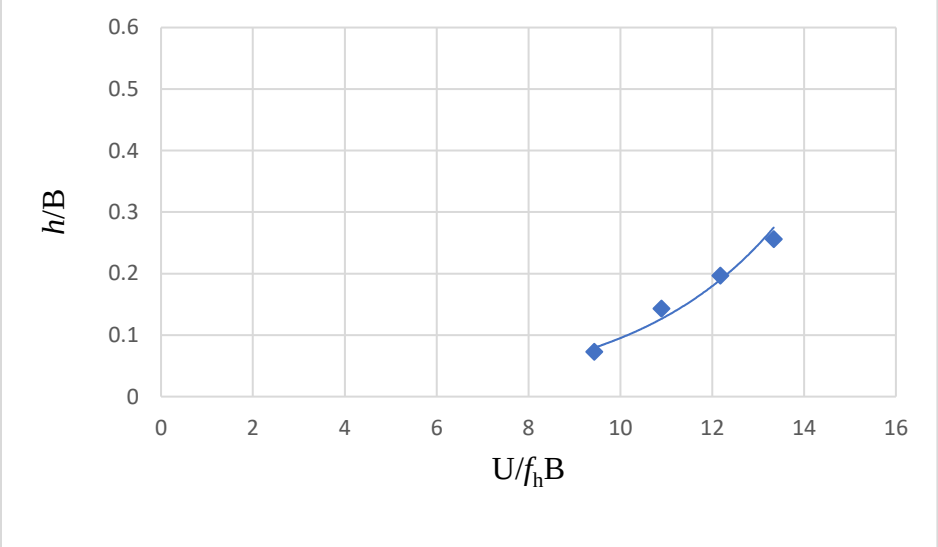

Figure 4.13 Normalized Vertical RMS Amplitude vs reduced velocity for Rectangular section, Vertical-Torsional DOF (B/D=1.5)

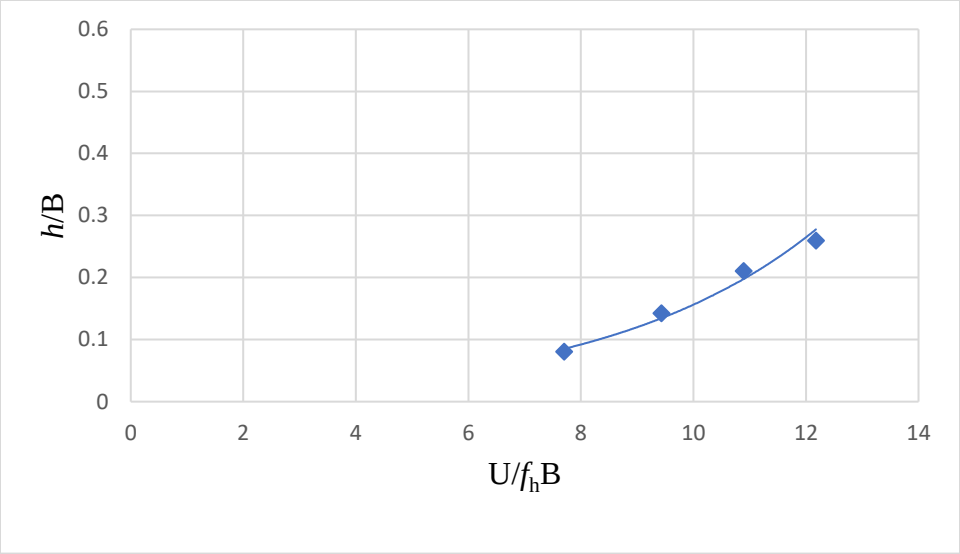

Figure 4.14 Normalized Vertical RMS Amplitude vs reduced velocity for Rectangular section, Vertical-Torsional DOF (B/D=1)

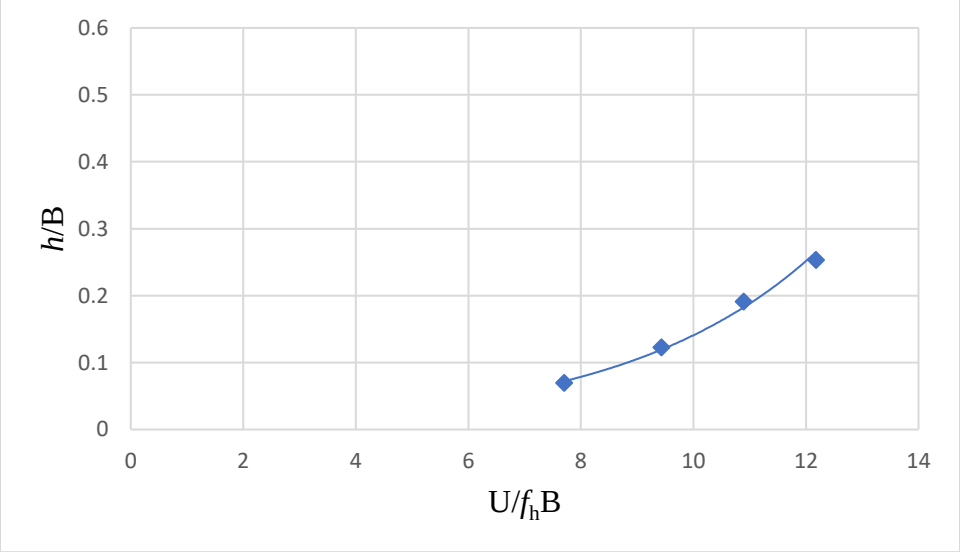

Figure 4.15 Normalized Vertical RMS Amplitude vs reduced velocity for Hybrid section in Vertical-Torsional DOF

Table 4.1 Comparison of flutter speed for different sections

Section Model	DOF	Flutter Speed (m/s)
Rectangular (B/D=1.5)	Vertical	5.03
Rectangular (B/D=1)	Vertical	4.99
Rectangular (B/D=1.5)	Torsional	6.61
Rectangular (B/D=1)	Torsional	6.48
'H' section (Configuration 1)	Torsional	4.49
'H' section (Configuration 2)	Torsional	4.56
'π' section	Torsional	4.72
Rectangular (B/D=1.5)	Vertical-Torsional	5.70
Rectangular (B/D=1)	Vertical-Torsional	5.40
Hybrid	Vertical-Torsional	5.38

Table 4.1 compares flutter speed in different DOF (vertical, torsional, and vertical-torsional) for different section models.

4.2 Effect of Frequency Ratio on Flutter Speed

In the 2-DOF suspension system used, the vertical frequency remains constant, but the torsional frequency can be varied. This can be achieved by moving the springs closer to each other or moving it farther away from each other. Frequency ratio can be defined as the ratio of the vertical frequency of the suspension system to the torsional frequency of the suspension system (σ).

$$\sigma = \frac{f_h}{f_\alpha}$$

It is critical to determine the best frequency ratio of the suspension system that will make the model to vibrate in both the directions at the lowest possible wind speed. The flutter boundary is very sensitive to the frequency ratio (σ). There are certain frequency ratios at which the flutter speed becomes very small depending on the values of other parameters. For this purpose, experiments were carried out by changing the torsional frequency of the suspension system, keeping all other system parameters constant. In the first case, the springs were attached at the top and bottom sides of the horizontal 'C' section which holds the section model and the distance between the springs was fixed at 11 inches when the corresponding frequency ratio is 0.25. Then the springs were moved closer to each other to obtain a frequency ratio of 0.5, the distance between the springs was 1 inch. The rectangular section models exhibited only vertical motion with the suspension system frequency ratio of 0.25. The rectangular section models exhibited vertical-torsional motion when the suspension system frequency ratio was 0.5. Figures 4.16 and 4.17 shows the effect of frequency ratio on flutter speed for the rectangular sections. It is clear that both the rectangular sections follow the same trend. From the plots it can be said that the flutter speed increases with increasing frequency ratio. For the vertical DOF only cases, $\sigma = 0.25$ can be used and for the vertical-torsional DOF cases, $\sigma = 0.5$ can be used since the rectangular sections exhibited coupled vertical-torsional motion only at a frequency ratio of 0.5. Thus, frequency ratio can be used as the system parameter for making a decision to optimize the functioning of the FIV wind energy harvester. Since the flutter speed is higher for a vertical-torsional case than the vertical-only case, the decision to select a larger frequency ratio and hence a vertical-torsional case has to be based on a higher wind energy capture.

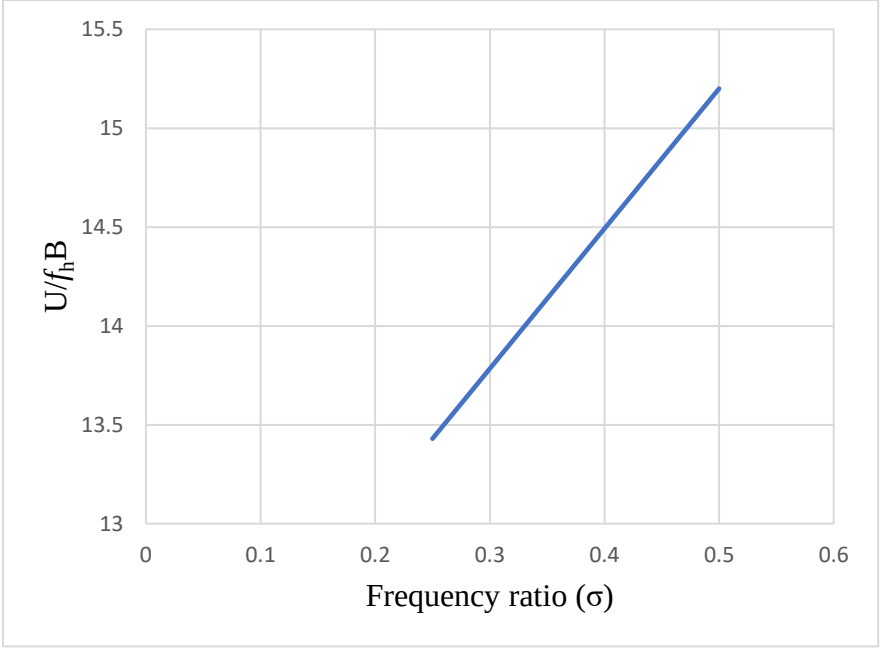

Figure 4.16 Frequency ratio vs flutter speed for Rectangular section (B/D=1.5)

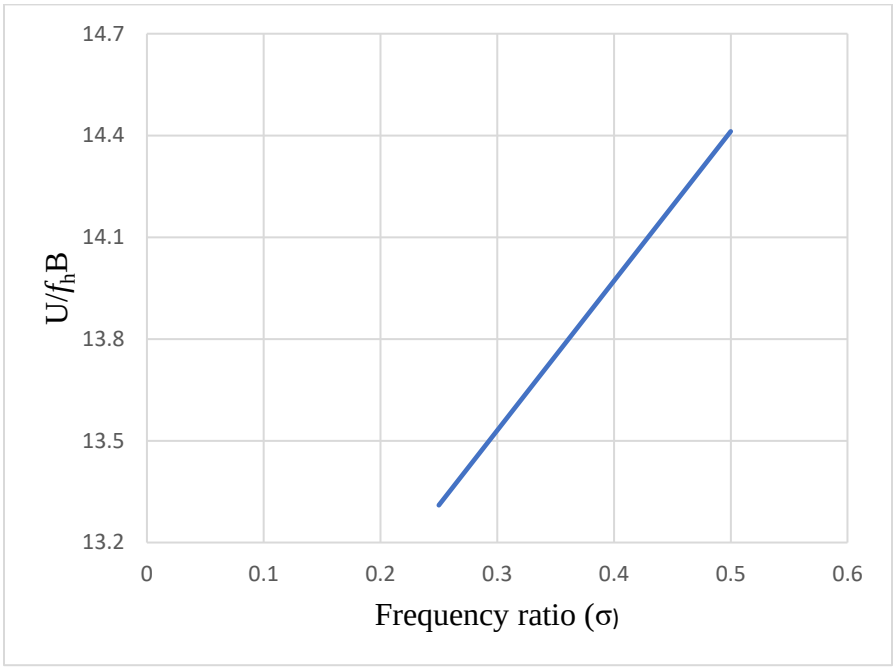

Figure 4.17 Frequency ratio vs flutter speed for Rectangular section (B/D=1)

Table 4.2 Type of motion exhibited by different section models for different Frequency ratio

SECTION MODEL	FREQUENCY RATIO (σ)	TYPE OF MOTION
Rectangular Section B/D=1.5	0.25	Vertical
	0.5	Torsional
	0.5	Vertical-Torsional
Rectangular Section B/D=1	0.25	Vertical
	0.5	Torsional
	0.5	Vertical-Torsional
'H' shaped section (Configuration 1)	0.25	Not tested
	0.5	Torsional
'H' shaped section (Configuration 2)	0.25	Not tested
	0.5	Torsional
'π' shaped section	0.25	Not tested
	0.5	Torsional
Hybrid section	0.25	Not tested
	0.5	Vertical-Torsional

Note: Torsional-DOF only cases were obtained with the vertical DOF restrained.

4.3 Effect of Mass Ratio on Flutter Speed

Mass of the FIV wind energy harvester is another important system parameter to be determined. The system should not be too heavy to achieve low flutter speed, but at the same time it should be heavy enough to vibrate at a given wind speed with a considerable amplitude response to generate reasonable amount of wind energy which is proportional to the mass.

Mass ratio (μ) in the vertical direction is defined as,

$$\mu = \frac{m}{\pi \rho B^2}$$

Mass ratio (μ) in the torsional direction is defined as,

$$\mu = \frac{I}{\pi \rho B^4}$$

where m is the mass per unit length of the section model, I is the moment of inertia per unit length of the section model, ρ is the density of air, and B is the width of the section model. To vary the mass of the system in the vertical direction, additional weights (0.25 kg, 0.50 kg and 1 kg) were added on the upper surface of the section model (M=5 kg) along the model mid-plane. In the torsional direction, moment of inertia was varied. Two identical weights were placed on the upper surface of the model, one at the windward edge and one at the leeward edge. The distance between the weights was measured to be 8 cm. For each case, acceleration was recorded for a range of wind speed to estimate the flutter speed. Figures 4.18 and 4.19 show the effect of Mass ratio in the vertical DOF on flutter speed for the rectangular section models and Figure 4.20 shows the effect of Mass ratio in the vertical-torsional DOF on flutter speed for the hybrid section. Both the rectangular sections follow the same pattern in the vertical DOF. It is clear that lower mass ratio will produce a lower flutter speed.

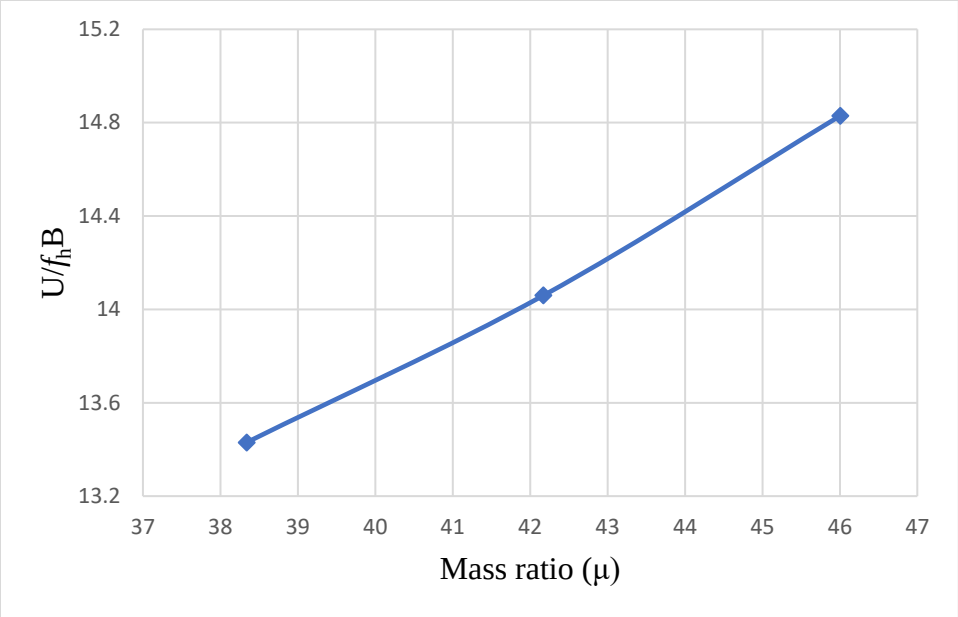

Figure 4.18 Mass ratio vs flutter speed for Rectangular section (B/D=1.5) in vertical DOF

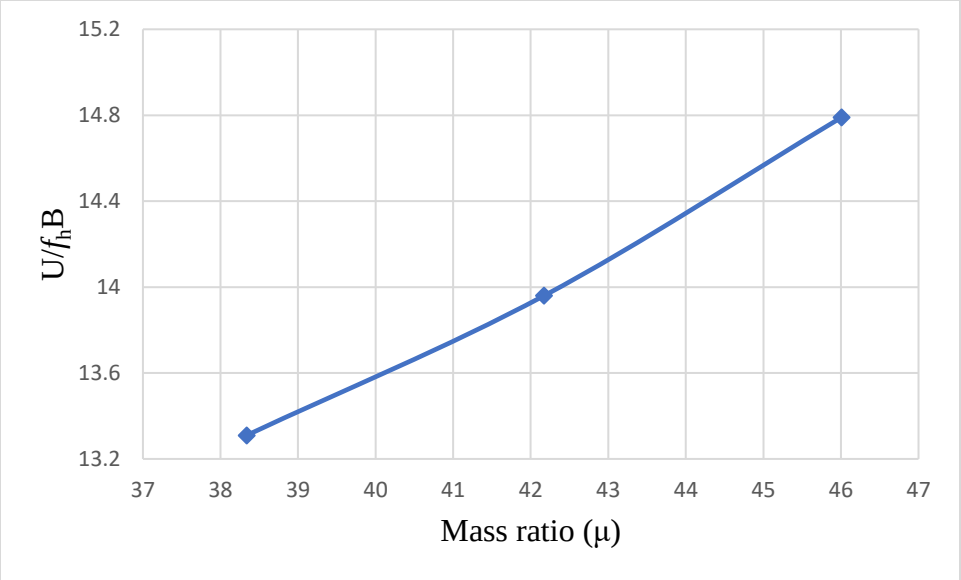

Figure 4.19 Mass ratio vs flutter speed for Rectangular section (B/D=1) in vertical DOF

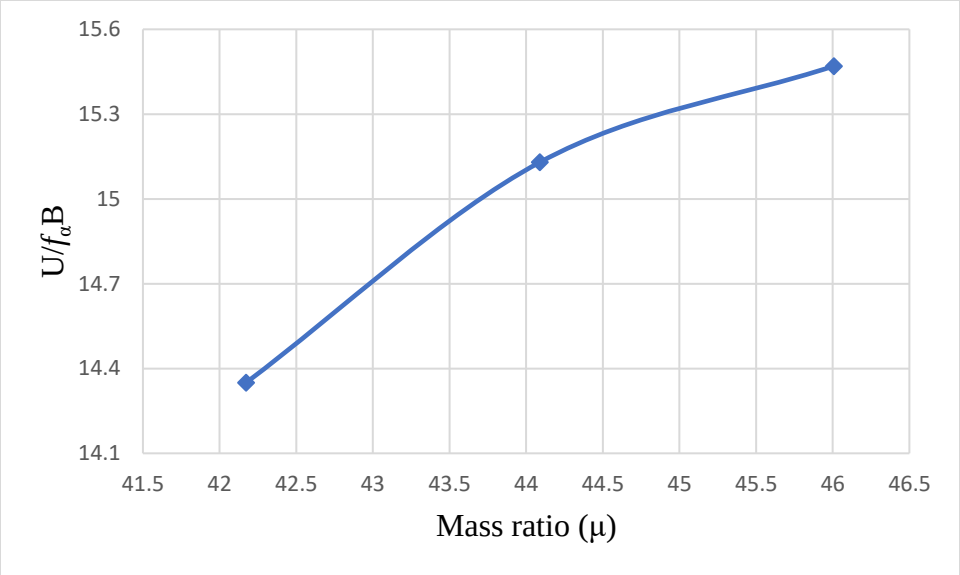

Figure 4.20 Mass ratio vs flutter speed for Hybrid section (vertical-torsional DOF)

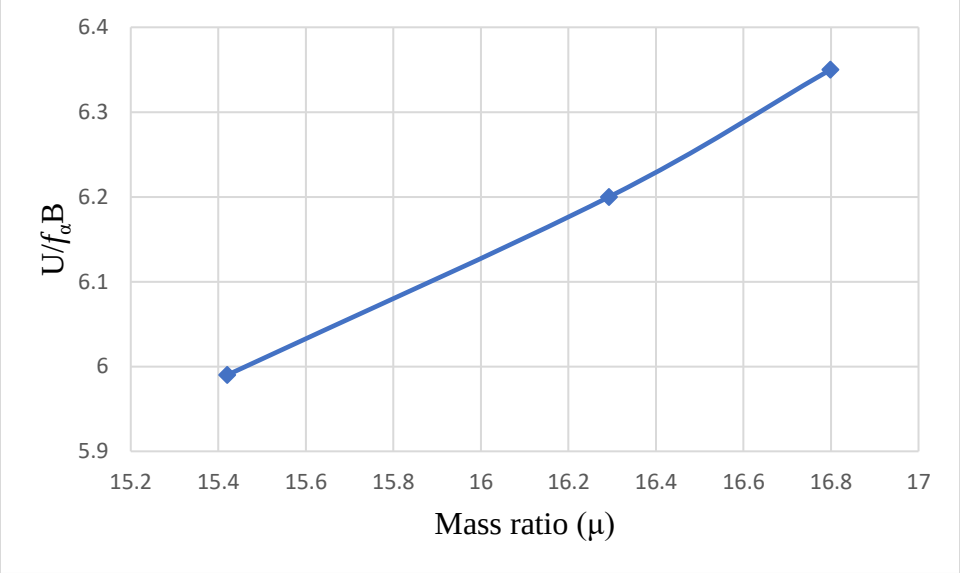

Figure 4.21 Mass ratio vs flutter speed for 'H' section (Configuration 1) in torsional DOF

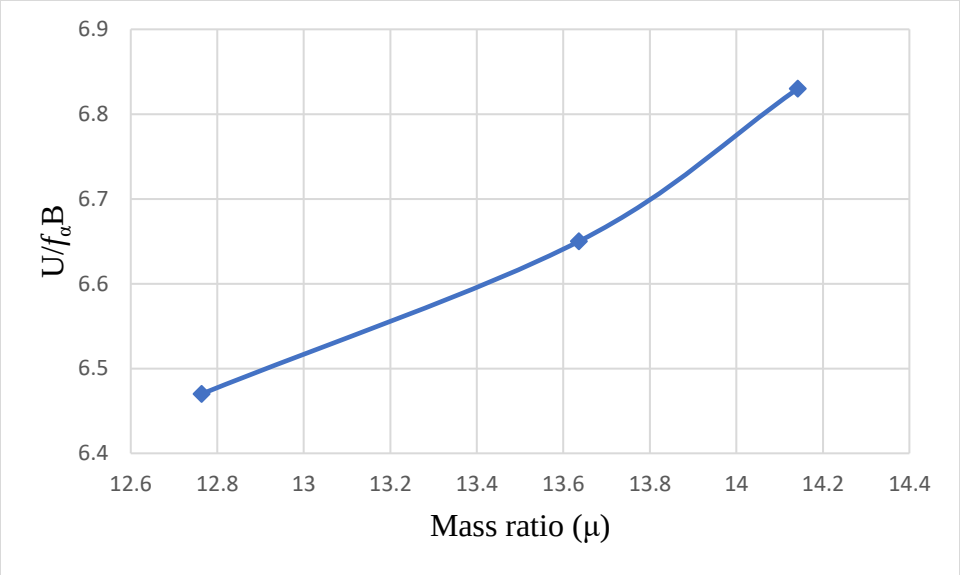

Figure 4.22 Mass ratio vs flutter speed for 'H' section (Configuration 2) in torsional DOF

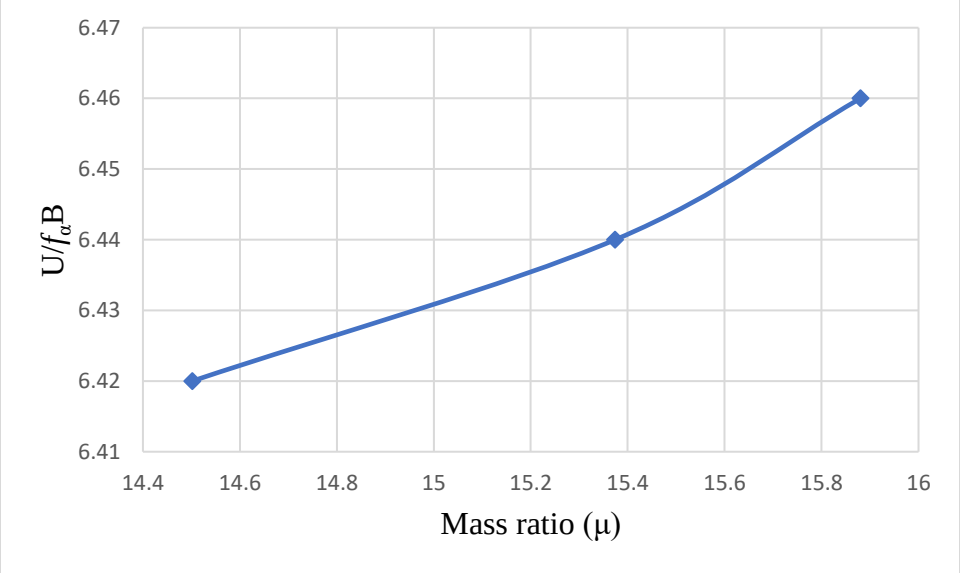

Figure 4.23 Mass ratio vs flutter speed for 'π' section in torsional DOF

Figures 4.21, 4.22 and 4.23 show the effects of mass ratio in the torsional DOF on flutter speed for the 'H' sections and 'π' section. It is clear that, both 'H' sections and 'π' section follow the same trend. From the plots we can say that the flutter speed increases proportionally with the Mass ratio. But as the mass increases, the amplitude of vibration of the section models

decreases which reduces the power generation. Thus, all these parameters are inter-related and needs to be determined carefully for enhanced power generation.

4.4 Effect of Offset Distance on Flutter Speed

The model is suspended at several offset distance to determine the effect of offset distance on the flutter speed. The model is moved by 1 inch, both forward and backward in the along wind direction. Zero-offset case (Figure 4.24) is the standard case, where the model is placed at mid-point between both the springs. The center of mass (C_M) and center of stiffness (C_S) acts at the same point in the zero-offset case. In the backward-offset case (Figure 4.25), the model is moved backward by 1 inch and the springs remain fixed in the same position. In this case, the center of stiffness (C_S) is ahead of the center of mass (C_M). In the forward-offset case (Figure 4.26), the model is moved forward by 1 inch while the springs remain fixed in the same position. In this case, the center of stiffness (C_S) is behind the center of mass (C_M). Thus, the backward-offset, where C_M is behind C_S along the wind direction, is represented by a negative offset distance, and the forward-offset, where C_M is ahead of C_S along the wind direction, is represented by a positive offset distance.

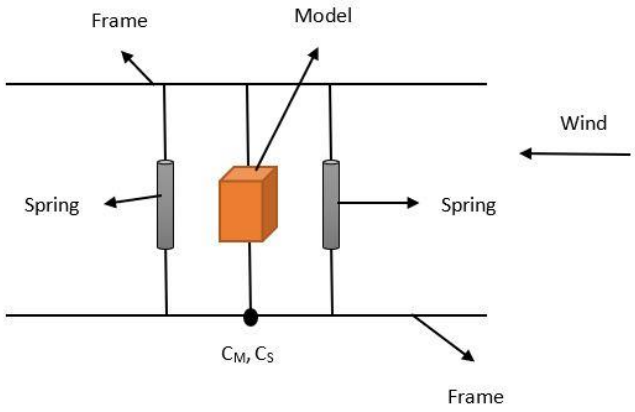

Figure 4.24 Zero-Offset

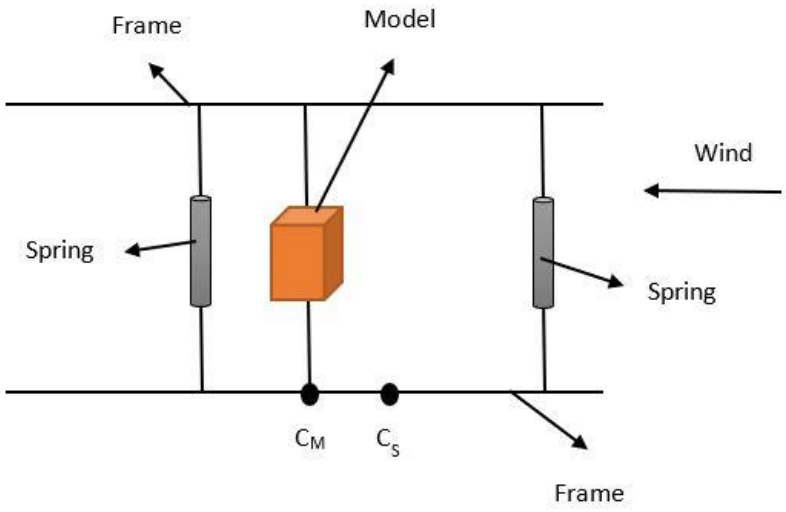

Figure 4.25 Backward-Offset

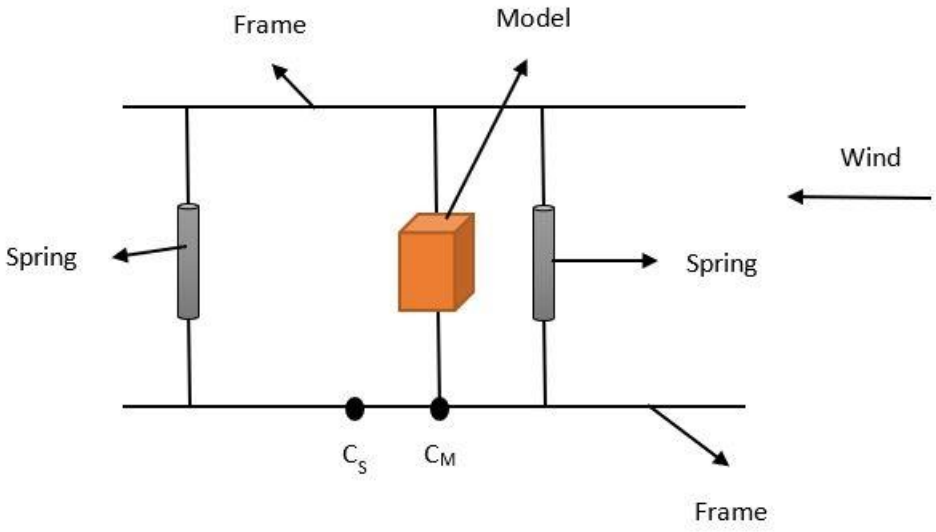

Figure 4.26 Forward-Offset

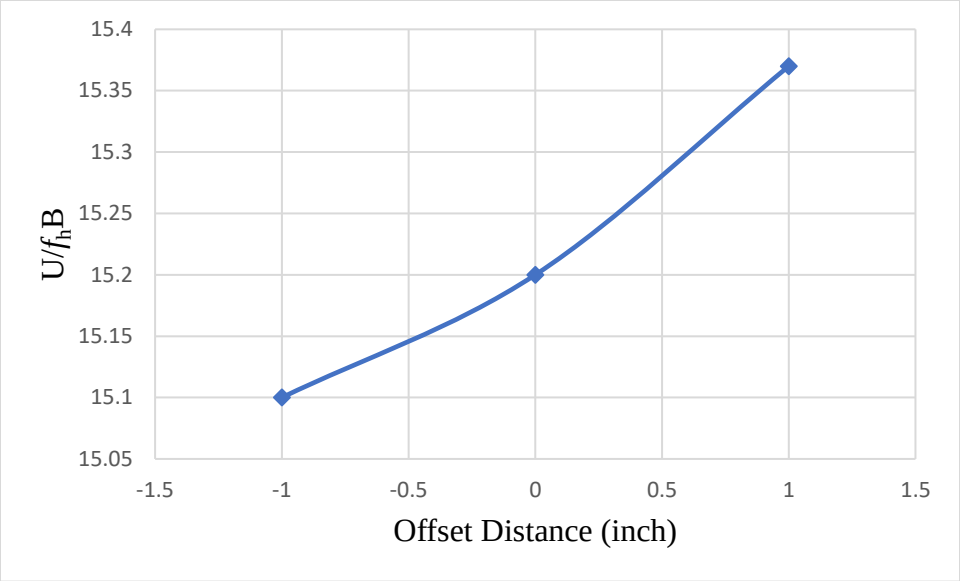

Figure 4.27 Offset Distance vs flutter speed for Rectangular section (B/D=1.5)

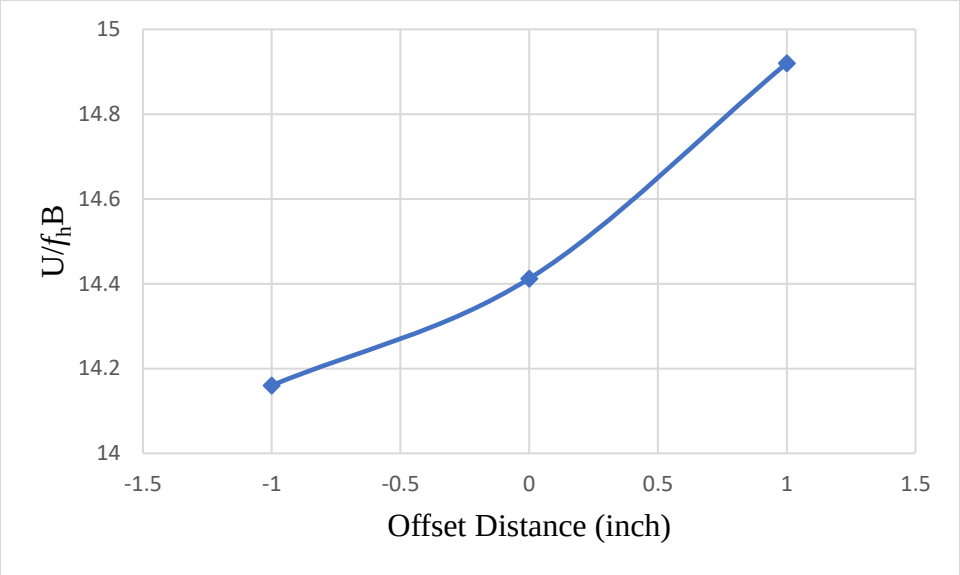

Figure 4.28 Offset Distance vs flutter speed for Rectangular section (B/D=1)

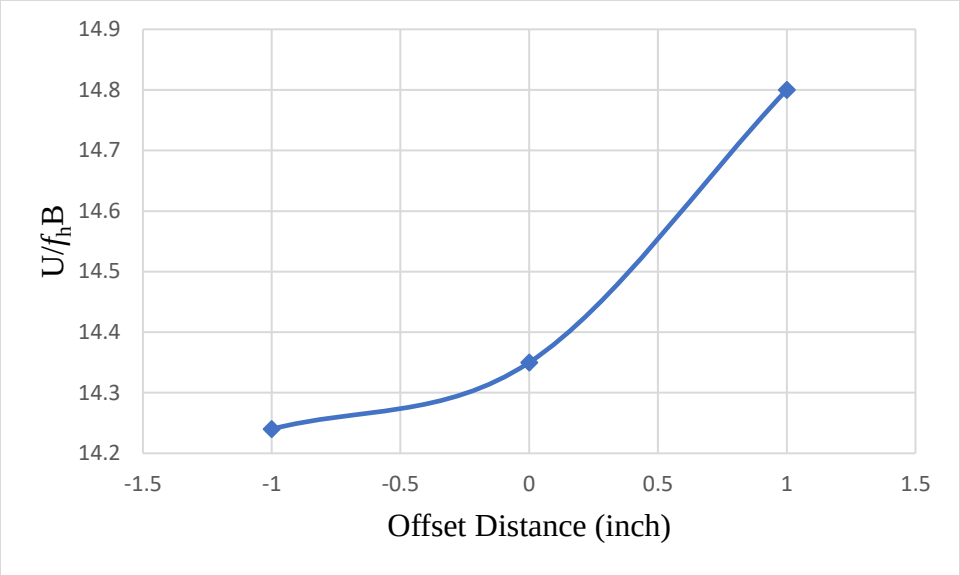

Figure 4.29 Offset Distance vs flutter speed for Hybrid section

Figures 4.27, 4.28 and 4.29 show the effect of offset distance on flutter speed for the rectangular sections and the hybrid section. The trend is same among all the section models. The flutter speed increases proportionally with the offset distance. The backward-offset case gives the lowest flutter speed, and the forward-offset case gives the largest flutter speed. In the forward offset case, since the center of mass (C_M) is ahead of the center of stiffness (C_S), the suspended section model is slightly tilted up. Similarly, in the backward-offset case the suspended section model is slightly tilted down because the center of mass (C_M) is behind the center of stiffness (C_S). This results in a slight angle of attack which also known to modify the flutter speed. Figures 4.30 and 4.31 show the variation of normalized vertical RMS displacement with offset distance for the rectangular section (B/D=1) and the hybrid section. Both the sections exhibit the same trend, the backward-offset gives the largest RMS amplitude of vertical displacement among all the three offset cases, more than the zero-offset and forward-offset cases. The forward-offset case gives the smallest RMS amplitude of vertical displacement, almost half of

the backward-offset case. Thus, to improve the performance of the FIV wind energy harvester, a small backward offset can be given to the vibrating section which reduces the flutter speed and increase the amplitude of vibration leading to its better performance.

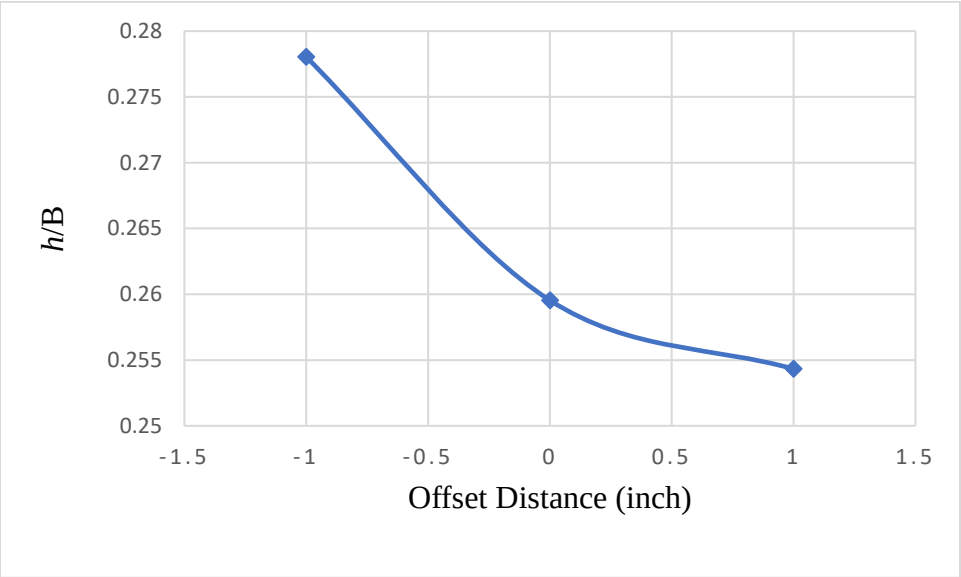

Figure 4.30 Effect of Offset Distance on Vertical Displacement for Rectangular section (B/D=1)

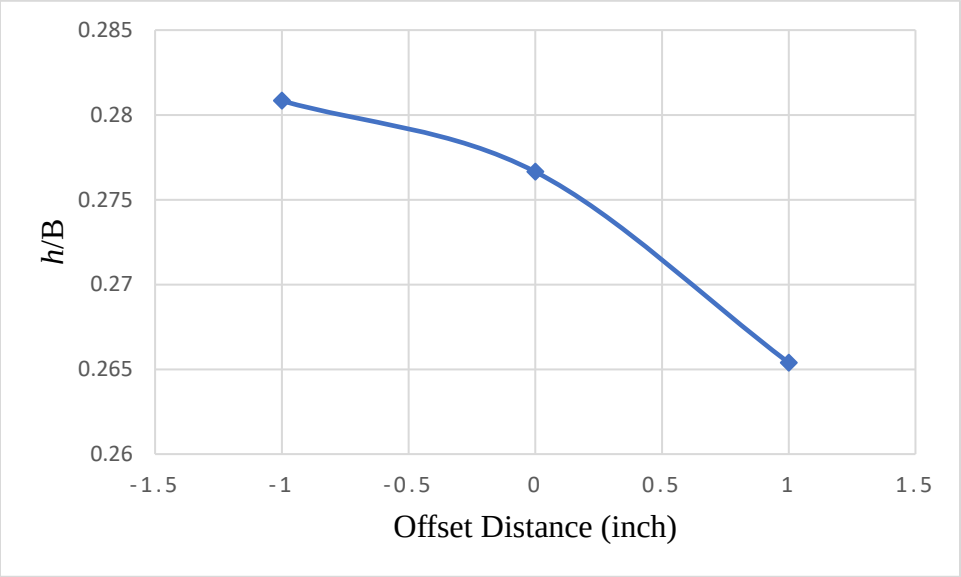

Figure 4.31 Effect of Offset Distance on Vertical Displacement for Hybrid section

4.5 Comparative Performance Study of Different Cross-Sections

The FIV wind energy harvester as conceived in this study can use any of the sections studied here but preferably a hybrid section like one tested for the following reason. At lower wind speeds around 3 m/s, the rectangular section will flutter in the vertical DOF, but it will not flutter in the torsional DOF. Similarly, the 'H' section will flutter in the torsional direction, but it will not flutter in the vertical DOF at lower wind speeds around 4 m/s. When the two sections are combined to form a hybrid section, at a given wind speed, one section is prone to vibration in the vertical DOF, and the other section is prone to vibration in the torsional DOF, leading to a vertical-torsional motion. The vertical-torsional flutter at relatively low flutter speed is advantageous because it is expected to generate more power than a single degree of freedom FIV wind energy harvester.

Section models of different sectional shapes studied here were selected for comparison of potential power generation based on the amplitude of their response at or near flutter and magnitude of flutter speed. Rectangular sections with B/D=1.5 and B/D=1 were selected, analyzed and compared for better amplitude response in the vertical DOF and low flutter speed. 'H' sections (Configuration 1 and 2) and 'π' section were selected, analyzed and compared for better amplitude response in the torsional DOF and low flutter speed.

The best performing section in the vertical DOF is then combined with the best performing section in the torsional DOF to form a Hybrid section. The Hybrid section is analyzed and compared with the rectangular section and 'H' section in terms of power generation and flutter speed.

4.5.1 Rectangular Sections, B/D=1.5 vs B/D=1

Rectangular sections exhibited only vertical motion when the frequency ratio of the system was set to be 0.25. When the frequency ratio was changed to 0.5, they exhibited vertical-torsional motion. The vertical RMS amplitudes from a vertical DOF test is used to compare the rectangular sections, and therefore, the system frequency was set to 0.25. Acceleration of the vibrating model was recorded at multiple wind speeds to determine the flutter speed. For comparison, the normalized vertical RMS displacement is plotted against the Scruton number. The Scruton number (S_C), also known as mass-damping parameter, is an important parameter when considering flow induced vibrations. It is defined as,

$$S_C = \frac{m\,\xi}{\rho\, D_C^2}$$

where, m is the mass per unit length of the section model, ξ is the vertical damping in the system, ρ is the density of air and $D_C = \sqrt{B\,D}$, where B is the width of the section model and D is the depth or height of the section model. Experiments were performed by changing the mass of the system, by adding additional weights on the section model. The weights were secured with a painter's tape to avoid slipping while the model is vibrating. The damping of the system also changes when the mass of the system is changed, thus, the damping is estimated every time before recording the acceleration. Figures 4.32 and 4.33 show the variation of vertical amplitude against Scruton number for the rectangular sections. From these plots, it can be seen that the vertical amplitude decreases with increasing Scruton Number. After a certain point the vertical amplitude remains constant and does not decrease further with increasing Scruton number. This can be seen in Figure 4.33 for the rectangular section (B/D=1), where at Scruton number of 0.43, the vertical RMS amplitude approaches an asymptotic constant of 0.28. As per equation (2.42), power generation can be increased by increasing the Scruton number, but since increasing the

Scruton number reduces the amplitude of vibration it decreases the power generation. The Scruton number is a very important factor in designing FSI-based energy harvester because if the Scruton number is fixed then the amplitude of vibration gets fixed, and then we the other system parameters like the total mass of the system, and dimensions like width and height and frequency of the vibrating section model can be changed to maximize the power (Equation (2.42)).

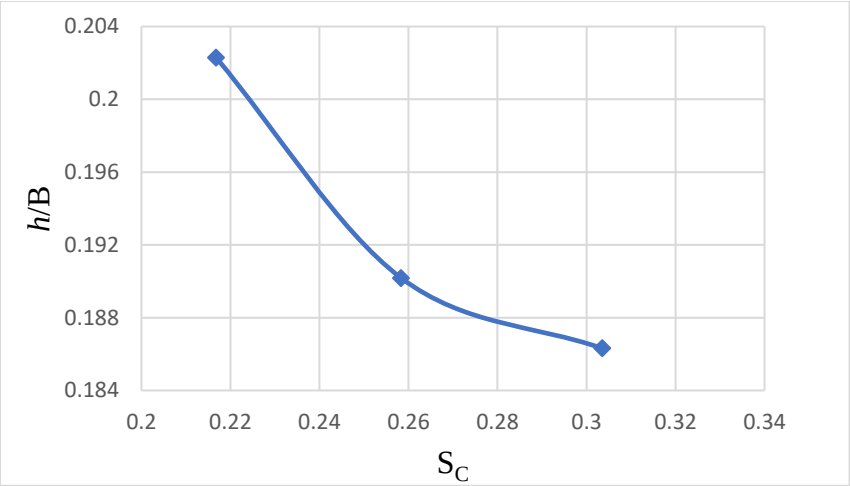

Figure 4.32 Normalized Vertical RMS Amplitude vs Scruton number for Rectangular section (B/D=1.5)

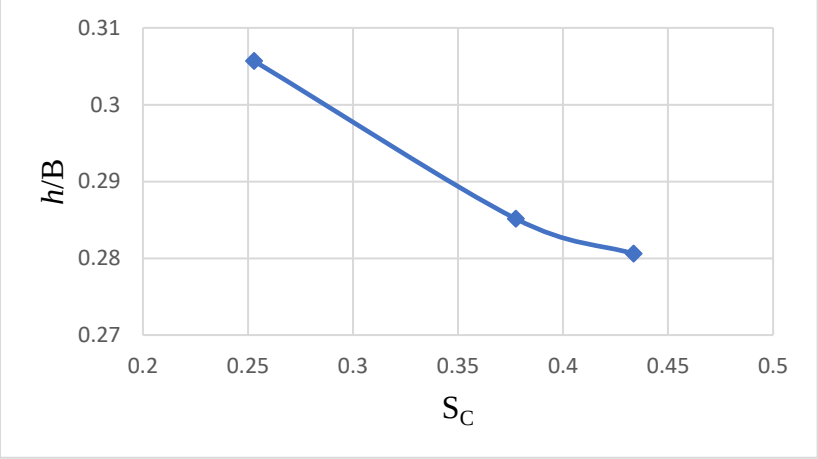

Figure 4.33 Normalized Vertical RMS Amplitude vs Scruton number for Rectangular section (B/D=1)

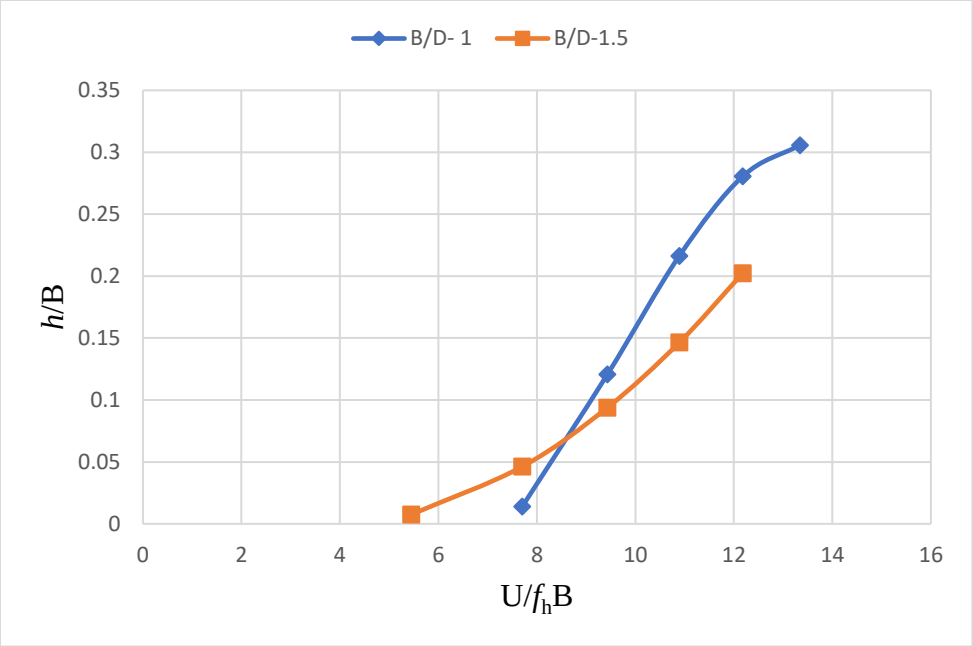

Figure 4.34 Comparison of Normalized Vertical RMS Amplitude between Rectangular sections

Figure 4.34 shows the comparison of vertical amplitude among the two rectangular sections. From the plot, it is clear that after a reduced velocity of 8.3, B/D=1 rectangular section has higher vertical amplitude than the B/D=1.5 rectangular section. The flutter speed in the vertical DOF for the rectangular section (B/D=1.5) is estimated to be 5.03 m/s (RV=13.4) and for the rectangular section (B/D=1) it is 4.99 m/s (RV=13.3). Therefore, the rectangular section (B/D=1) has almost same flutter speed but considerably higher vertical amplitude than the rectangular section (B/D=1.5) at flutter which is beyond reduced velocity of 8.3. Thus, the rectangular section (B/D=1) has better performance in terms of power generation than the rectangular section (B/D=1.5) in the vertical DOF and is therefore selected as one of the cross-sections for the hybrid section model.

4.5.2 ‘H’ Sections, ‘H’ Section vs ‘π’ Section

Among the ‘H’ sections, comparison was made by recording the torsional displacement as the model vibrates. The frequency ratio of the system was set to be 0.5, as the torsional frequency is relatively smaller. Only at higher wind speeds the ‘H’ sections vibrate in the vertical DOF with a very small amplitude. Thus, the vertical motion was restricted by attaching a string to the horizontal ‘C’ section that holds the model. One end of the string is connected to the upper frame, the other end of the string goes through the ‘C’ channel plate and is connected to the lower frame. Acceleration in the torsional DOF was measured for multiple wind speeds to determine the flutter speed. The torsional RMS displacement in degrees is plotted against Scruton Number for comparison. The Scruton Number in the torsional DOF is defined as,

$$S_C = \frac{I\,\xi}{\rho\, D_C^4}$$

where, I is the moment of inertia per unit length of the section model, ξ is the torsional damping in the system, ρ is the density of air and $D_C = \sqrt{B\,D}$, where B is the width of the section model and D is the height of the section model. In this case, experiments were performed for different moment of inertia of the ‘H’ section models. The moment of inertia is increased by placing two identical weights on the model, one near the windward edge and other near the leeward edge. The distance between the weights was measured to be 8 cm. The weights were secured with a painter’s tape to avoid slipping while the model is vibrating. The damping of the system is also estimated every time, after placing the weights before recording the acceleration. Figures 4.35, 4.36 and 4.37 show the variation of torsional RMS amplitude against Scruton number for the ‘H’ sections and ‘π’ section. Both the ‘H’ sections and the ‘π’ section follow the same trend. The torsional RMS amplitude decreases with increasing Scruton number. After a certain Scruton Number, the torsional amplitude remains almost constant and does not decrease further for

increasing Scruton Number. Thus, by fixing the ideal Scruton number for maximum torsional amplitude, other system parameters like the total mass moment of inertia, length, dimensions like width and height and frequency of the section model can be modified to improve the efficiency of the FIV wind energy harvester.

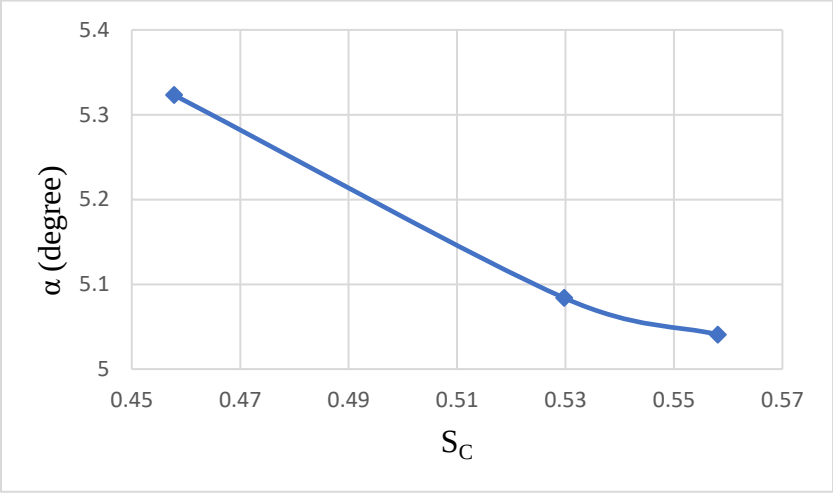

Figure 4.35 Torsional RMS Amplitude vs Scruton number 'H' section (Configuration 1)

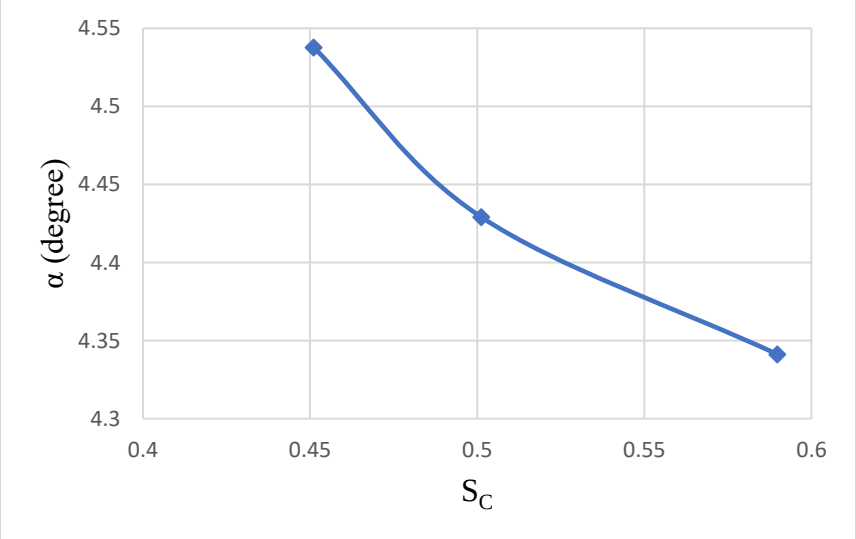

Figure 4.36 Torsional RMS Amplitude vs Scruton number 'H' section (Configuration 2)

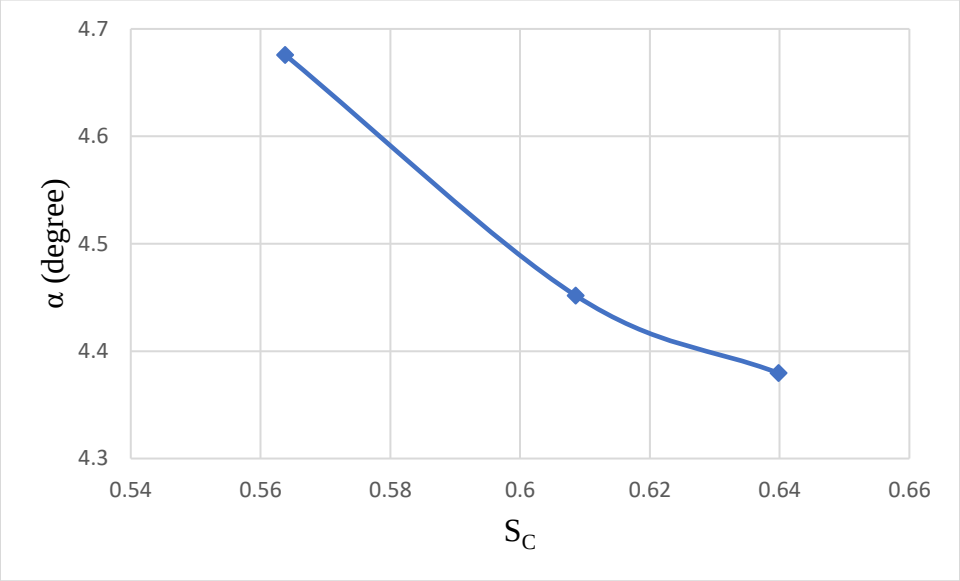

Figure 4.37 Torsional RMS Amplitude vs Scruton number 'π' section

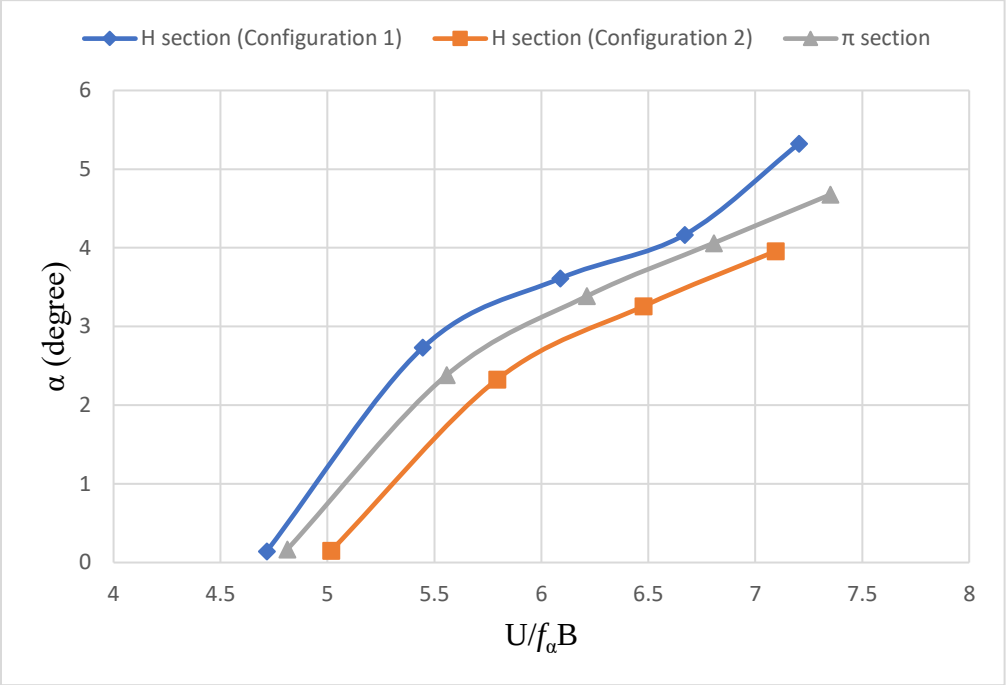

Figure 4.38 Comparison of Torsional RMS Amplitude between 'H' sections and 'π' section

Figure 4.38 shows the comparison of torsional RMS amplitude among the two ‘H’ sections and the ‘π’ section. ‘H’ section (Configuration 1) has higher torsional amplitude for a given wind speed than the ‘H’ section (Configuration 2) and the ‘π’ section. The flutter speed in the torsional DOF for ‘H’ section (Configuration 1) is 4.49 m/s, for ‘H’ section (Configuration 2) it is 4.56 m/s and for the ‘π’ section it is 4.72 m/s. The ‘H’ section (Configuration 1) has higher torsional displacement and lowest flutter speed in the torsional-DOF than the ‘H’ section (Configuration 2) and the ‘π’ section. Thus, the ‘H’ section (Configuration 1) has a better overall performance in the torsional DOF and is therefore selected as the second cross-section for the Hybrid section model.

4.5.3 Hybrid Section: Rectangular and ‘H’ Sections

Hybrid section consists of one half of the rectangular section (B/D=1) and one half of ‘H’ section (Configuration 1). The rectangular section (B/D=1) has the highest vertical displacement and lowest flutter speed from the vertical-DOF tests, and the ‘H’ section (Configuration 1) has the highest torsional displacement and lowest flutter speed from the torsional-DOF tests. Both the rectangular section and the hybrid section exhibit coupled vertical-torsional motion when the system frequency ratio is set to 0.5. The ‘H’ sections and the ‘π’ does not exhibit vertical-torsional motion at lower wind speeds. Thus, vertical-torsional motion tests were performed for the hybrid section and compared with the rectangular section (B/D=1) to determine its performance with respect to the power generated.

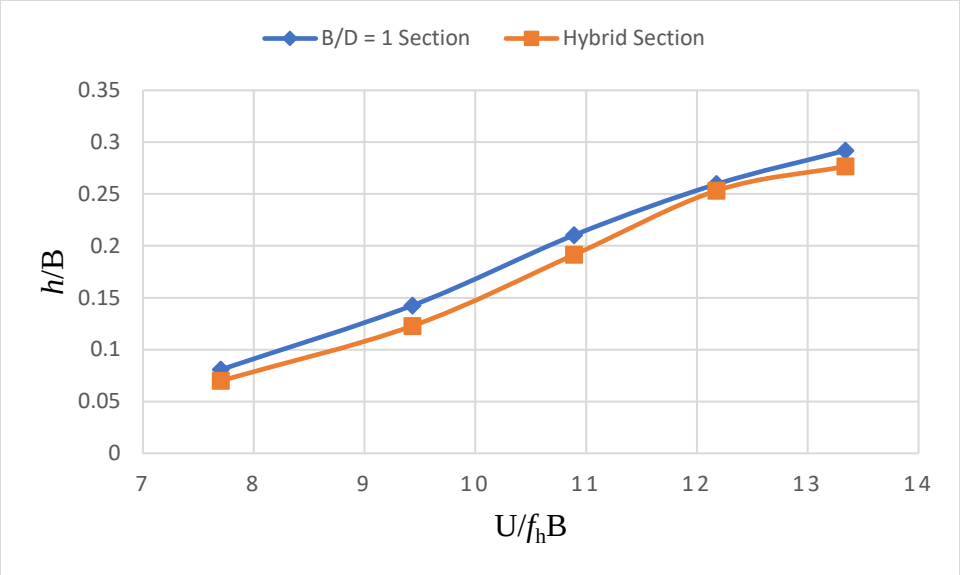

Figure 4.39 Comparison of Normalized Vertical RMS Amplitude between Rectangular (B/D=1) and Hybrid section

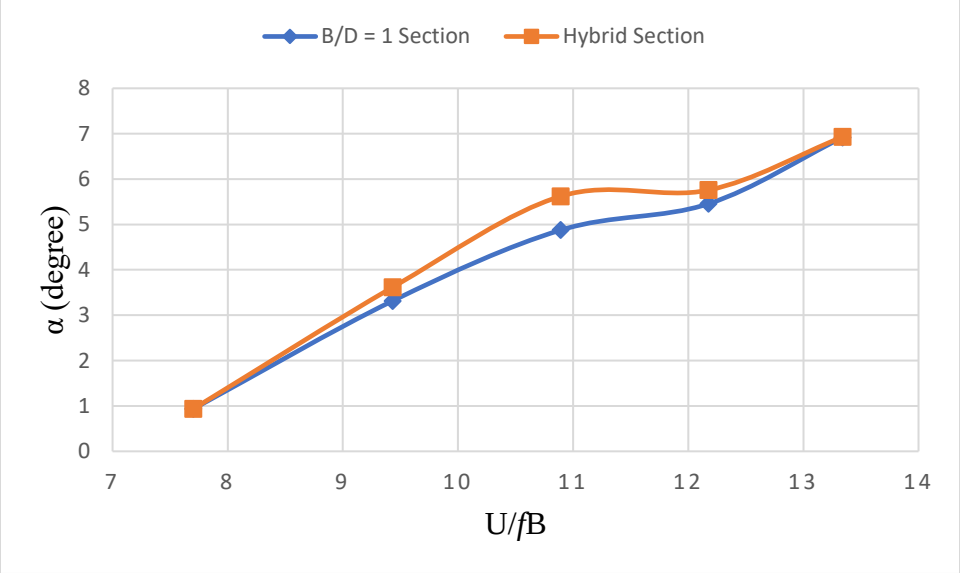

Figure 4.40 Comparison of Torsional RMS Amplitude between Rectangular (B/D=1) and Hybrid section

During the torsional-DOF tests, the rectangular section (B/D=1) started to flutter around 4.56 m/s with a very low amplitude (0.1 degree). It had a maximum torsional amplitude of 4.8 degrees at a wind speed of 6.46 m/s. But during the vertical-torsional test, it exhibited vertical-torsional motion much earlier around 4.08 m/s. Also, the torsional amplitude was much higher (7 degrees) than the torsional-DOF tests. This can be because of the influence of the coupled vertical-torsional motion. The vertical amplitude from the vertical-torsional test almost remains the same when compared to vertical amplitude from the vertical-DOF test. Thus, a 2-DOF energy harvester extracts more wind energy due to high amplitude of displacements due to the coupled motion than a 1-DOF energy harvester.

Similarly, during the torsional-DOF tests, the ‘H’ section (Configuration 1) started to flutter around 3.54 m/s with a very low amplitude (0.14 degree). It had a maximum torsional amplitude of 5.4 degrees at a wind speed of 5.40 m/s. ‘H’ section had higher torsional amplitude than the rectangular section during the torsional-DOF tests. But during the vertical-torsional tests, the rectangular section had higher torsional amplitude (7 degrees) than the ‘H’ section due to the coupled motion.

Both the hybrid section and rectangular section (B/D=1) started to flutter in the vertical DOF around 2.04 m/s. Both the hybrid section and rectangular section (B/D=1) exhibited vertical-torsional motion at 3.53 m/s. Figure 4.39 shows the comparison of normalized vertical RMS amplitude between the rectangular (B/D=1) and hybrid sections. The rectangular section (B/D=1) has slightly higher vertical displacements than the hybrid section. Figure 4.40 shows the comparison of torsional RMS amplitude between the rectangular and hybrid sections. The hybrid section has slightly higher torsional amplitude than the rectangular section. In a vertical-torsional

DOF, the flutter speed of the hybrid section is 5.38 m/s, which is almost same as the flutter speed of the rectangular section (B/D=1) which is 5.40 m/s.

Certainly, instead of having a full section model with only rectangular section or only complete 'H' section, if a hybrid section of combined rectangular and 'H' section is used, it is possible to generate higher wind power at lower wind speeds (≥3.53 m/s) from the flow-induced vibrations due to coupled vertical-torsional motion.

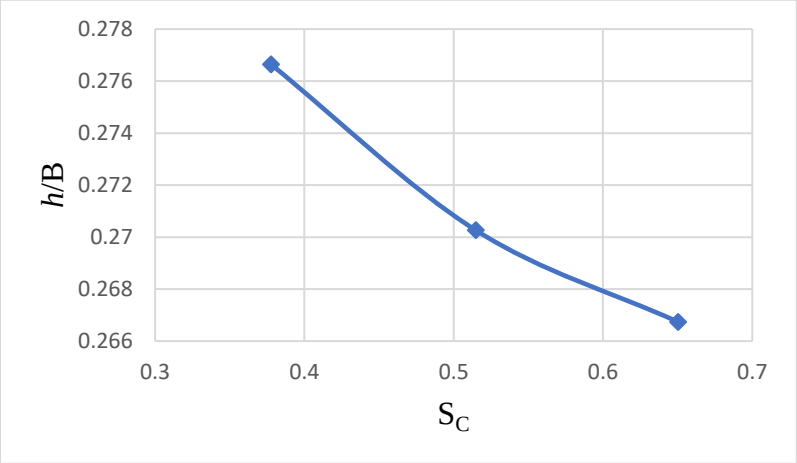

Figure 4.41 Normalized Vertical RMS Amplitude vs Scruton number for Hybrid section

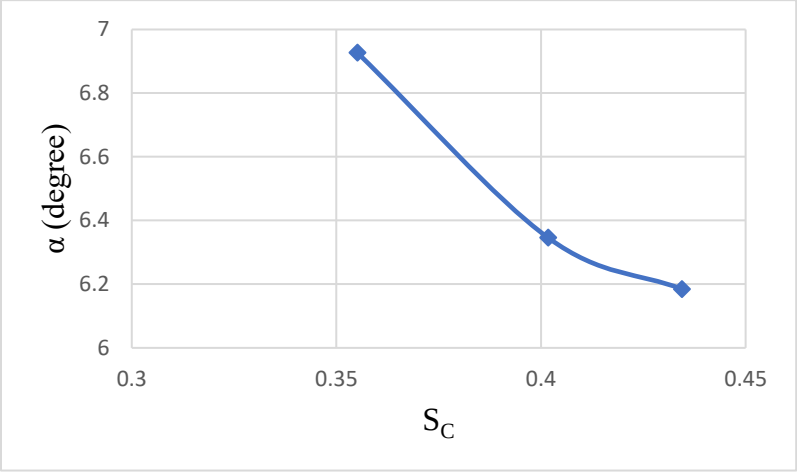

Figure 4.42 Torsional RMS Amplitude vs Scruton number for Hybrid section

Figure 4.41 and 4.42 shows the variation of vertical and torsional amplitude with respect to Scruton number for the hybrid section. Like the rectangular and 'H' sections, the vertical and torsional amplitudes of displacement decrease with increasing Scruton number for the hybrid section.

4.6 Prediction of Energy Capture in Time Domain

The maximum available power over one cycle of oscillation for each section models are tabulated below in Table (4.3). The average power available is determined at a wind speed slightly below the flutter speed as the system becomes unstable beyond the flutter speed. The total power available when a section model vibrates in a 2-DOF is greater than the total power available when the same model vibrates in a 1-DOF, which is exhibited by both the rectangular sections. The hybrid section has the maximum available power (3.64 W) over one cycle of oscillation in a coupled vertical-torsional motion at a wind speed of 4.1 m/s. This is because the hybrid section has higher torsional amplitude than the rectangular section (B/D=1) in a coupled vertical-torsional motion at wind speeds below the flutter speed.

Also, the power generated is directly proportional to $\omega_h{}^3$, the hybrid section has higher torsional frequency (5 Hz) than the rectangular section (4.8 Hz). In the 2-DOF test for the rectangular section (B/D=1), the maximum available power in the vertical DOF is 2.4 W and the maximum available power in the torsional DOF is 1.1 W which yields a total power of 3.5 W. For the hybrid section, the maximum available power in the vertical DOF is 2.18 W and the maximum available power in the torsional DOF is 1.46 W which yields a total power of 3.6 W. Thus, at wind speeds below the flutter speed, the hybrid section can be used to harvest higher wind energy than the rectangular sections. But at higher wind speeds flutter speed, the

rectangular section (B/D=1) has higher amplitudes of vibration in both DOF (vertical and torsional) than the hybrid section and hence can be used instead.

Table 4.3 Comparison of Maximum available power for different cross-sections

Section Model	DOF	Maximum Available Power (W)	Wind speed at max power (m/s)
Rectangular (B/D=1.5)	Vertical	1.44	4.1
Rectangular (B/D=1.5)	Vertical-Torsional	1.62	4.1
Rectangular (B/D=1)	Vertical	3.16	4.1
Rectangular (B/D=1)	Vertical-Torsional	3.5	4.1
'H' section (Configuration 1)	Torsional	0.67	5.0
'H' section (Configuration 2)	Torsional	0.36	5.0
'π' section	Torsional	0.27	5.0
Hybrid	Vertical-Torsional	3.64	4.1

4.7 Devised FIV Wind Energy Harvester

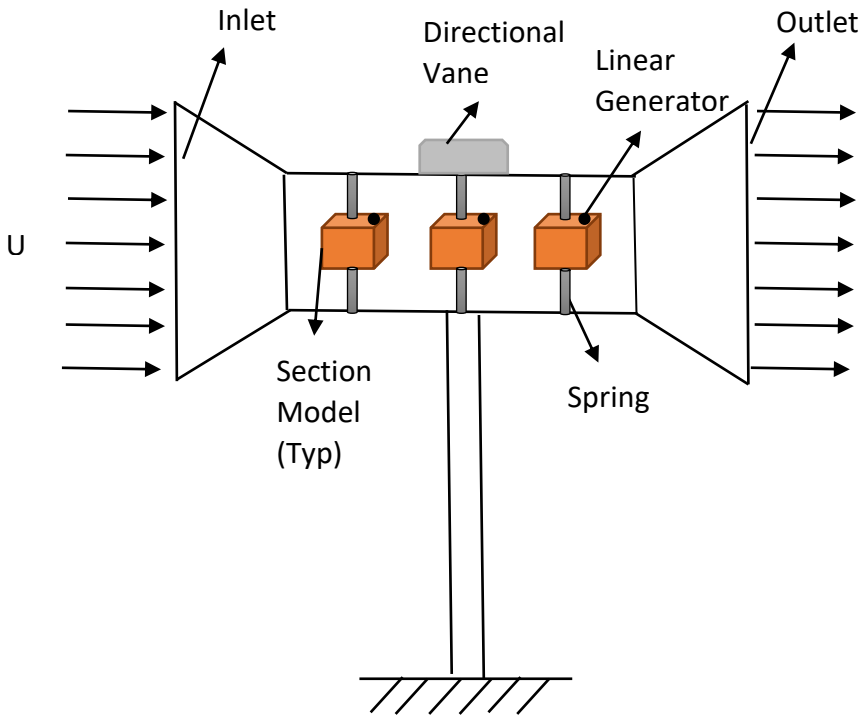

Figure 4.43 FIV Wind Energy Harvester

Figure 4.43 shows a conceptual design of a FIV wind energy harvester that uses a linear actuator-type generator to generate the wind energy from the vibrating section model that the system can potentially capture. For example, a FIV wind energy harvester can consist of three or more units of the rectangular (B/D =1.5) sections housed inside a duct with adequate separation. The width, depth and length of the rectangular sections that are proposed, say, are assumed as 0.6 m, 0.4 m and 2 m. Thus, the total power generated is thrice the power generated by the individual

unit for a three-unit system. These three units of the FIV wind energy harvester, as shown in Figure 4.43, are suspended by springs and placed inside a duct with a larger inlet followed by a contraction section at both ends of the duct to allow the mechanism to work with reversal of wind flow. The contraction causes an increase in the flow velocity. If the area contraction ratio of the duct is taken as 8, the velocity at inlet of 2.5 m/s will be 20 m/s inside the duct. The inlet area of the harvester is 18 m^2 and the outlet area is 2.25 m^2. The length of the FIV harvester is 9 m to accommodate the three units with adequate spacing. The damping of the linear generator can be determined using equation (2.62). Using equation (2.62), the maximum damping that the linear generator can have for the system to still flutter is determined to be 8.2% using the $H_1^* = 10$ at critical RV = 13.4 for a rectangular section (B/D=1.5) with B = 0.60 m, D = 0.40 m, L = 2m, M = 26.7 kg, f_h = 2.5 Hz, $\xi_{mech} = 0.0012$, Sc = 0.036. A damping of 4% is selected for the linear generator. The mechanical damping of the system is 0.12%, thus the total mechanical damping of the FIV energy harvester is 4.12%. Therefore, Sc = 1.24 for the rigid model with the linear generator. Extrapolating from the results for RMS of displacement h versus Sc relationship, the A/B can be estimated as 0.185, which yields an Average Power yield of 102 Watts. For a 3-unit system as described earlier, the total power will be 306 watts at 20.15 m/s without contraction and 2.52 m/s with an 8:1 area contraction as proposed earlier. The power density which is power generated per unit area of inflow captured is calculated as 17 watts/m^2 over 18 m^2 of inlet (D_{eq} = 4.8 m). Using a linear generator designed with 4% damping, almost 50% of the maximum available wind energy can be captured. A linear generator designed with 5% damping, can capture 62% of the maximum available wind energy.

For comparison, the power density of a conventional wind turbine of rotor diameter 4.8 m, say for example, rotating at 54 rpm at a wind speed of 2.52m/s with a TSR of ~5.4 (C_P=0.35)

comes out as 3.4 watts/m^2. The system parameters like the mass, mass moment of inertia of the harvester, width, depth and length of the section units, frequency of vibration, sectional shape, 1 or 2 DOF system, pivot point, frequency and mass ratios can be selected to optimize the FIV wind energy harvester even further by reducing the flutter speed and increasing the power output.

4.8 Extracted Rational Function Coefficients from Flutter Derivatives

Rational function coefficients were extracted using the flutter derivative data for the rectangular sections and 'H' section using the formulation and methodology presented in Chapter 2. The rational function coefficients for the 'H' section are presented here. The eight flutter derivatives associated with the coupled vertical-torsional motion $\underline{H_1^*}$, $\underline{H_2^*}$, $\underline{H_3^*}$, $\underline{H_4^*}$, $\underline{A_1^*}$, $\underline{A_2^*}$, $\underline{A_3^*}$, $\underline{A_4^*}$ and the reduced velocity are the inputs for the formulation. The entire range of reduced velocity available from the data is divided into multiple sections. Dividing into separate sections will give more refined rational function coefficients for each section with which the aeroelastic forces and displacements can be numerically simulated more accurately for a given wind speed. Each section or regime of normalized wind speeds will have their own rational function coefficients which is a new proposition. The rational function coefficients of the first section are not applicable for the second section or vice-versa. For the 'H' section, all the eight flutter derivatives are available for a reduced velocity of up to 9.5. Thus, the entire range of reduced velocity is divided into two sections. Reduced velocity below 5 will be the first section and reduced velocity of 5 – 9.5 will be the second section.

Section 1: Reduced Velocity Below 5

$$A_0 = \begin{bmatrix} -12.9139 & -2.3689 \\ 2.1882 & -1.3884 \end{bmatrix} \quad A_1 = \begin{bmatrix} -6.6545 & 0.1202 \\ -1.3537 & -0.2539 \end{bmatrix} \quad F = \begin{bmatrix} 5.2060 & -4.3026 \\ -12.4377 & 4.3995 \end{bmatrix}$$

$$\lambda_{L1} = -0.4105 \quad \lambda_{L2} = -1.1550 \quad \lambda_{M1} = -2.9648 \quad \lambda_{M2} = 0.0773$$

Section 2: Reduced Velocity of 5 – 9.5

$$A_0 = \begin{bmatrix} 12.5995 & -20.2722 \\ -21.0052 & -0.3084 \end{bmatrix} \quad A_1 = \begin{bmatrix} -7.3197 & 1.2175 \\ 3.0144 & -1.0977 \end{bmatrix} \quad F = \begin{bmatrix} -10.8672 & 15.9102 \\ 21.2732 & 2.5827 \end{bmatrix}$$

$$\lambda_{L1} = 0.0098 \quad \lambda_{L2} = 0.2189 \quad \lambda_{M1} = -0.044 \quad \lambda_{M2} = 0.5662$$

To verify the correctness of the extracted rational function coefficients, all the eight flutter derivatives were calculated using the extracted rational function coefficients using the relationship between the two and compared with the original flutter derivates.

Figures 4.44 to 4.51 show the comparison of flutter derivatives generated using the extracted rational function coefficients and the original flutter derivatives. The extracted flutter derivatives match well with the original flutter derivatives, validating the correctness of the extracted rational function coefficients. Here the rational function coefficients were extracted using n sets of flutter derivatives and reduced velocity where n is the number of data points. Thus, the flutter derivatives generated using the extracted rational function coefficients depend on the number of data points. By increasing the number of data points, the accuracy of the rational function coefficients can be certainly enhanced.

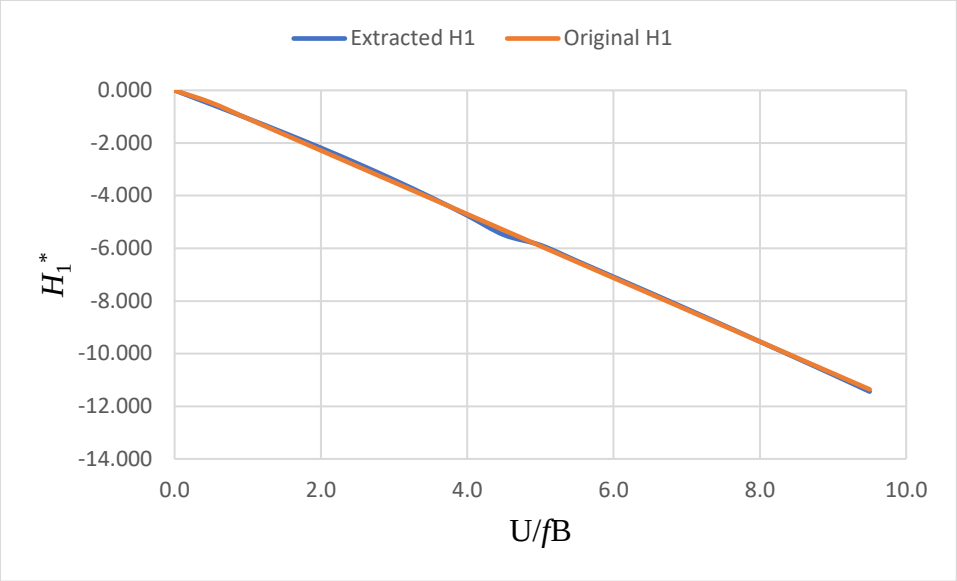

Figure 4.44 Comparison of Extracted and Original H_1^*

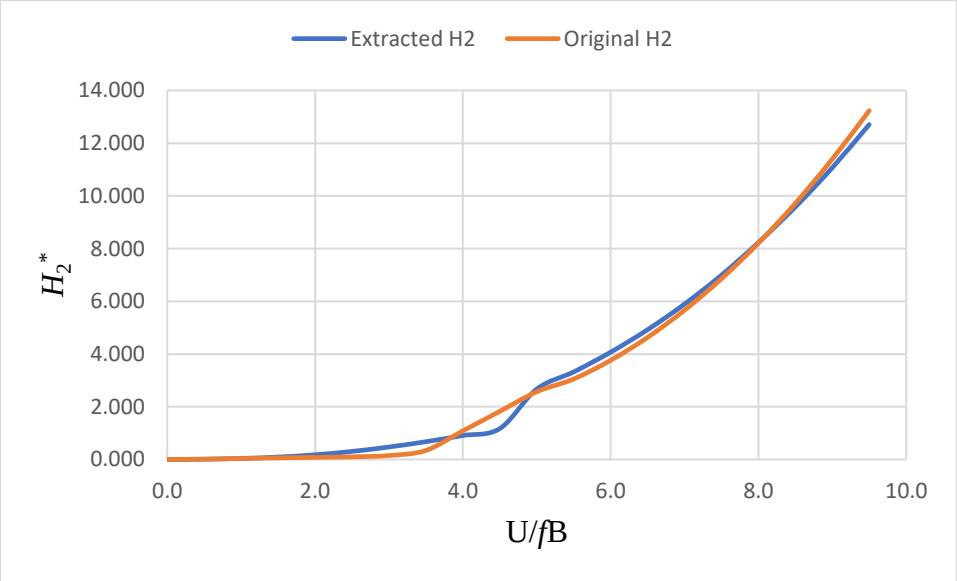

Figure 4.45 Comparison of Extracted and Original H_2^*

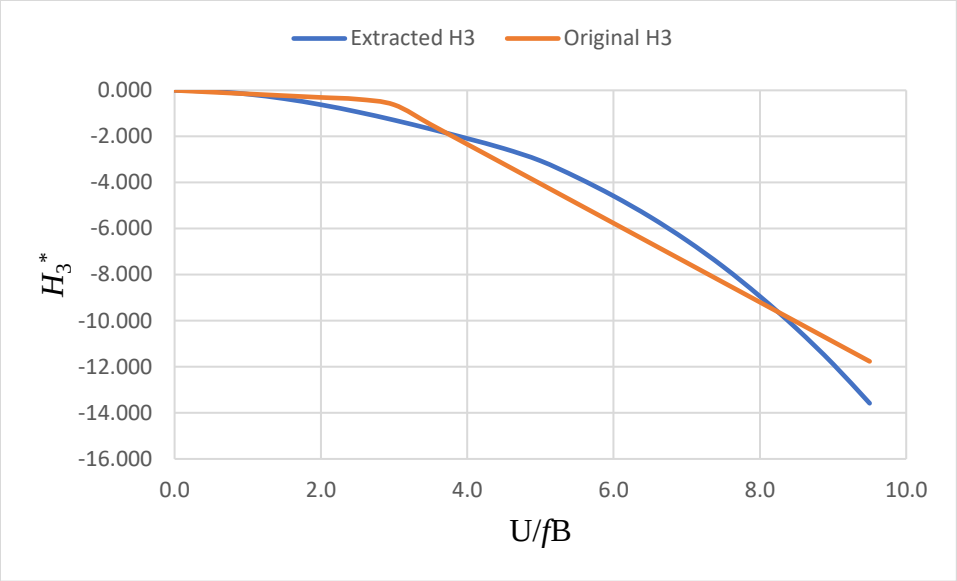

Figure 4.46 Comparison of Extracted and Original H_3^*

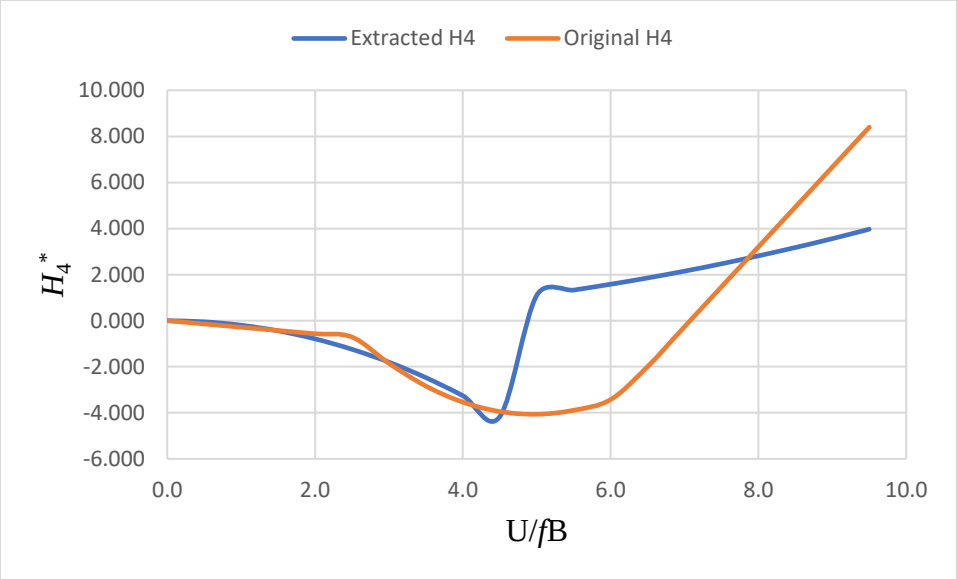

Figure 4.47 Comparison of Extracted and Original H_4^*

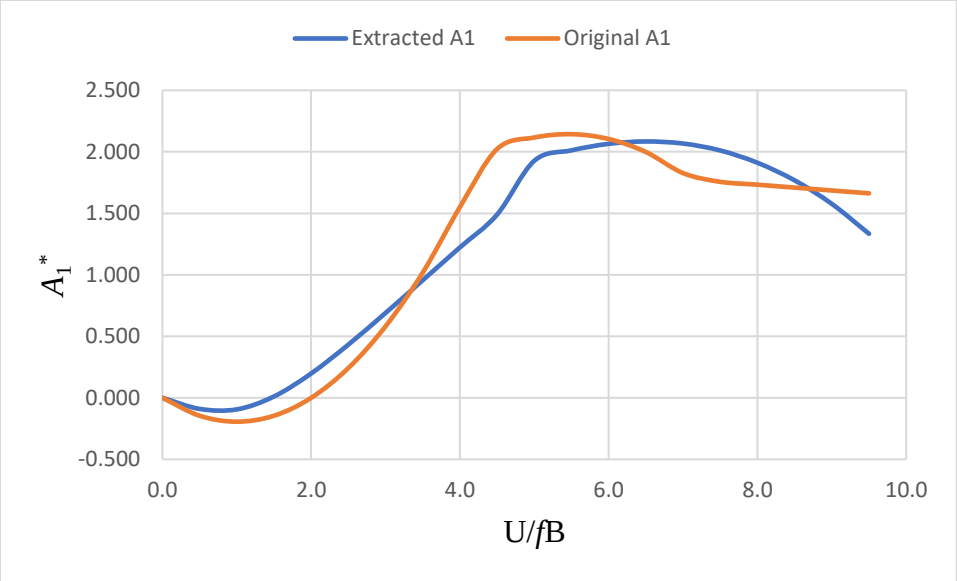

Figure 4.48 Comparison of Extracted and Original A_1^*

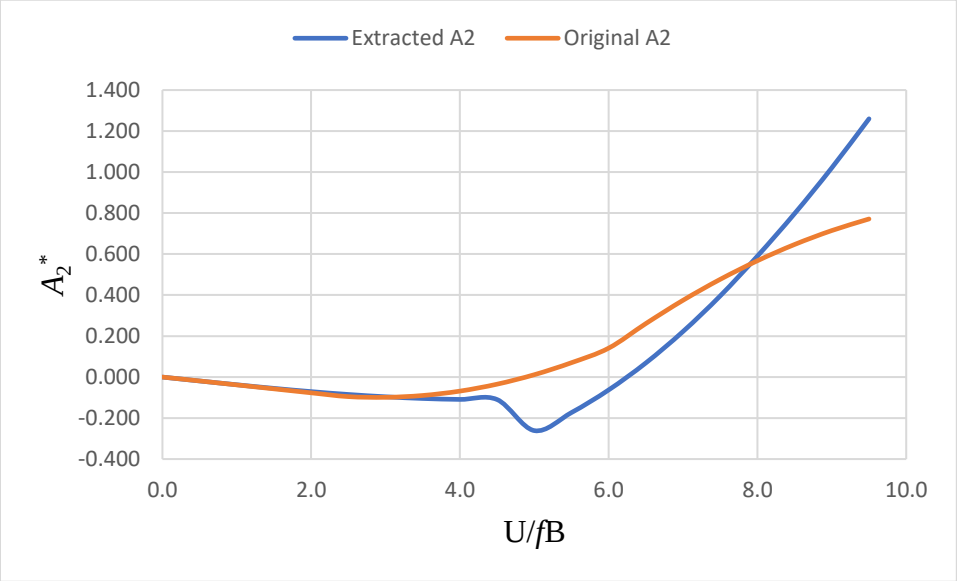

Figure 4.49 Comparison of Extracted and Original A_2^*

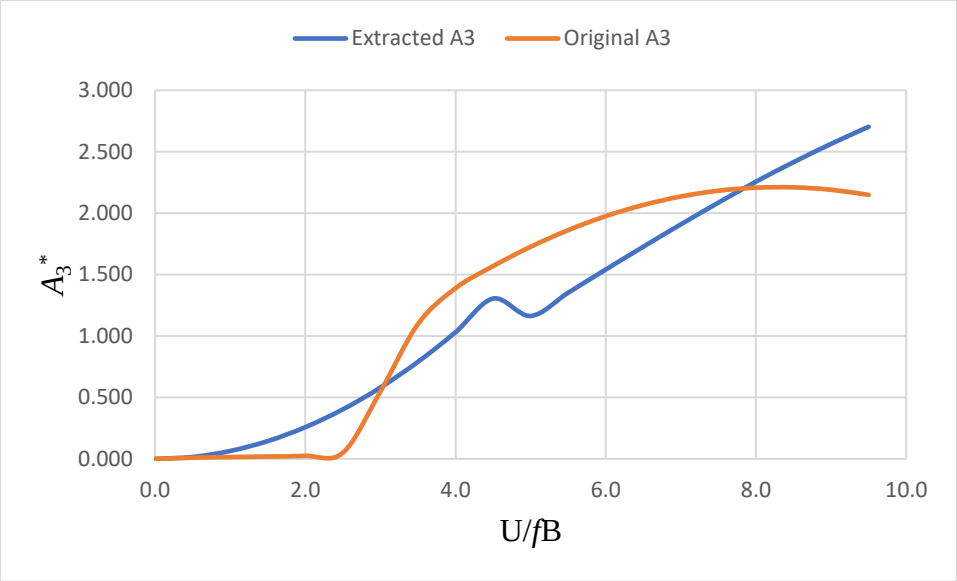

Figure 4.50 Comparison of Extracted and Original A_3^*

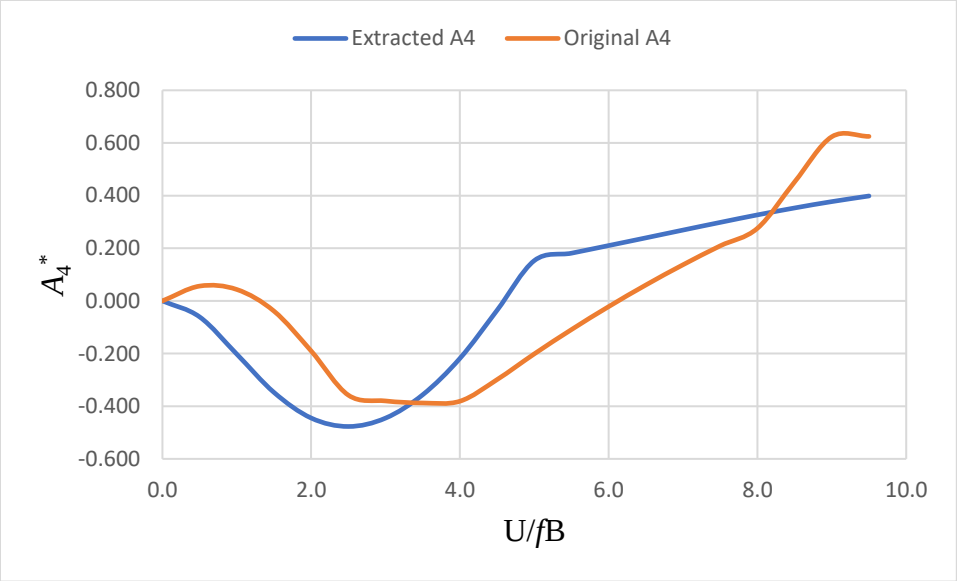

Figure 4.51 Comparison of Extracted and Original A_4^*

The extracted rational function coefficients were used to numerically simulate the torsional displacement (α) of the 'H' section for a time period of one second. Figure 4.52 shows

the comparison of experimentally obtained and numerically simulated torsional displacement for the ‘H’ section at a wind speed of 4.08 m/s below the flutter speed. There is a good agreement between the experimentally obtained and numerically simulated torsional displacements, validating the correctness of the extracted rational function coefficients.

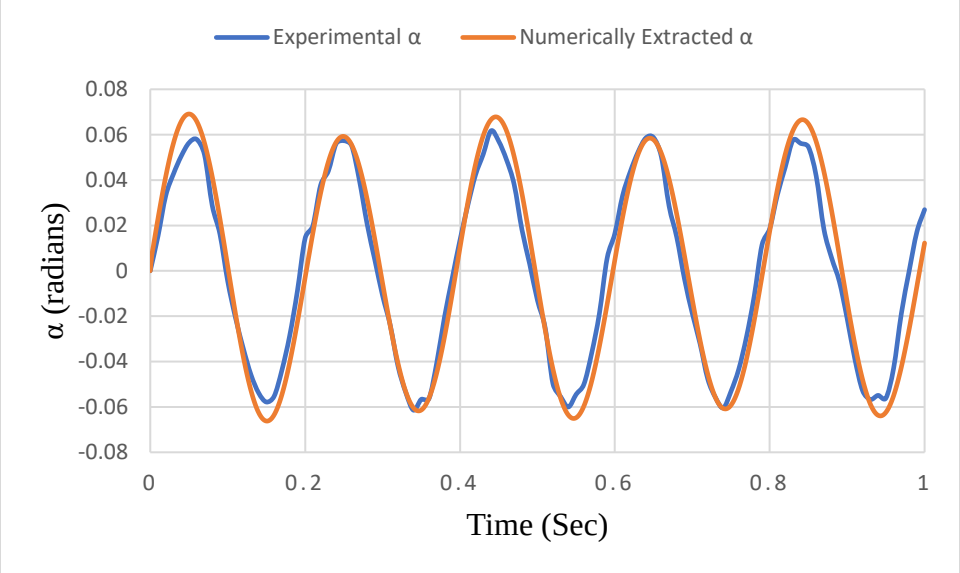

Figure 4.52 Comparison of Experimental and Numerically Simulated α

CHAPTER 5. SUMMARY AND CONCLUSION

5.1 Summary and Conclusions

The main objective of this study was to explore the feasibility of a flutter-driven wind energy harvester referred here as FIV (or flutter-induced vibration) wind energy harvester using rigid-body motions of section models with specific cross-sections that can harvest wind energy at low wind speeds. The objective of this study was to explore the parameters that will influence the performance of the FIV wind energy harvester which is assessed by the low magnitude of flutter speed and large magnitude of vibration amplitude at or near flutter.

Section models are rigid-models with 1 to 3 degree-of-freedom (DOF) that faithfully represent the geometry of the cross-section of a structure over a finite length, with end plates to simulate a 2D-flow. There are various cross-sections of section models that are prone to vibration at a given wind speed along a particular DOF. Rectangular sections of aspect ratio (AR) less than 2 usually have low flutter speeds in the vertical DOF and 'H'-shaped sections, used in old long-span bridges like the first Tacoma Narrows Bridge, have low flutter speeds in the torsional DOF. A hybrid section model formed by combining these two sections is therefore expected to be more sensitive to a coupled vertical-torsional flutter at low wind speeds. Such hybrid cross-sections are ideal for a 2-DOF (vertical and torsional) FIV wind energy harvester. Wind tunnel experiments were performed with geometrically scaled models to determine the flutter speed and average wind energy capture for various section models in 1-DOF and 2-DOF motions. For a comparative study, rectangular section models (Aspect Ratio = B/D = AR=1.5 and AR=1) in 1-DOF (vertical or torsional) and 2-DOF (vertical and torsional), and H-shaped section models in torsional DOF were tested.

In the vertical DOF, the rectangular section (B/D=1) was observed to have higher vertical displacement and low flutter speed than that of the rectangular section (B/D=1.5). Higher the response amplitude of a model at a given wind speed, higher will be the power generated. Thus, rectangular section (B/D=1) was considered better than the rectangular section (B/D=1.5) for wind energy harvesting and selected as one of the cross-sections for the hybrid section. In the torsional DOF, the 'H' section (Configuration 1) was found to have higher amplitude of torsional displacement and low flutter speed than the 'H' section (Configuration 2) and the 'π' section. Therefore 'H' section (Configuration 1) was selected as the best cross-section in the torsional DOF for efficient wind energy harvesting. The best rectangular section (AR=1) in the vertical DOF and best H-shaped section (Configuration 1) in the torsional DOF with respect to low flutter speed and high vertical or torsional amplitudes of vibration are combined to form a hybrid section and tested in 2-DOF (vertical and torsional) and compared with the best rectangular section and best H-shaped section for flutter speed and average wind energy available at flutter.

In a vertical-torsional motion, the hybrid section has slightly higher or equal torsional RMS displacement than the rectangular section (B/D=1) at wind speeds below the flutter speed. However, the rectangular section (B/D=1) has slightly higher vertical RMS displacement than the hybrid section (B/D=1) at wind speeds below the flutter speed. The flutter speed of the hybrid section in vertical-torsional motion is 5.38 m/s, which is almost same as the flutter speed of the rectangular section (B/D=1) which is 5.40 m/s. Thus, a section model with only a rectangular section (AR=1) or the hybrid section of combined rectangular and 'H' section can be used for wind power generation from the flow-induced vibrations due to coupled vertical-torsional motion.

Wind energy harvesting at lower wind speeds is the prime interest of this research as these energy harvesters are designed for small-scale wind energy harvesting. Mean daily wind speeds at 10m elevation are generally low (<10 m/s). Even at the lowest available wind speed these FIV wind energy harvesters should be able to scavenge considerable wind energy. From the experiments, we can conclude that the rectangular section (B/D=1) is the best performing section in the vertical DOF with low flutter speed and high amplitude of vertical displacement, 'H' section (Configuration 1 or Symmetric) is the best performing section in the torsional DOF with low flutter speed and high torsional displacement, while the hybrid section or the rectangular section (B/D=1) will be more suitable for wind energy harvesting in a 2-DOF (vertical-torsional), with lower flutter speed and high amplitudes along both DOF. To improve the performance of the FIV wind energy harvester, a parametric study of the flutter mechanism was conducted to understand the effects of frequency ratio (2-DOF), mass ratio, offset distance (distance between centers of mass and stiffness) and choice of DOF on flutter speed and response amplitude. Both rectangular and hybrid section exhibited combined vertical-torsional motion only at a frequency ratio (ratio of vertical frequency to torsional frequency) of $\sigma = 0.5$. From the experiments performed, a frequency ratio of 0.5 is more applicable for a 2-DOF wind energy harvester than a frequency ratio of 0.25. It was observed that as the mass ratio increases, the flutter speed increases and response amplitude decreases. Thus, the mass of the system should be as low as possible for enhanced power generation at relatively lower wind speeds. The flutter speed of the models increased as the offset distance changed from negative (backward offset) to zero to positive value (forward offset). The backward-offset case (center of stiffness is ahead of the center of mass from the leading edge) has the lowest flutter speed and highest amplitude of displacement than the zero-offset and forward-offset case (center of stiffness is aft

of the center of mass from the leading edge). Thus, a small backward offset can be given to the system to increase the power generation and lower the flutter speed.

The maximum power available when a section model is vibrating in 1-DOF or 2-DOF is tabulated and compared in Chapter 4, section 4.6 for all the cross sections. The hybrid section was found to have the highest available power of 3.6 W and the rectangular section (B/D=1) came in second with available power of 3.5 W over one cycle of vibration while vibrating in a 2-DOF (vertical-torsional) motion at wind speeds below the flutter speed.

Next, a FIV wind energy harvester was designed using 3 units of rectangular section (B/D=1.5) in 1 DOF (vertical), as an example, to estimate the amount of wind energy that can be captured when the sections vibrate at or above the flutter speed. The section model for the harvester was scaled up from the model tested for higher power generation. The width and depth of the rectangular section was selected as 0.6 m and 0.4 m (4 times the model tested), respectively, and length was increased to 2 m from 1.5 m of the model tested. The total mass of the section was estimated as 26.7 kg and frequency was kept to be the same 2.5Hz. A linear-actuator type generator is proposed to capture the energy from the vibration. The damping of the linear generator used is critical in determining the amount of power that can be captured. A linear generator can be designed to have a specific mechanical damping. It is important to determine the maximum damping ratio of the linear actuator that can be sustained in the system at flutter (using equation 2.62), based on which the damping of the linear generator can be determined. A linear generator with 4% damping can be shown to capture 50% of the total power and a linear generator with 5% damping can be shown to capture 62% of the total available power. Ideally, one cannot capture 100% of the available power considering the losses in the system due to friction, mechanical losses, etc. The maximum power that is available with one unit of the

rectangular section was estimated around 206 W at a wind speed of 20 m/s. Using the linear generator, a power of 102 W can be captured at this wind speed. The FIV wind energy harvester uses a duct with a contraction section with an area contraction ratio of 8:1 and an inlet area of 18 m^2 and outlet area of 2.25 m^2, causing an increase in the flow velocity at the inlet of 2.5 m/s to 20 m/s inside the duct where the units of power generation will be located. The length of the FIV wind energy harvester is 9 m to accommodate the three units with adequate spacing. Thus, for a three-unit harvester, it could generate 306 W at or above 2.5 m/s capturing wind over an area of 18 m^2 (D_{eq}=4.8m), which yields a power density of 17 W/m^2. The average power density of a conventional rotor-type wind turbine of rotor diameter 4.8 m, say for example, rotating at 54 rpm at a wind speed of 2.52m/s with a Tip-Speed-Ratio (TSR) of ~5.4 (C_P=0.35) comes out as 3.4 watts/m^2. Thus, the FIV wind energy harvester has almost 5 times the power density of a conventional wind turbine at the same wind speed. The FIV energy harvester presented in this study is therefore suitable for small-scale wind energy harvesting with considerably high-power density.

A new method was developed to extract the rational function coefficients, used in time-domain flutter analysis, directly from the flutter derivatives that are used in frequency domain analysis to help in the parametric study of this fluid-structure problem in the future. The algorithm presented in this study for extracting rational function coefficients were validated using the wind tunnel experimental results. The extracted rational function coefficients were used to numerically predict the torsional displacement of a ‘H’ section (Configuration 1) whose flutter derivatives were taken from the literature. The numerically simulated torsional displacement matched well with the torsional displacement obtained from the wind tunnel experiments. The extracted rational functions coefficients were used to calculate all the eight

flutter derivatives using the relationship between them and compared with these original flutter derivatives for the ‘H’ section. The flutter derivatives extracted from the rational function coefficients matched well with the original flutter derivatives of the ‘H’ section, thereby validating the correctness of the algorithm.

5.2 Recommendations

The recommendations apply to the suspension system developed in this study, so that the improved system can be used in the future research. The horizontal ‘C’ channel section used to suspend the model has series of holes which is at an interval of one inch, to attach the springs on top and bottom sides. The springs need to be moved in and out to change the frequency ratio. Due to the pre-drilled holes, the frequency ratios are pre-defined, and it cannot be modified. Instead of drilled holes if a continuously slotted hole is made along the length of the ‘C’ channel section mid-plane, then the springs can be moved wherever they need to be and fixed with the help of a set screw, to target a desired frequency ratio. Also, while changing the frequency ratio, it was cumbersome and time consuming to remove the springs from one hole and fixing it in another hole. This process can be made easier with a continuously slotted hole.

At higher wind speeds, when the section models had higher amplitude of displacements, the leaf springs that were used to restrict the lateral motion deformed, which imposed a slight hinderance to the vibrating model. The leaf springs had to be replaced thrice throughout the experiments to address this problem. A better leaf spring or another mechanism to restrain lateral motion can be used to resolve this issue.

The section models were built using plexiglass to have lowest possible weight and it was cost efficient too. The end plates which were designed to support the model at the center and at the end were also built using plexiglass. As the experiments progressed, the smaller end plates

which were used to support the model at the center started to develop cracks. This was because we had to unscrew and screw them whenever we switch between the models. Also, many screws were used to prevent any bending moment to be developed at the center of the model. Over a period of time the cracks developed and eventually one of the smaller end plates collapsed. A new pair of end plates were built to replace them. Instead, the end plates can be built using wood as they are light weighted and cost efficient too. Unlike the plexiglass they would not develop cracks while screwing and unscrewing to the model.

5.3 Future Research

A 2-DOF FIV wind energy harvester (vertical-torsional) is presented in this study for wind energy harvesting. Instead of a coupled vertical-torsional motion, vertical-lateral and torsional-lateral experiments can be performed by designing a hybrid section using best performing cross-section in the lateral direction. By this way, the best 2-DOF FIV wind energy harvester can be determined.

The rectangular sections exhibited higher amplitudes of displacement during 2-DOF test than 1-DOF test, especially in the torsional DOF. It also started to flutter in the torsional DOF at a much lower wind speed during the coupled vertical-torsional motion test. Also, the total available power in a 2-DOF motion is greater than the power available in a 1-DOF motion. Therefore, a 3-DOF FIV wind energy harvester can be developed using best performing vertical, torsional and lateral hybrid cross-sections. A 3-DOF suspension system has already been devised and used for past wind tunnel experiments in the WiST lab at Iowa State University. A 3-DOF wind energy harvester can be designed, and the performance of such harvester can be examined by conducting similar experiments using this suspension system.

If a backward offset is given to the model, then the model has increased amplitude of vibration and lower flutter speed. To understand the variation of the amplitude of vibration and flutter speed within the backward offset region, experiments can be performed for multiple backward offset points. This will help to find the best offset distance that can be used to enhance the power generation.

REFERENCES

[1] Arnold, D. (2007). Review of microscale magnetic power generation. IEEE Transactions on Magnetics, 43, 3940–3951.

[2] Mitcheson, P., Miao, P., Start, B., Yeatman, E., Holmes, A., & Green, T. (2004). MEMS electrostatic micro-power generator for low frequency operation. Sensors Actuators A, 115, 523–529.

[3] Abdelkefi, A., Nayfeh, A. H., & Hajj, M. R. (2012d). Design of piezoaeroelastic energy harvesters. Nonlinear Dynamics, 68, 519–530.

[4] L. Pigolotti, C. Mannini, G. Bartoli. Experimental investigations on a flat plate equipped with porous screens undergoing classical flutter oscillations, Proc. XIV Conference of the Italian Association for Wind Engineering (IN-VENTO-2016), Terni, Italy, 2016.

[5] J. Young, J.C.S. Lai, M.F. Platzer. A review of progress and challenges in flapping foil power generation, Prog. Aerosp. Sci. 67 (2014) 2-28.

[6] L. Caracoglia. Feasibility assessment of a leading-edge-flutter wind power generator, J. Wind Eng. Indust. Aerodyn. 98(10-11) (2010) 679– 686.

[7] Bochao Cao, Partha P. Sarkar. Identification of Rational Functions using two-degree-of-freedom model by forced vibration method, Engineering Structures 43 (2012) 21–30.

[8] Masaru Matsumoto. Aerodynamic damping of prisms, Journal of Wind Engineering and Industrial Aerodynamics 59 (1996) 159-175.

[9] Fangwei Hou, Partha P. Sarkar. Time-domain model for prediction of generalized 3DOF buffeting response of tall buildings using 2D aerodynamic sectional properties, Engineering Structures 232 (2021) 111847.

[10] Scanlan RH, Tomko JJ. Airfoil and Bridge deck flutter derivatives. J Eng Mech Div 1971;97(6):1717-33

[11] Heather Scot Sauder, Partha P. Sarkar. Real-time prediction of aeroelastic loads of wind turbine blades in gusty and turbulent wind using an improved load model, Engineering Structures 147 (2017) 103-113.

[12] Junlei Wang. The state-of-the-art review on energy harvesting from flow-induced vibrations, Applied Energy 267 (2020) 114902

[13] Antonino Maria Marra. Measurements and improved model of vortex-induced vibration for an elongated rectangular cylinder Antonino, J. Wind Eng. Ind. Aerodyn. 147 (2015) 358–367.

[14] Gang Hu. Experimental investigation on the efficiency of circular cylinder-based wind energy harvester with different rod-shaped attachments, Applied Energy 226 (2018) 682–689.

[15] Guangcheng Zhang. Energy harvesting utilizing reciprocating flow-induced torsional vibration on a T-shaped cantilever beam, SMS-106931.R1

[16] Junlei Wang. Efficiency investigation on energy harvesting from airflows in HVAC system based on galloping of isosceles triangle sectioned bluff bodies, Energy 172 (2019) 1066-1078.

[17] Xiaobiao Shan. A curved panel energy harvester for aeroelastic vibration, Applied Energy 249 (2019) 58–66.

[18] Wan Sun. Development of a novel vibro-wind galloping energy harvester with high power density incorporated with a nested bluff-body structure, Energy Conversion and Management 197 (2019) 111880.

[19] Jiantao Zhang. Modeling and nonlinear analysis of stepped beam energy harvesting from galloping vibrations, Journal of Sound and Vibration 479 (2020) 115354.

[20] L.B. Zhang. Theoretical modeling, wind tunnel measurements, and realistic environment testing of galloping-based electromagnetic energy harvesters, Applied Energy 254 (2019) 113737.

[21] Bochao Cao, Partha P. Sarkar. Identification of rational functions by forced vibration method for time-domain analysis of flexible structures. In: Proceedings: the fifth international symposium on computational wind engineering, Chapel Hill; 2010.

[22] Arindham Gan Chowdhury, Partha P. Sarkar. Experimental identification of rational function coefficients for time-domain flutter analysis, Engineering Structures 27 (2005) 1349–1364.

[23] Partha P. Sarkar. Identification of aeroelastic parameters of flexible bridges, J.Eng.Mech. 1994.120:1718-1742.